TWO-DEGREE-OF-FREEDOM SUBSONIC WING ROCK

AND

NONLINEAR AERODYNAMIC INTERFERENCE

by

Jamal M. Elzebda

Dissertation submitted to the Faculty of the

Virginia Polytechnic Institute and State University

in partial fulfillment of the requirements for the degree of

DOCTOR OF PHILOSOPHY

in

Engineering Mechanics

APPROVED:

Dean T. Mook, Chairman

Ali H. Nayfeh, Chairman

Saad A. Ragab

Scott L. Hendricks

Daniel Frederick

Michael Williams

December, 1986

Blacksburg, Virginia

ACKNOWLEDGMENTS

The author expresses his gratitude and appreciation to both chairmen of his committee:

Dr. Dean Mook for his continuous guidance, encouragement, and understanding throughout this work.

Dr. Ali Nayfeh for his significant remarks and contributive suggestions.

Special thanks to Dr. S. Ragab, Dr. S. Hendricks, Dr. D. Frederick and Dr. M. Williams for giving their valuable time in reading this manuscript.

I would like also to express my sincere appreciation to

for their great friendship and continuous encouragement.

Finally, my very deep gratitudes are expressed to my wife,

, to my brother, , and to my parents,

. Their patience, love, and moral support made this contribution possible.

This work was supported by the Office of Naval Research and the Air Force Office of Scientific Research.

TABLE OF CONTENTS

Page

Page

LIST OF FIGURES

Figure Page

LIST OF TABLES

CHAPTER I

INTRODUCTION

1.1 Statement of the Problem

In this thesis, two modern aerodynamic problems that are of equal importance are carefully investigated.

1.1.1 Wing-Rock Phenomenon

Combat aircraft such as the F-4 (Phantom) and A-4 (Skyhawk) (Schmidt, 1979), the Northrop F-5 (Hwang and Pi, 1978), the Grumman F-14 (Tomcat) (Nguyen et al, 1980), the HP-115 (Ross, 1972), and the F-15 and the X-29A (Hsu, 1985) often operate at subsonic speeds and high angles of attack in parts of their flight envelopes. Several maneuvers such as take-off and landing are examples where such fighters undergo high angles of attack while traveling at subsonic Mach numbers. At such high angles of attack, these aircraft enter into an oscillatory, mainly rolling motion, known as wing rock. This phenomenon can be a major maneuver limitation and can pose a serious safety problem (AGARD, 1979). Here the problem of one- and two-degrees-of-freedom of subsonic wing rock is simulated numerically.

1.1.2 Unsteady Aerodynamic Interference

Many modern configurations, especially those employing canards, place new demands on the ability of aerodynamicists to predict interference. The main difficulty comes from the fact that the

vorticity being continuously convected from the trailing edges, wing tips, and possibly the leading edges of the canards typically passes close to the main wing. Consequently, the strength and location of the vorticity in these wakes must be determined accurately if the loads on the main wing are to be predicted accurately. The problem becomes even more complicated if the flow is highly unsteady (Elzebda et al, 1985). Here the problem of unsteady aerodynamic interference for lifting surfaces is treated numerically.

1.2 Current State of Knowledge

Before exploring the literature covering the above two topics, we shall review the history of the unsteady vortex-lattice method (UVLM), which is the basic tool of the numerical techniques used in this thesis.

1.2.1 Unsteady Vortex-Lattice Method (UVLM)

Belotserkovskii (1966) was the first to contribute in the area of the vortex-lattice method for steady and unsteady flows over any planform and deformed wing. The method did not predict the shape of the wake as part of the solution; therefore, it was limited to small angle of attack. Three years later, Belotserkovskii (1969) developed the first successful nonlinear numerical technique for steady flows over arbitrary planforms, which calculated aerodynamic loads on wings with tip separation.

Belotserkovskii and Nisht (1974) extended the above method to predict the unsteady flow over swept-back and rectangular wings. They

determined the shape of the wakes emanating from the wing tips and trailing edge, but they did not account for leading-edge separation when they considered delta wings. Later, many investigators added significant contributions to the development of this method.

The general unsteady vortex-lattice method used in this thesis is, by far, the most complete method for reasons to be mentioned as the discussion of literature unfolds. The method is similar to the one presented by Belotserkovskii. Maddox (1973) and Mook and Maddox (1974) were the first to add the concept of leading-edge separation to the vortex-lattice method. They added a system of discrete, nonintersecting vortex lines to simulate the wake at the leading edge of a delta wing. Each of these vortex lines consisted of a series of short straight segments except the last one, which was a semi-infinite segment. Then they iterated to adjust the leading-edge wake to the force-free position. However, this method did not account for force-free wing-tip and trailing-edge vortex sheets. Kandil (1974) and Kandil, Mook and Nayfeh (1974) improved this method and applied it to different planforms and got very good agreements with existing experimental data. Such progress motivated Atta (1976) and Atta, Kandil, Mook and Nayfeh (1976; 1977) to extend the method in order to treat unsteady flows over wings of arbitrary planforms with sharp-edge separation.

All applications introduced, so far, posed the problem in terms of a ground-fixed inertial frame, but this formulation proved to be inconvenient. Therefore, Thrasher, Mook, Kandil and Nayfeh (1977) and Kandil, Atta and Nayfeh (1977) posed the problem in terms of a body-

fixed frame and enhanced the method to treat flows past wings executing arbitrary maneuvers. This led to a completely general method as long as separation takes place along the sharp edges of the wing, and vortex bursting does not occur above the surface of the wing.

Thrasher (1979) combined the method at hand with a fourth-order predictor-corrector method to simultaneously predict the flowfield and motion of a rectangular wing with a hinged flap. Thrasher, Mook and Nayfeh (1979) applied the steady version of this method to simulate the flow over sails. Levin and Katz (1981) applied the unsteady vortex-lattice method to solve flow over delta wings with leading-edge separation. They compared this method to a steady-state iterative method with the same panel configuration. Both methods gave the same results. However, the unsteady method required less computer time.

Finally, Nayfeh, Mook and Yen (1979) and Konstadinopoulos (1981) and Konstadinopoulos, Mook and Nayfeh (1981) and Konstadinopoulos, Thrasher, Mook, Nayfeh and Watson (1985) developed the most general and complete form of the unsteady vortex-lattice method. This method will be discussed in detail in Chapter II.

1.2.2 Wing Rock

Many efforts have been made to investigate and understand this phenomenon. Different researchers gave different arguments as to what are the physical mechanisms that may cause wing rock.

Ross (1972) examined the Handley-Page 115 research aircraft which has highly swept wings (with leading-edge sweep $\Lambda = 75^{o}$). He discovered

that wing rock started at $\alpha = 19^0$ in the flight tests and at $\alpha = 14^0$ in his wind-tunnel experiment (where α is the angle of attack). Ross indicated that limit cycles occur when either the rolling or yawing moment is cubic with respect to the sideslip angle. Hwang and Pi (1978) modeled the Northrop F-5A to simulate the wing rock oscillations at transonic speeds. They suggested that wing rock was generated by a limit-cycle mechanism due to the fluctuating pressure changes on the wing top surfaces, particularly close to the wing-tip region. Using the F-94A in his analysis, Schmidt (1979) applied control-theory concepts to identify an aerodynamic hysteresis as the cause of limit-cycle motions. This aerodynamic hysteresis corresponds to a roll moment relay action that is dependent upon the sign of sideslip velocity. In addition to his study (Ross, 1972) in which he concluded that nonlinearities in moments due to sideslip can cause limit cycles, Ross (1979) claimed that a rolling moment nonlinear in roll rate can also cause limit-cycle motion when he examined the Gnat aircraft.

In an attempt to understand the basic mechanisms that cause wing rock, Nguyen, Yip and Chambers (1981) conducted a number of wind-tunnel experiments using a flat-plate delta wing with 80 degrees leading-edge sweep. In the free-to-roll tests, their model exhibited large-amplitude, limit-cycle wing rock at angles of attack greater than 25 degrees. From the analysis, they indicated that the dependence of aerodynamic roll damping on sideslip is the cause of this phenomenon.

Levin and Katz (1982) conducted wind-tunnel experiments similar to the ones of Nguyen et al but with different support conditions. The

model used by Nguyen et al was free to roll and to exhibit partial coning motions, but the model used by Levin and Katz was only free to roll. Levin and Katz's model exhibited roll oscillation at an angle of attack of 19-20 degrees. Nonlinearities in the rolling moment, vortex asymmetry and vortex breakdown, as reported by Levin and Katz, caused the wing rock. Ericsson (1983) studied the existing experimental results given by Nguyen et al (1981) to describe the flow mechanisms that led to wing rock. Ericsson concluded that wing rock is caused by asymmetric leading-edge vortices and never by vortex breakdown. Vortex breakdown has a damping effect on the rolling motion. He also added that wing rock occurs only for delta wings with more than 74° leading edge sweep for which asymmetric vortex shedding occurs before vortex breakdown.

Using the Standard Dynamics Model (SDM) as his model, Beyers (1983) conducted comprehensive roll-oscillation experiments at a Mach number of 0.6 for angle-of-attack range $25^0 < \alpha < 41^0$ with nonzero sideslip angles. Beyers found that at higher angle of attack ($\alpha > 30^0$) the direct, cross and cross-coupling moment derivatives are highly nonlinear with angle of attack as well as highly sensitive to both angle of sideslip and frequency of oscillation. Conventional aircraft wings and straight or moderately swept leading edges can also undergo wing rock as described by Ericsson (1984). This wing rock is caused by negative damping in plunge of airfoil section experiencing leading-edge type stall with accompanying big loss of lift.

Konstadinopoulos (1984) and Konstadinopoulos, Mook and Nayfeh (1983;1985) and Mook and Nayfeh (1985) presented a numerical simulation of wing rock. They were able to combine the general unsteady vortex-lattice method with a predictor-corrector integration scheme to predict the motion of the fluid and wing (flat delta wing with $\Lambda = 80^{\circ}$) simultaneously and interactively. Their numerical results showed a limit cycle with amplitude of 34° and period of 1.01 seconds when $\alpha = 27^{\circ}$ which are in good agreement with the experimental results produced by Nguyen et al (1981). Their results also showed good comparison with the experimental results of Levin and Katz (1982). Their simulation predicted that the symmetric configuration of the leading-edge vortex system becomes unstable as the angle of attack increases which causes a loss of roll damping at small angles of roll. Consequently, any small disturbances introduced into the flowfield grow, and wing rock develops.

Hsu and Lan (1985) developed a semi-empirical theory to describe the mechanism of wing rock. Combining a mathematical model for the rolling moment coeffient, which is based on existing experimental data produced by Nguyen (1981), with some kinematic relationships, Hsu and Lan derived a nonlinear second-order differential equation for a steady-state limit-cycle wing rock. Then using an asymptotic method, they solved for the limit-cycle amplitude and wing-rock frequency. In their paper, the authors compared the results of their theory with the results on which the theory was based. Furthermore, they used the rolling moment model, which is based on experimental results for one degree-of-

freedom system, to write a similar expression for the yawing moment coefficient, and then they went on to derive a system of equations for the three-degree-of-freedom system. They concluded that wing rock is caused by flow asymmetries, developed by negative or weakly positive roll damping, and preserved by nonlinear aerodynamic roll damping. Moreover, their unified theory (as claimed) is based on experimental data for a certain configuration.

Katz and Levin (1985) conducted the same experiment they performed in 1982, except this time a small canard was installed in front of the delta wing. This experiment emphasized that subsonic wing rock of slender delta wings is caused by dynamic vortex interaction with the lifting surface. It was noticed that leading-edge vortices from the canard enhanced roll oscillations at test conditions for which the basic delta wing would otherwise have been stable. Consequently, the canard increased the range of angle of attack at which wing rock occurred. Brandon and Nguyen (1986) performed a series of subsonic wind tunnel tests to examine the effects of forebody shapes on static and dynamic lateral/directional stability. They found that the cross-sectional shape of the forebody can strongly affect static stability and wing rock behavior at high angles of attack. Forebody-vortex development, behavior of vortices at sideslip conditions, and their interaction with the wing were not very apparent during flow visualization. However, when they considered different forebodies, a trend was noted whereby nose shapes that provided the highest levels of static lateral/

directional stability also caused the highest amplitude of wing rock and vise versa.

From the above survey and to the best of our knowledge, it appears that there is no analytical, or experimental, or numerical study that was undertaken to consider two-degrees-of-freedom wing rock. One of the main goals of the present investigation is to study the influence of an additional degree of freedom on subsonic wing rock of a slender delta wing.

1.2.3 Aerodynamic Interference

Aerodynamic interference is a problem of long-standing interest and therefore one about which much has been written. In their analysis, Giesing, Kalman and Rodden (1972) used the doublet-lattice method and the method of images to predict steady and oscillatory loadings on general configurations such as multiple wings and bodies. They stated that the results could be inaccurate, especially for unsteady flow, if the cross section is represented by only a few elements. This method gave good results as far as the loads are concerned, however, it failed to describe the strength and orientation of vorticity in the wake. An analytical method was presented by Rowe, Winther and Redman (1974) to predict the unsteady aerodynamic loadings on lifting surfaces that are due to oscillatory motions of trailing edge control surfaces. This method was an extension to the work done by Landahl (1968). Again, this technique did not provide any information about the flow mechanisms.

Kandil, Mook and Nayfeh (1977) developed a nonlinear vortex-lattice method to treat different models of canard-wing configurations in steady, low-subsonic invisid flows. Beside predicting pressure distributions and total-load coefficients, the method provided the first attempt towards describing the flowfield and wakes for such configurations. Consequently, by selecting the shape of the planforms, the relative areas, the relative positions and orientations of the canard and the main wing, the strong vortex interaction can be used to obtain the maximum efficiency of the aerodynamic characteristics and hence to achieve better longitudinal control of the aircraft. Comparisons with experimental results were made and qualitative as well as quantative agreements were found.

Normal-force and pitching-moment coefficients of wing-body combinations, at angles of attack up to 40° in the subsonic Mach-number range, were calculated analytically by Nikolitsch (1978). The analysis was for steady-state cases and compared well with test measurements, however; it did not report about vortex interactions. Uchiyama, Mikkilineni and Wu (1978) developed a computational scheme to predict the flow over wing-body combinations at moderate angles of attack. The body was represented by a system of source/sink elements and the wing by a system of discrete non-intersecting vortex lines. The method was only applied for static cases. Very little details about the flowfield were given. However, this iterative scheme seems to converge very well.

Atta (1978) and Atta and Nayfeh (1978) modified the vortex-lattice method to solve for nonlinear steady flows over wing-body combinations.

The wing and body surfaces were represented by constant strength quadrilateral vortex segments. Separation from the lifting-surface (wing, canard, tail) edges and interference effects were considered in this technique; however, separation from the body and vortex breakdown were not accounted for. The results compared well with some experimental data.

A series of low-speed and high-speed wind tunnel tests for a three surface configuration was conducted by Agnew and Hess (1979) at the McDonnell Aircraft Company. Most of the aerodynamic characteristic measurements were made for the three-surface AFTI-15. The AFTI-15 was derived by adding a close-coupled horizontal canard to the F-15. During more than 500 hours of testing, the effects of canard planform, size, location, and dihedral angle were investigated. Many performance benefits resulting from the interaction of the canard with the wing and with other aircraft control surfaces were reported. The most important effect of the interaction of the canard and the wing, as observed, was a significant increase in lift, especially at maneuvering angles of attack ($\alpha > 10^{o}$). Moreover, the addition of the canard enhanced the effectiveness of the stabilator and the rudder. Wind-tunnel tests were conducted for steady-state motions and for both subsonic and supersonic Mach numbers.

As an application of Forward Sweep Wing (FSW), Spacht (1980) at Grumman Aersopace Corporation tested the FSW Technology Demonstrator aircraft Grumman Design 712; canard-FSW combination. All test measurements confirmed that the configuration performs as designed

across the Mach range and has excellent high-angle-of-attach characteristics.

Croom, Grafton and Nguyen (1982) summarized the results of wind-tunnel tests for two different three-surface configurations based on the F-18 and F-15 designs. They noted that there is strong coupling between canard/wing/empennage flowfields which can result in highly nonlinear aerodynamic characteristics at high angles of attack. It was also found that the canard can strongly influence high-α static stability, damping, and control characteristics.

Very extensive simulation studies of wind-tunnel tests that were performed at NASA-Langley Reserach Center were done by Grafton, Gilbert, Croom and Murri (1982). The main purpose of these tests was to define the high angle-of-attack characteristics of a forward-swept-wing fighter. The X-29A design, which has a close-coupled canard-wing configuration, was used. This work was the first attempt where high angle-of-attack considered with such configuration, i.e., results represented covered the range from $\alpha = 0^{o}$ to $\alpha = 50^{o}$. It was found that adding the canard to the X-29A produces substantial improvements in lift at all angles of attack through maximum lift. Furthermore, the canard enhanced the contributions of the fuselage forebody by increasing the vertical tail effectiveness and hence improving both static and dynamic directional stability. It was noted that above $\alpha = 25^{o}$ the body-wing interference becomes quite strong and stabilizing. Apparently, adding the canard uniformly improved the lateral stability. It was also concluded that the main contribution of the forward-swept wing to the

high angle-of-attack characteristics was the high level of roll control provided by the full-span flaperons.

An investigation similar to the one above was performed by Murri, Croom and Nguyen (1983). They indicated that even though the fuselage forebody contributed to static directional stability, it produced unstable values of damping in roll. They added that the canard not only caused the very high levels of static pitch instability shown by the X-29A model, but it also impressively affected static directional stability, yaw damping, and rudder effectiveness. The forward-swept wing was primarly responsible for the static laterial stability characteristics up to 25° angle of attack; however, at higher angles of attack, these characteristics appear to be affected by the interaction of the body and canard/wing flowfields.

Griffin and Jonas (1983) used the seven-hole pressure probe to experimentaly examine the major pressure and velocity field effects of the interaction between the wake from the canard and the flowfield of the forward-swept wing of the X-29 aircraft. The model used was designed to be tested with or without the canard, so that comparisons could illustrate the canard/wing wake interactions. the investigation discussed in detail the fluid mechanics behind the drastic changes in the total pressure.

Miller and Hadley (1983) and Moore and Frei (1983) and Frei and Moore (1985) applied the concept of forward swept wing in their wind-tunnel experiments. The first group used the F-16A as their model and the later used the X-29. Both investigations summarized how aerodynamic

characteristics are enhanced when combining forward-swept wings and close-coupled, variable-incidence canards in fighter aircraft.

Calarese (1984) in a recent experimental study considered a closely coupled canard-wing configuration. Using hot-wire anemonetry, he measured the Reynolds stresses to illustrate the vortex structure (vortex interaction) at angles of attack of α = 10, 16 and 20 degrees. Eriksson and Rizzi (1984) used a time-marching, finite-volume method to obtain steady-state solutions of Euler's equations for canard-wing interference. They noticed a substantial lift decrease on the main wing when the canard was added. Keither and Selberg (1985) used the vortex-panel and discrete-vortex methods to model canard-wing interference. In their investigation they attempted to determine the aerodynamic effects of gap, stagger, decalage, wing-to-canard area ratio, and aspect ratio as applied to canard/wing configuration. Their model; however, did not account for wing-tip vortex systems or deforming wakes. The recent paper by Er-El and Seginer (1985) describing an experimental study, contains references to earlier works. In this paper Er-El and Seginer considered steady, low subsonic flows. They used a flat delta wing with 60-degree sweep and one of two canard models. One was a delta-shaped canard of 75-degree sweep and the other a moderately swept cropped-arrow-shaped canard of 56-degree sweep. The first was mounted just above the apex of the main wing and second was at two longitudinal locations relative to the wing. Using the Schlieren flow-visualization technique, the authors were able to locate the cores of the leading-edge

vortex systems and determine when and where vortex breakdown occurred. Force and moment measurements were also made during the tests.

The above extensive literature review shows that even though there might be some experimental studies which slightly treated unsteady interference, there were neither numerical nor theoretical methods that fully considered the unsteady aerodynamic interference problem, which is the second part of the present investigation.

1.3 Scope of this Investigation

In this thesis, the problems stated in section 1.1 are treated in a systematic manner.

In Chapter II, the general unsteady vortex-lattice method is described in details. Parameters affecting the accuracy of the method are discussed. The effects of such parameters were not clarified prior to the present study. Numerical examples include flowfields and loads for delta wings.

In Chapter III, equations of three degrees of freedom motion are introduced. A step-by-step general procedure to integrate these equations, based on the predictor-corrector technique, is developed.

In Chapter IV, one-degree and two-degree subsonic wing rock of slender delta wing is considered. Numerical examples for both cases are given for four different angles of attack. Conclusions are drawn.

Finally, in Chapter V, the unsteady vortex-lattice method is extended to treat configurations of multiple close-coupled lifting surfaces. A communication procedure between two or more lifting

surfaces is developed. Numerical examples of steady and unsteady aerodynamic interference are given.

CHAPTER II

DESCRIPTION OF THE UNSTEADY VORTEX-LATTICE METHOD

2.1 Introduction

The numerical procedure models the flow around thin finite wings of arbitrary planform, moving through an inviscid incompressible fluid. When an actual wing moves, it sets the fluid in motion. As a result of viscosity in the real fluid, vorticity is created in the boundary layers on the upper and lower surfaces and vortices are formed along the sharp edges. The latter are shed, convected away from the wing, and form the wake. In the numerical model all the vorticity in the flow is restricted to a thin region around the lifting surface and its wake, and the flow outside this region is considered irrotational.

The wing and its wake are represented by a sheet of vorticity which consists of two parts: the bound vortex sheet that represents the wing and the free vortex sheet that represents the wake. The position of the first is specified; as a result, a finite pressure jump exists across it in general. The position of the second is not specified a priori; it is allowed to deform freely during the motion until it assumes a force-free position. As a result, there is no pressure jump across it. The two parts of the vortex sheet are joined along the sharp edges where separation occurs, the same edges where the Kutta condition is imposed in a steady flow. In the numerical model the vortex sheet is represented by a lattice of discrete vortex lines.

Two coordinate systems are used: one inertial frame of reference (which is called ground-fixed and labelled G-F in this thesis) and one moving frame of reference attached to the wing (which is called body-fixed and labelled B-F in this thesis). If the wing deforms, then the B-F frame is attached to a reference configuration of the wing, and the deformations are described in terms of displacements from this reference configuration. Here only rigid-body motions are considered.

The motion of the wing has, in general, six degrees of freedom: these are the three components of the position vector of the origin of the moving B-F frame (the point is labelled A, the position vector $\vec{R}_A$, and the components X_A, Y_A, Z_A) and a set of three Euler angles (these are labelled ξ, ψ, and θ and are discussed further below). In developing the vortex-lattice method these are considered to be six independent, arbitrary functions of time.

In addition to the motion of the wing being arbitrary, the motion of the ambient fluid may be considered an arbitrary irrotational flow. Here this restriction is imposed in order to use Bernoulli's equation to calculate the pressure and subsequently the loads.

The numerical problem is posed in the B-F frame. The principal advantage of using this frame stems from the fact that the influence coefficients (discussed later) are constant in this frame for rigid wings. If the wings are deforming, the deformations can conveniently be measured from a reference configuration of the wing.

A typical wing and the two coordinate systems are shown in Figure 2.1.

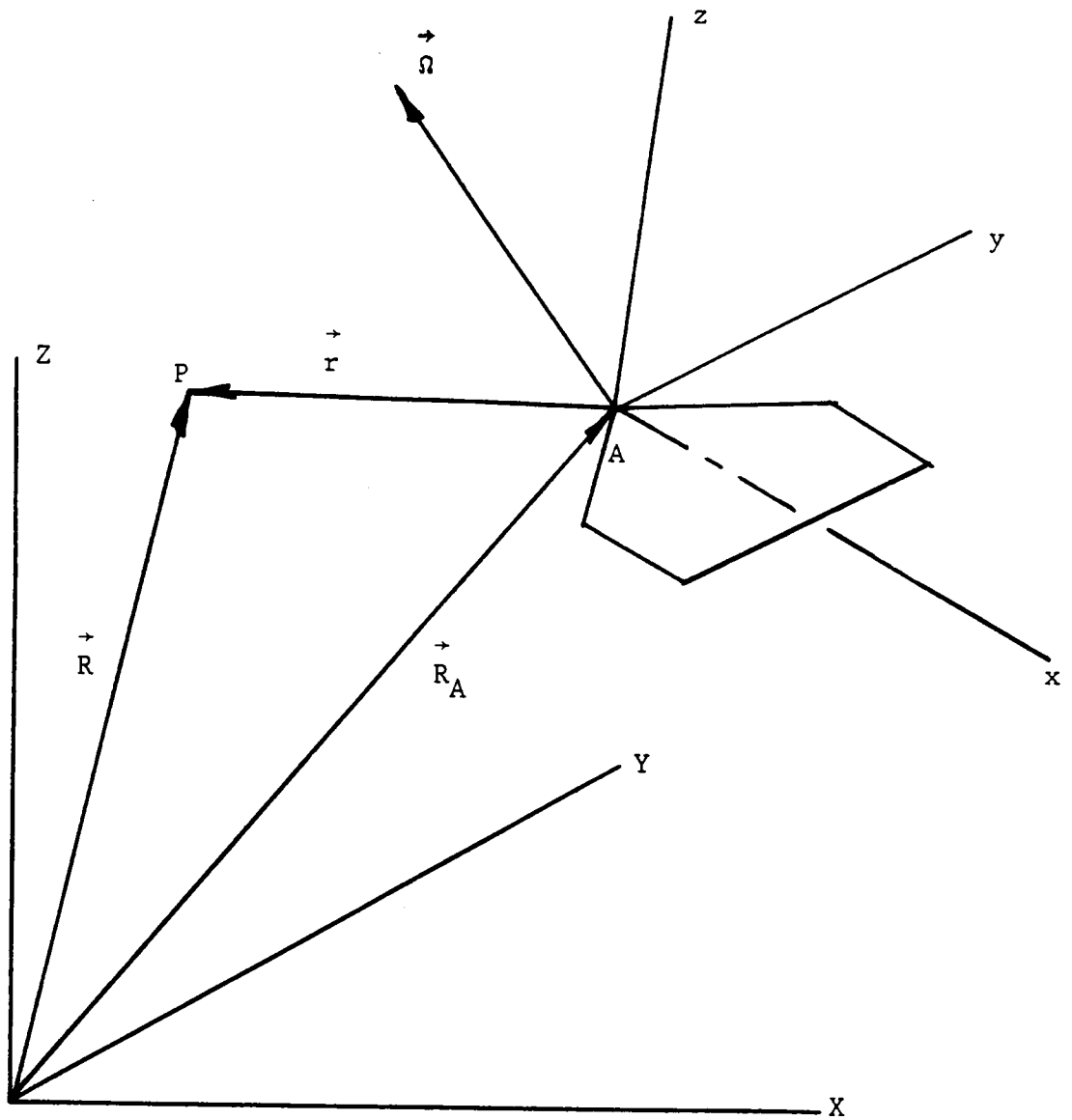

Figure 2.1. Two coordinate systems: global (or ground-fixed denoted XYZ) and local (or body-fixed denoted xyz).

2.2 Euler Angles

Originally the wing is oriented with the coordinate axes in the B-F frame parallel to the corresponding axes in the G-F frame. The following sequence moves the wing to its actual orientation from this reference:

(a) a yaw-like rotation around the original z-axis through the angle ψ followed by

(b) a pitch-like rotation around the new position of y-axis through the angle θ followed by

(c) a roll-like rotation around the final position of the x-axis through the angle ξ.

The base vectors in the G-F frame $(\vec{I},\vec{J},\vec{K})$ are related to those in the B-F frame $(\vec{i},\vec{j},\vec{k})$ as follows:

$$\begin{Bmatrix} \vec{i} \\ \vec{j} \\ \vec{k} \end{Bmatrix} = [C] \begin{Bmatrix} \vec{I} \\ \vec{J} \\ \vec{K} \end{Bmatrix} \quad \text{and} \quad \begin{Bmatrix} \vec{I} \\ \vec{J} \\ \vec{K} \end{Bmatrix} = [C]^T \begin{Bmatrix} \vec{i} \\ \vec{j} \\ \vec{k} \end{Bmatrix} \tag{2.1}$$

where

$$[C] = \begin{bmatrix} C\theta C\psi & C\theta S\psi & -S\theta \\ S\xi S\theta C\psi - C\xi S\psi & S\xi S\theta S\psi + C\xi C\psi & S\xi C\theta \\ C\xi S\theta C\psi + S\xi S\psi & C\xi S\theta S\psi - S\xi C\psi & C\xi C\theta \end{bmatrix} \tag{2.2}$$

and C and S denote the cosine and sine functions.

The angular velocity of the wing is

$$\vec{\Omega} = \Omega_x \vec{i} + \Omega_y \vec{j} + \Omega_z \vec{k} \tag{2.3}$$

where Ω_x, Ω_y, and Ω_z are the components along the B-F axes. These components are related to the derivatives of the Euler angles as follows:

$$\begin{Bmatrix} \Omega_x \\ \Omega_y \\ \Omega_z \end{Bmatrix} = [B] \begin{Bmatrix} \dot{\psi} \\ \dot{\theta} \\ \dot{\xi} \end{Bmatrix} \tag{2.4}$$

where

$$[B] = \begin{bmatrix} -S\theta & 0 & 1 \\ S\xi C\theta & C\xi & 0 \\ C\xi C\theta & -S\xi & 0 \end{bmatrix} \tag{2.5}$$

In the program, the subroutine that converts the derivatives of the Euler angles into the components of the angular velocity along the body-oriented axes is called OMEGAS.

2.3 Velocity of a Point on the Wing

It follows from Figure 2.1 that the position of a point P can be expressed as follows:

$$\vec{R} = \vec{R}_A + \vec{r} \tag{2.6}$$

where $\vec{R}$ is the position of P in the G-F frame, $\vec{R}_A$ is the position of the origin of the B-F frame, and $\vec{r}$ is the position of point P in the B-F frame.

Differentiation of Equation (2.6) yields

$$\vec{V} = \vec{V}_A + \vec{\Omega} \times \vec{r} + \vec{v} \tag{2.7}$$

where $\vec{V}$ is the velocity of point P in the G-F frame, $\vec{V}_A$ is the velocity

of the origin of the B-F frame in the G-F frame, $\vec{\Omega}$ is the angular velocity of the B-F frame and is related to the derivatives of the Euler angles according to Equation (2.5), and $\vec{v}$ is the velocity of point P in the B-F frame (i.e., $\vec{v} = \dot{x}\vec{i} + \dot{y}\vec{i} + \dot{z}\vec{k}$). Equation (2.7) is used later when the procedure for developing the wake (convection of vorticity) is described.

When P is fixed in the surface representing the wing, its velocity relative to the B-F frame is zero; therefore, for points fixed in the surface

$$\vec{V} = \vec{V}_A + \vec{\Omega} \times \vec{r} \tag{2.8}$$

2.4 Representation of the Wing by a Lattice of Discrete Vortex Lines

The wing and its wake are approximated by a sheet of vorticity. The position of the portion of the sheet that represents the wing is specified; hence, this portion is said to be bound. Specifying the position of the vortex sheet, in general, produces a difference in the pressures on the two sides of the sheet. This difference is the basis for predicting the aerodynamic loads on the wing. The position of the portion of the sheet that represents the wake is obtained as part of the solution. Because this position is not specified, it is called free. The position of the wake is determined by the requirement that the difference between the pressures on the two sides of the sheet representing the wake be zero.

The velocity field induced by the wing and its wake is approximated by the velocity field induced by lattices of discrete vortices. Each

segment in the lattices is straight. Figure 2.2 shows the evolution of the numerical model from wing to vortex sheet to vortex lattice.

The velocity field generated by a single, straight vortex segment is given by the Biot-Savart law (Karamcheti, 1966)

$$\vec{V} = \frac{\Gamma}{4\pi h} (\cos\theta_A - \cos\theta_B)\vec{e}_v \qquad (2.9)$$

The terms in Equation (2.9) are identified in Figure 2.3: Γ is the circulation around the vortex segment, which extends from point A to point B. The positive sense for Γ is indicated in the figure; it conforms to the right-hand rule. The parameter h is the distance from point P, where the velocity is being calculated, to the line defined by points A and B. The angles θ_A and θ_B are defined in the figure. And the unit vector $\vec{e}_v$ is perpendicular to the plane defined by the three points - A, B, and P - and in the direction of $\vec{\omega} \times \vec{r}_1$. Both $\vec{\omega}$ (the vorticity) and $\vec{r}_1$ (the position of point P relative to point A) are shown in the figure.

Equation (2.9) is the fundamental building block of the vortex-lattice method. In the computer code, the subroutine that evaluates $\vec{V}$ for a circulation of 4π is called BS1. The parameter list includes the coordinates of points A, B, and P and the three components of $\vec{V}$. The call statement provides the coordinates of the three points, and the subroutine returns the three components of $\vec{V}$.

When P approaches a point between points A and B, the magnitude of $\vec{V}$ approaches infinity. (When P approaches a point on the line defined by points A and B outside the segment between them, the magnitude approaches zero). To eliminate this singularity and to simulate a $\vec{V}$

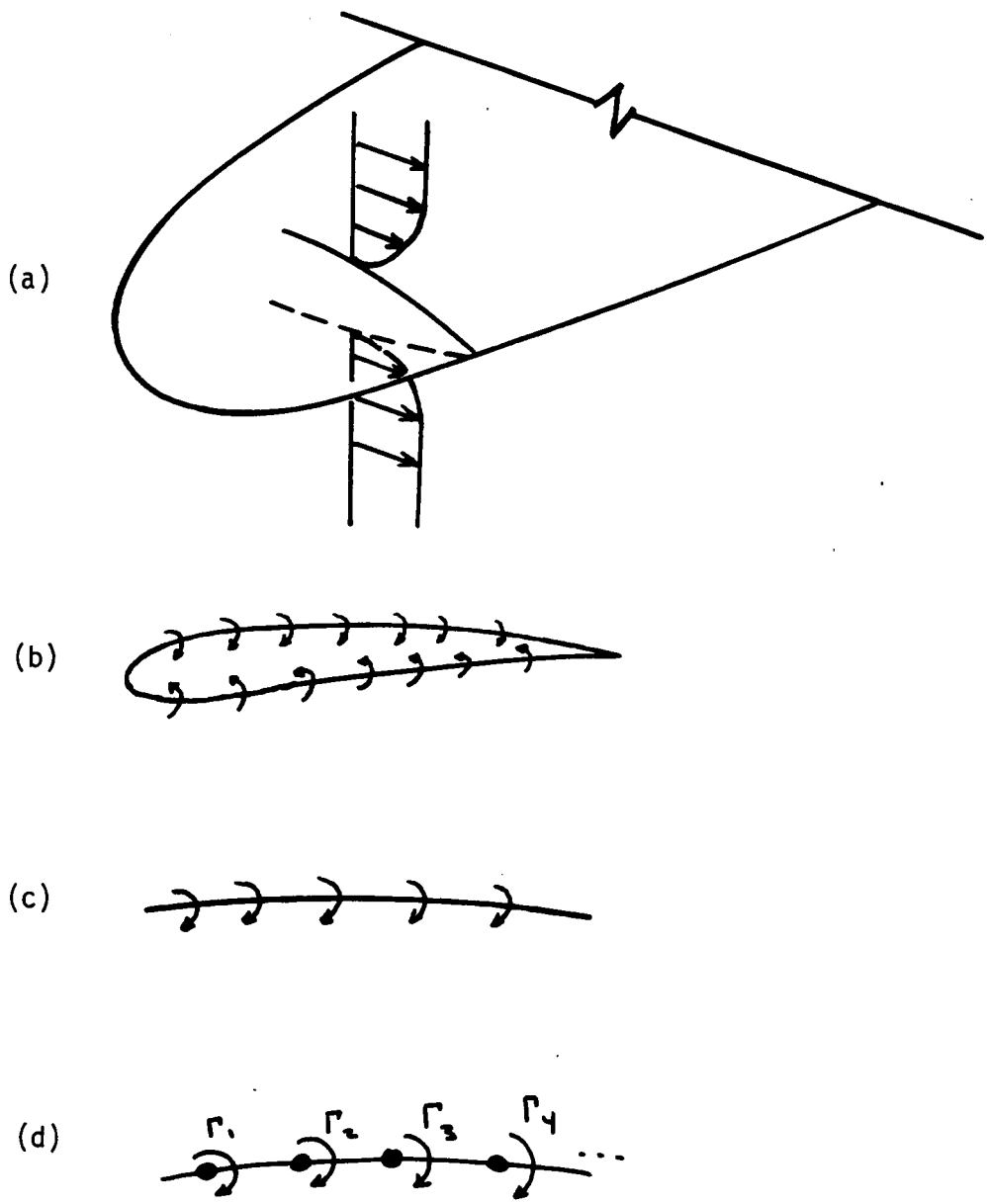

Figure 2.2. The evolution of the numerical model. (a) The actual boundary layers, scale in the normal direction exaggerated. (b) Profile of a section with the boundary layers on the upper and lower surfaces represented by vortex sheets. (c) Upper and lower vortex sheets merged on the camber surface to form a "lifting surface". (d) The single vortex sheet on the camber surface represented by a lattice of discrete vortex lines (sometimes called cores, sometimes simply called vortices). Each segment of the lattice is straight.

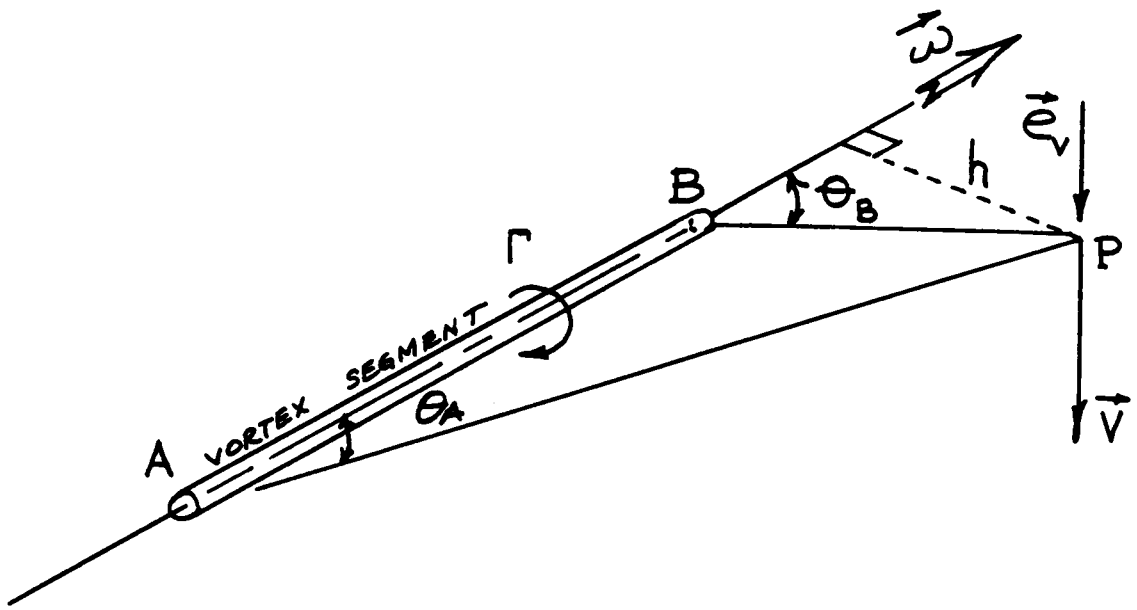

Figure 2.3. A straight segment of a discrete vortex line. The velocity induced by this segment at point P is given by the Biot-Savart law, Equation (2.9).

viscous core, the subroutine returns zero for each of the components of when h is less than a so-called cutoff length. The cutoff length is supplied by the user in the input data. The cutoff length is discussed further later in this thesis.

2.5 Determination of the Governing Equations for the Circulations Around the Discrete Vortex Segments

2.5.1 Spatial Conservation of Circulation

One of the results of the Kelvin-Helmholtz theory of vorticity is that at any instant the circulation around a vortex line is constant (Karamcheti, 1966). The implication of this result is that vortex lines never end. In order to satisfy this requirement the vortex lattice is made of closed loops of constant-circulation vortex lines. These loops enclose the elements of area that make up the bound lattice and the free lattice. Typical loops in the bound and free lattices of a rectangular planform are shown in Figure 2.4. One such loop is A→C→D→B→A, having the circulation G_2 around each of its four vortex segments. The segments A→B and B→D are common to two loops in the bound lattice; consequently, the circulations around these segments are $G_1 - G_2$ and $G_4 - G_2$, respectively.

2.5.2 Infinity Condition

The disturbance created by the wing and its wake must decay as the distance from them increases. Because the disturbance velocity is

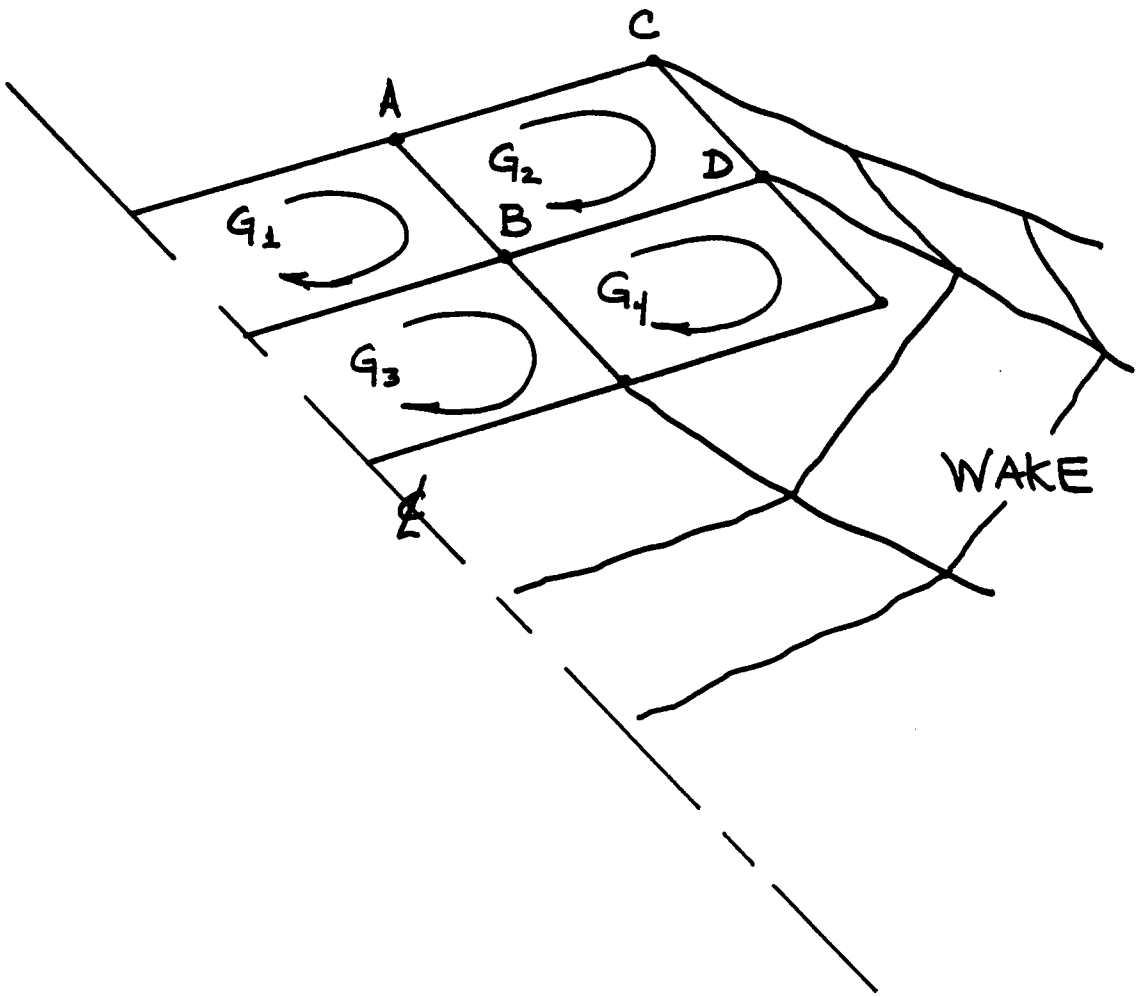

Figure 2.4. A schematic representation of a bound and a free vortex lattice. G_1, G_2, G_3, and G_4 are the values of the circulations around the closed loops of vorticity that form the bound lattice. The circulation is the same for all the segments in a given loop. A→C→D→B→A is an example of a closed loop. Because segment A→B is common to two loops, the circulation around this segment is $G_1 - G_2$.

computed according to the Biot-Savart law, Equation (2.9), this requirement is satisfied.

2.5.3 No-penetration Condition

There is no flow through the surface of the wing (this is often called the no-penetration condition):

$$(\vec{V} - \vec{V}_{LS}) \cdot \vec{n} = 0 \quad \text{everywhere on } S_{LS} \tag{2.10}$$

where $\vec{V}$ is the absolute velocity of the fluid particle in contact with the lifting surface, $\vec{V}_{LS}$ is the velocity of the contact point in the lifting surface ($\vec{V}_{LS}$ is computed from Equation (2.8)), S_{LS} denotes the lifting surface, and $\vec{n}$ is a vector normal to the surface. Because there are only a finite number of loops, and hence only a finite number of unknown circulations, Equation (2.10) can be satisfied at only a finite number of points, not everywhere, on S_{LS}. These points where Equation (2.10) is imposed, called control points, are the centroids of the corners of the rectangular elements and the mid-points of the hypotenuses of the triangular elements along the leading edges of delta wings. The vector $\vec{n}$ is the cross product of the diagonals for rectangular elements and the normal to the plane defined by the three corners for triangular elements.

The velocity of the fluid particle is the sum of two contributions:

$$\vec{V} = \vec{V}_B + \vec{V}_F \tag{2.11}$$

where $\vec{V}_B$ is the velocity induced by the bound lattice (wing) and $\vec{V}_F$ is the velocity induced by the free lattice (wake). The velocity

induced by the wake can be computed from the information obtained at previous time steps or from initial conditions; hence, when starting the motion impulsively $\vec{V}_F$ is zero. This is discussed further in this thesis. Equation (2.10) is replaced with the following:

$$(\vec{V}_B \cdot \vec{n})_i = [(\vec{V}_{LS} - \vec{V}_F) \cdot \vec{n}]_i \qquad (2.12)$$

for i = 1, 2, ..., N. Here i denotes the number of the element and N is the total number of elements in the lifting surface. One equation is written for each element. The velocities are evaluated at the control points.

The normal component of the velocity $\vec{V}_B$ at the control point of element number i is expressed as follows:

$$(\vec{V}_B \cdot \vec{n})_i = \sum_{j=1}^{N} A_{ij} G_j \qquad (2.13)$$

where A_{ij} is the normal component of the velocity induced at the control point of element number i by the vortex loop of circulation 4π around element number j. Substituting Equation (2.13) into Equation (2.12) leads to

$$\sum_{j=1}^{N} A_{ij} G_j = [(\vec{V}_{LS} - \vec{V}_F) \cdot \vec{n}]_i \qquad (2.14)$$

for i = 1, 2, ..., N. Equation (2.14) is used to obtain the unknown circulations G_j. In the program, the subroutine that computes the elements of the influence coefficient matrix A_{ij} is called BINCOF. The subroutine that solves for the G's in Equation (2.14) is called SOLVE.

To start the numerical procedure, one must provide a complete set of initial conditions. These include the positions of all the nodes

(intersections) and the circulations around all the loops in the wake. In addition, one must provide a description of the motion (i.e., $\vec{R}_A$ and the Euler angles as functions of time). Or, in the case where the motion is being determined by numerical integration, one must provide initial values for these quantities and their derivatives. This information is sufficient to compute the right-hand side of Equation (2.14).

2.5.4 The Unsteady Kutta Condition, the Temporal Conservation of Circulation, and the Formation of the Wake

Spatial conservation of circulation dictates that there must be a discrete vortex along the leading and trailing edges. In the case of an impulsive start, this vorticity along the edges is the vortex-lattice simulation of the starting vortex described by Prandtl and Tietjens (1934). Two-dimensional considerations, based on the requirement that the pressures on the upper and lower surfaces be equal along these edges, suggest that these cores be shed into the flowfield (Kim and Mook, 1986). Here the goal is to force the difference in the pressures on the upper and lower surfaces to vanish along the leading and trailing edges. The imposed condition that causes this is called the Kutta condition; generally each numerical model requires its own special statement. The following is the three-point statement of the unsteady Kutta condition appropriate for the vortex-lattice method:

(a) In an unsteady flow, all the vorticity along the edges where the Kutta condition is applied in a steady flow is shed into the flowfield, and in the case of delta wings:

(b) The vortex segments extending from the leading edge into the flowfield are in the plane of the leading-edge element, and

(c) They are perpendicular to the leading edge.

The experiences of Kandil et al (1974) and Kelly (1977) have shown that (b) and (c) lead to accurate results in the case of steady flow and to robust convergence characteristics as the number of elements increases. Hummel's (1979) experimental data seem to show that the vorticity is perpendicular to the leading edge.

Another result from the Kelvin-Helmholtz theory of vorticity (Karamcheti, 1966), is that, in a continuous pressure field where viscous effects are negligible, the circulation around any given loop of fluid particles does not change with time as these particles are convected in the flow:

$$\frac{D\Gamma}{Dt} = 0 \tag{2.15}$$

where $\frac{D}{Dt}$ denotes the substantial (also called material or co-moving) derivative. To satisfy this requirement, the present method computes the velocity at each node and then displaces the nodes according to

$$\vec{r}(t + \Delta t) = \vec{r}(t) + \vec{v}(t)\Delta t$$

$$= \vec{r}(t) + [\vec{V}(t) - \vec{V}_A(t) - \vec{\Omega}(t) \times \vec{r}(t)]\Delta t \tag{2.16}$$

where $\vec{r}(t + \Delta t)$ is the position of the node at the next time step, $\vec{r}(t)$ is the current position and $\vec{v}(t)$ is the current velocity at the current position relative to the moving frame (see Equation (2.7)). The problem

is posed in the moving frame; hence, the change in the position of the wake relative to the B-F frame is computed.

A more accurate formula for the displacement of the nodes is

$$\vec{r}(t + \Delta t) = \vec{r}(t) + \frac{1}{2}\left[\vec{v}(t) + \vec{v}(t + \Delta t)\right]\Delta t \qquad (2.17)$$

where the common symbols are as defined for Equation (2.16) and $\vec{v}(t + \Delta t)$ is the velocity of the node at the next time step when it is in the position $\vec{r}(t + \Delta t)$. Clearly, the position at $t + \Delta t$ must be known before the velocity there can be calculated. As a result, iteration must be used to solve Equation (2.17):

$$\vec{r}_{i+1}(t + \Delta t) = \vec{r}(t) + \vec{v}(t)\,\frac{\Delta t}{2} + \vec{v}_i(t + \Delta t)\,\frac{\Delta t}{2} \qquad (2.18)$$

where $\vec{r}_{i+1}(t + \Delta t)$ denotes the predicted position at $t + \Delta t$ after $i + 1$ iterations while $\vec{v}_i$ denotes the velocity at $\vec{r}_i(t + \Delta t)$. Equation (2.18) is solved repeatedly until there is convergence, Equation (2.16) being used to provide the initial guess. It is noted that each iteration requires a complete solution, the values of the Γ_i at $t + \Delta t$. Consequently, time steps small enough for Equation (2.16) to be accurate are used. Several comparisons of solutions based on both Equations (2.16) and (2.17) suggest that such time steps can be found and that significantly less computing time is required by the use of Equation (2.16). The results presented here were obtained from Equation (2.16).

In the program, the subroutine that convects the nodes of the lattice in the wake is called CNVECT. The convection is effected by a two-step process: First, the velocity is computed at each of the nodes, including those along the edges where vorticity is being shed into the

wake. Separate do-loops cover the leading-edge and trailing-edge portions of the wake. At the same time the velocity of a node is computed, its new position is computed according to Equation (2.16). The new position of each node is stored during this step so that the velocity field in the entire wake is calculated at a given time. Second, each node in the wake is moved to its new position. Again separate do-loops are used for the leading-edge and trailing-edge wakes, just as earlier when the velocity field was computed.

The subroutine that calculates the velocity $\vec{v}$ (see Equation (2.16)) induced at a point by the combined bound and free vortex systems is called VLSEGM.

While the nodes in the free vortex sheet are being convected to their new positions, the circulations around the vortex segments in the wake remain constant in accordance with Equation (2.15). Keeping the circulations around the individual vortex segments in the wake constant while these segments are being convected can be done quite simply: For each of the elements along the edges in the bound lattice where vorticity is being shed, the entire loop is moved, as a single unit, out of the bound lattice and into the free lattice.

The subroutine that moves the vorticity back through the wake at each time step is called RENGES.

2.6 Comments about Various Parameters

There are some parameters or safeguards that vortex-lattice codes must incorporate in order to avoid singularities or other physically

untenable predictions. One such parameter already mentioned in context with the Biot-Savart law is the so-called cutoff length; this and two others are discussed below. In addition, the choice of characteristic length and time are also discussed.

2.6.1 Leading-Edge Extensions

Experience has shown that accurate results and robust convergence as the number of elements increases can be obtained when the vortex segments extending from the leading edge into the flow are perpendicular to the edge, in the plane of the delta wing, and equal in length to the spanwise dimension of one of the rectangular elements.

2.6.2 Cutoff Lengths

The choice of cutoff length can affect the results. Consequently, one must seek a range of lengths in which the results are nearly constant for a given mesh. In the present code the cutoff length is specified in terms of the length of the vortex segment AB (see Figure 2.3).

2.6.3 Prevention of Penetration of the Lifting Surface by Leading-Edge Vortex Lines

Finally, when several rows are used, there is a possibility that one or more of the vortex lines representing the wake may curve sharply and penetrate the surface of the wing. This is possible because the no-penetration condition is satisfied at only the control points. (Indeed,

the normal component of velocity approaches infinity near a discrete vortex core). A statement has been added to the code that does not permit any point in the wake to get closer to the lifting surface than some prescribed value. This length is specified in terms of the chord. For a given mesh, a numerical experiment shows that the distance used here lies in a range for which loads are nearly constant.

2.6.4 Dimensionless Variables

It is convenient to introduce dimensionless variables (denoted by asterisks):

$$\vec{v}^* = \frac{\vec{v}}{U_c} \ , \ \vec{r}^* = \frac{\vec{r}}{L_c} \ \text{ and } \ t^* = \frac{U_c}{L_c} t$$

where U_c and L_c are the characteristic speed and length respectively. Here, U_c is the forward speed of the wing; or in the case when the forward speed is variable, it is a speed characterizing the forward motion; or in the case when the wing is viewed as stationary while the air blows past, it is the speed of the air. And L_c is the chordwise dimension of the rectangular elements in the bound lattice; specifically, it is the actual chord divided by the number of rows of elements.

Dimenionless variables are introduced formally in Section 2.8.3, where the pressure coefficient is developed.

2.6.5 Correspondence Between Time Steps and Mesh Size

Experience has shown that the vortex lattice method yields the best results when the elements in the bound and free lattices are nearly

uniform. This is accomplished by choosing the time step in dimensionless variables to be unity. This can be seen by reconsidering Equation (2.16), which is used to convect nodes in the wakes and which determines the lengths of the elements in the wake:

$$\vec{r}(t + \Delta t) = \vec{r}(t) + \vec{v}(t)\Delta t$$

In dimensionless variables this can be written as follows:

$$\vec{r}^*(t + \Delta t) - \vec{r}^*(t) = \vec{v}^* \Delta t^*$$

where $\vec{v}^*$ is near unity as a result of the definition of characteristic speed; consequently, $\vec{r}^*(t + \Delta t) - \vec{r}^*(t)$ is also near unity when Δt^* is unity.

As a final comment, we recall that

$$\vec{v} = \vec{V} - \vec{V}_A - \vec{\Omega} \times \vec{r}$$

which becomes

$$\vec{v}^* = \vec{V}^* - \vec{V}_A^* - \vec{\Omega}^* \times \vec{r}^*$$

where

$$\Omega^* = \frac{U_C}{L_C} \vec{\Omega} \quad , \quad V_A^* = \frac{V_A}{U_C}$$

and the rest of the variables are as introduced in Section 2.6.4.

2.7 A Numerical Example Illustrating the Procedure to Find the Flowfield

As a further explanation of the procedure a numerical example is considered: the flowfield created by a delta wing of unit aspect ratio

when it undergoes an impulsive start at an angle of attack of 20° and then proceeds at constant velocity.

In Figure 2.5, the bound lattice is shown schematically (not to scale). The unknown circulations around the closed loops of vortex segments are indicated; these are the G's. In Table 2.1 the coordinates of the nodes in the mesh are given; in Table 2.2 the coordinates of the control points, points where the no-penetration boundary condition is imposed, are given; and in Table 2.3 the influence matrix (see Equation (2.13)) is given. All tables give data for a flat, unit-aspect-ratio delta wing. Because the wing is rigid in this example, none of these tables changes.

The subroutine that provides the coordinates of the nodes in both the bound and free lattices and the coordinates of the control points is called COORD.

The results the instant after the impulsive start are given in Figure 2.6. Because the flow is symmetric, only half the wing is shown. The wing is moving at constant unit velocity at 20 degrees angle of attack. The circulations around the vortical segments in the mesh divided by 4π are indicated in the figure. These can be obtained from the values of the G's. In Table 2.4 the values of $G/4\pi$ are given (the factor 4π is not taken into account until the loads are calculated). Here there is no wake; $\vec{V}_F$ is zero in Equation (2.14).

After the G's have been found, the segments along the leading and trailing edges are shed into the wake and convected away at the local

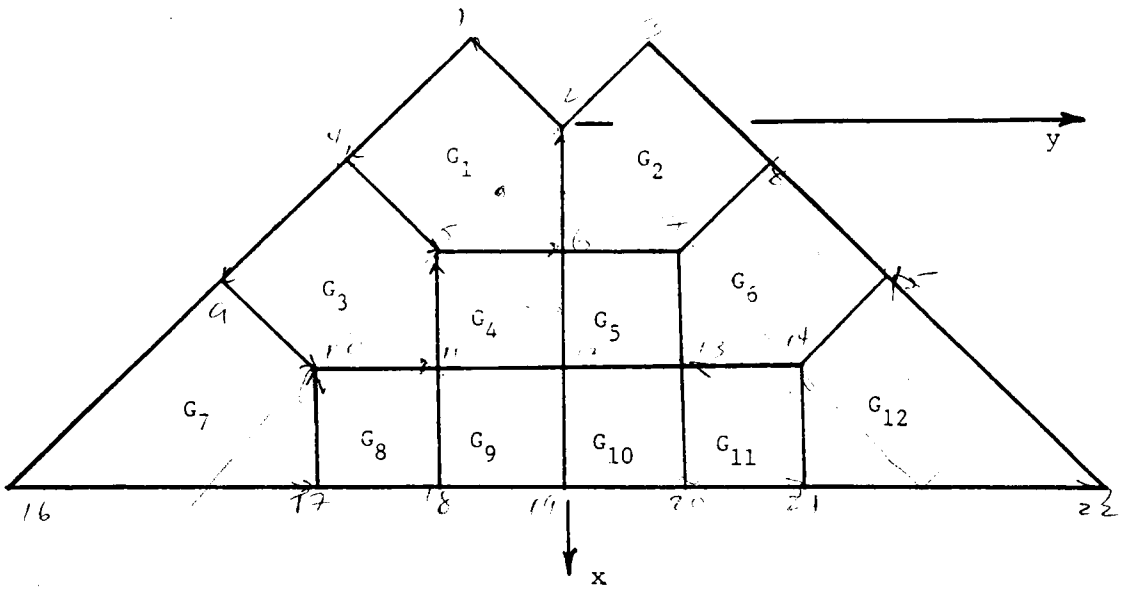

Figure 2.5. Schematic drawing of mesh for a delta wing having 3 rows of elements in the bound lattice. The G's denote unknown circulations around closed vortex loops.

Table 2.1. Coordinates for the three-row mesh of a unit-aspect-ratio delta wing.

Node Coordinates

X	Y	Z
Row #1		
-0.06063	-0.24254	0.0
0.00000	0.00000	0.0
-0.06063	0.24254	0.0
Row #2		
0.93937	-0.49254	0.0
1.00000	-0.25000	0.0
1.00000	0.00000	0.0
1.00000	0.25000	0.0
0.93937	0.49254	0.0
Row # 3		
1.93937	-0.74254	0.0
2.00000	-0.50000	0.0
2.00000	-0.25000	0.0
2.00000	0.00000	0.0
2.00000	0.25000	0.0
2.00000	0.50000	0.0
1.93937	0.74254	0.0
Row #4		
3.00000	-1.00769	0.0
3.00000	-0.50000	0.0
3.00000	-0.25000	0.0
3.00000	0.00000	0.0
3.00000	0.25000	0.0
3.00000	0.50000	0.0
3.00000	1.00769	0.0

Table 2.2. Coordinates of the control points for the delta wing of Table 2.1.

Control-Point Coordinates

CONT. PT. #	X	Y	Z
1	0.50	-0.125	0.0
2	0.50	0.125	0.0
3	1.50	-0.375	0.0
4	1.50	-0.125	0.0
5	1.50	0.125	0.0
6	1.50	0.375	0.0
7	2.50	-0.635	0.0
8	2.50	-0.625	0.0
9	2.50	-0.125	0.0
10	2.50	0.125	0.0
11	2.50	0.375	0.0
12	2.50	0.625	0.0

Table 2.3. The influence matrix A_{ij} (see Equation 2.13) for a unit-aspect-ratio delta wing having 3 rows of elements (see Figure 2.5 and Tables 2.1 and 2.2).

-25.384	10.852	0.499	0.437	0.366	0.326	0.046	0.035	0.035	0.035	0.032	0.041
10.852	-25.384	0.326	0.366	0.437	0.499	0.041	0.032	0.035	0.035	0.035	0.046
0.655	0.344	-25.384	9.826	1.544	0.656	0.501	0.437	0.366	0.243	0.152	0.133
0.687	0.531	10.852	-32.985	9.826	1.869	0.328	0.366	0.437	0.366	0.243	0.206
0.531	0.687	1.869	9.826	-32.985	10.852	0.206	0.243	0.366	0.437	0.366	0.328
0.344	0.655	0.656	1.544	9.826	-25.384	0.133	0.152	0.243	0.366	0.437	0.501
0.053	0.043	0.655	0.243	0.152	0.137	-25.340	9.826	1.544	0.515	0.230	0.165
0.056	0.049	0.687	0.366	0.243	0.215	10.872	-32.985	9.826	1.544	0.515	0.305
0.057	0.054	0.531	0.437	0.366	0.344	1.879	9.826	-32.985	9.826	1.544	0.661
0.054	0.057	0.344	0.366	0.437	0.531	0.661	1.544	9.826	-32.985	9.826	1.879
0.049	0.056	0.215	0.243	0.366	0.687	0.305	0.515	1.544	9.826	-32.985	10.872
0.043	0.053	0.137	0.152	0.243	0.655	0.165	0.230	0.515	1.544	9.826	-25.340

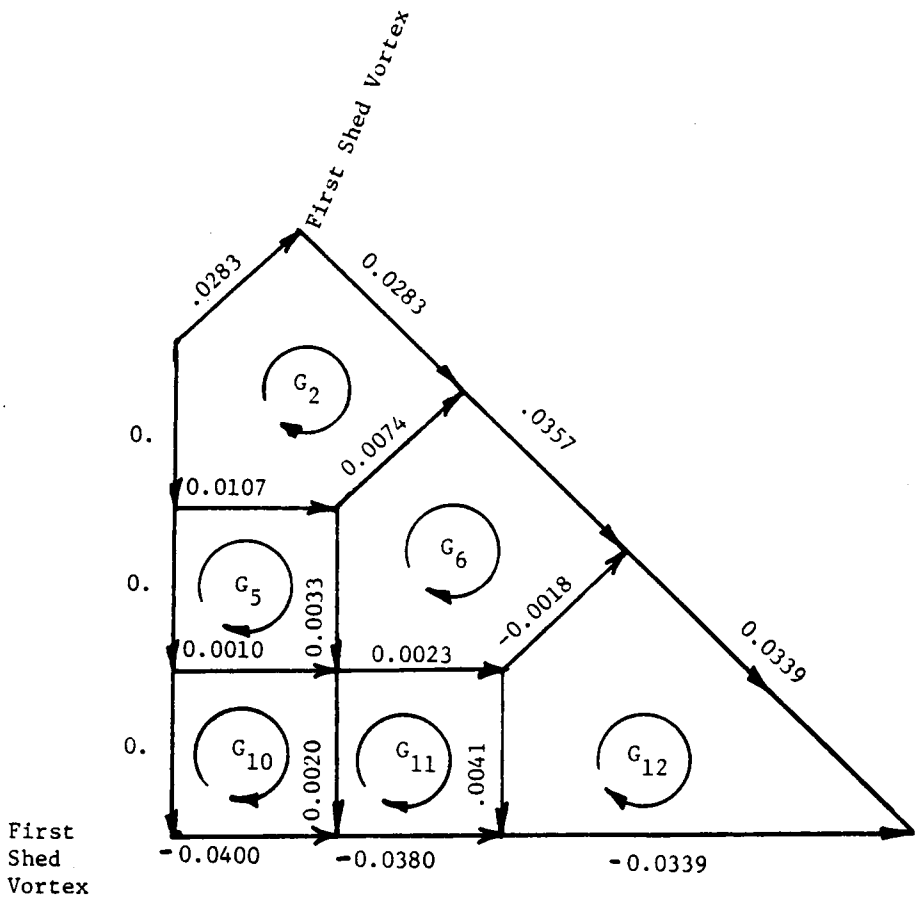

Figure 2.6. Circulations around individual vortex segments at the instant after an impulsive start. Unit-aspect-ratio delta wing at 20° angle of attack.

Table 2.4. The values of $G/4\pi$ for the case described in Figure 2.6.

$G_1 = 0.0282837269$	$G_7 = 0.0338835404$
$G_2 = 0.0282837269$	$G_8 = 0.0380137253$
$G_3 = 0.0356739174$	$G_9 = 0.0399843350$
$G_4 = 0.0390180502$	$G_{10} = 0.0399843350$
$G_5 = 0.0390180502$	$G_{11} = 0.0380137253$
$G_6 = 0.0356739174$	$G_{12} = 0.0338835404$

particle velocity, according to Equation (2.16). Now there is one row of elements around the wing, representing the wake, and $\vec{V}_F$ is no longer zero.

The solution at the next time step is shown in Figure 2.7. The circulations around the individual vortex segments in the wing and its wake are given.

The values of the G's in both the bound and the free lattice are given in Table 2.5. The circulations around the vortex segments that lay along the edges in Figure 2.6 are the same as those around the segments at the edge of the wake (this vortex is marked "First Shed Vortex") here. And the circulations around the loops in the wake here are the same as the circulations around the loops along the leading and trailing edges in Figure 2.6.

After the G's corresponding to Figure 2.7 are found, the segments along the edges and those already in the wake are convected. Then a new $\vec{V}_F$ is calculated and subsequently new G's. The results are shown in Figure 2.8 and given in Table 2.6.

The procedure can be repeated indefinitely. After a certain number of time steps, the first shed vortex no longer significantly affects the conditions on the wing and can be ignored, after the next time step the second shed vortex can be ignored, etc.

The actual results showing the shape of the wake in the steady state are presented in Figure 2.9. These results show a symmetric flow, but the method is not restricted to symmetric flows. The steady-state

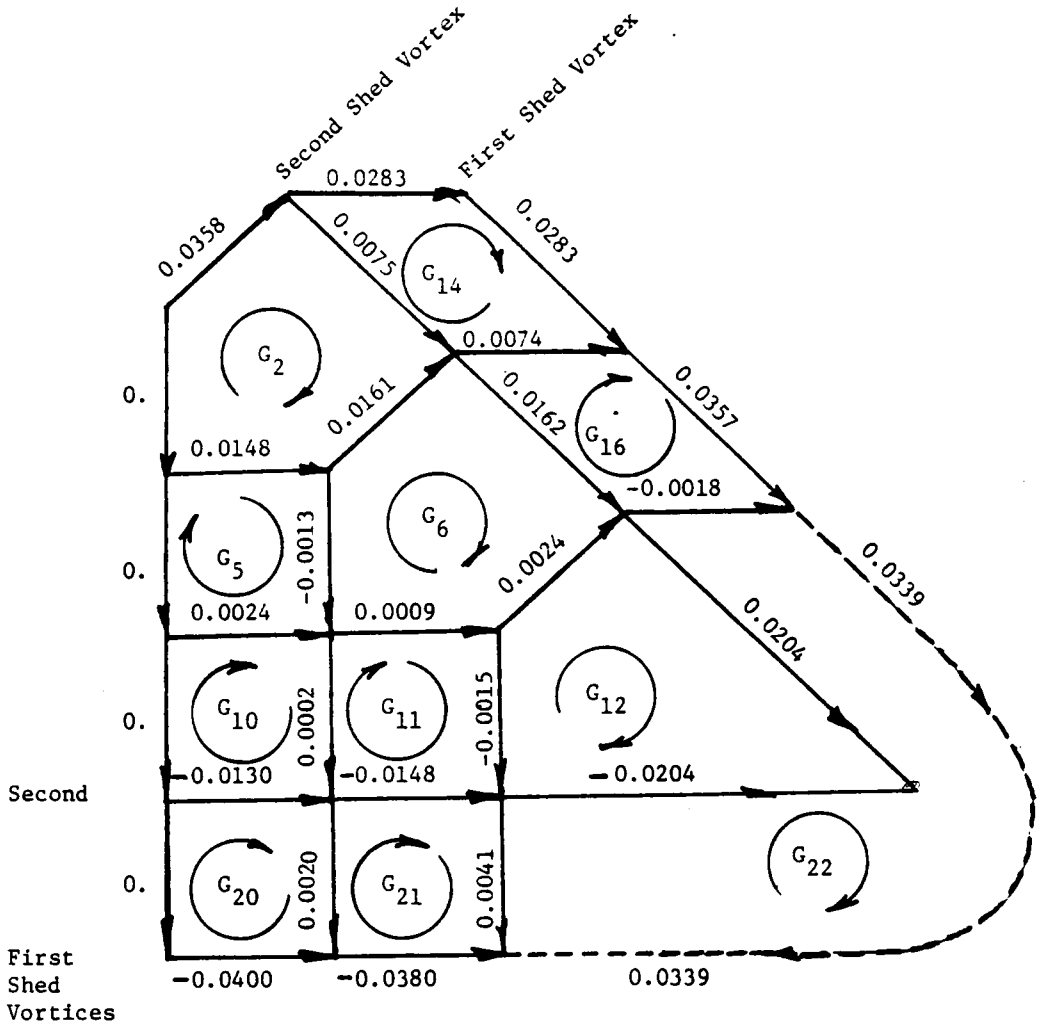

Figure 2.7. Circulations around individual vortex segments one time step after impulsive start.

Table 2.5. The values of $G/4\pi$ for the case described in Figure 2.7.

G_2 = 0.0357958638	G_{14}= 0.0282837269
G_5 = 0.0505862689	G_{16}= 0.0356739174
G_6 = 0.0519090977	G_{20}= 0.0399843350
G_{10}= 0.0529538379	G_{21}= 0.0380137253
G_{11}= 0.0528088195	G_{22}= 0.0338835404
G_{12}= 0.0542843042	

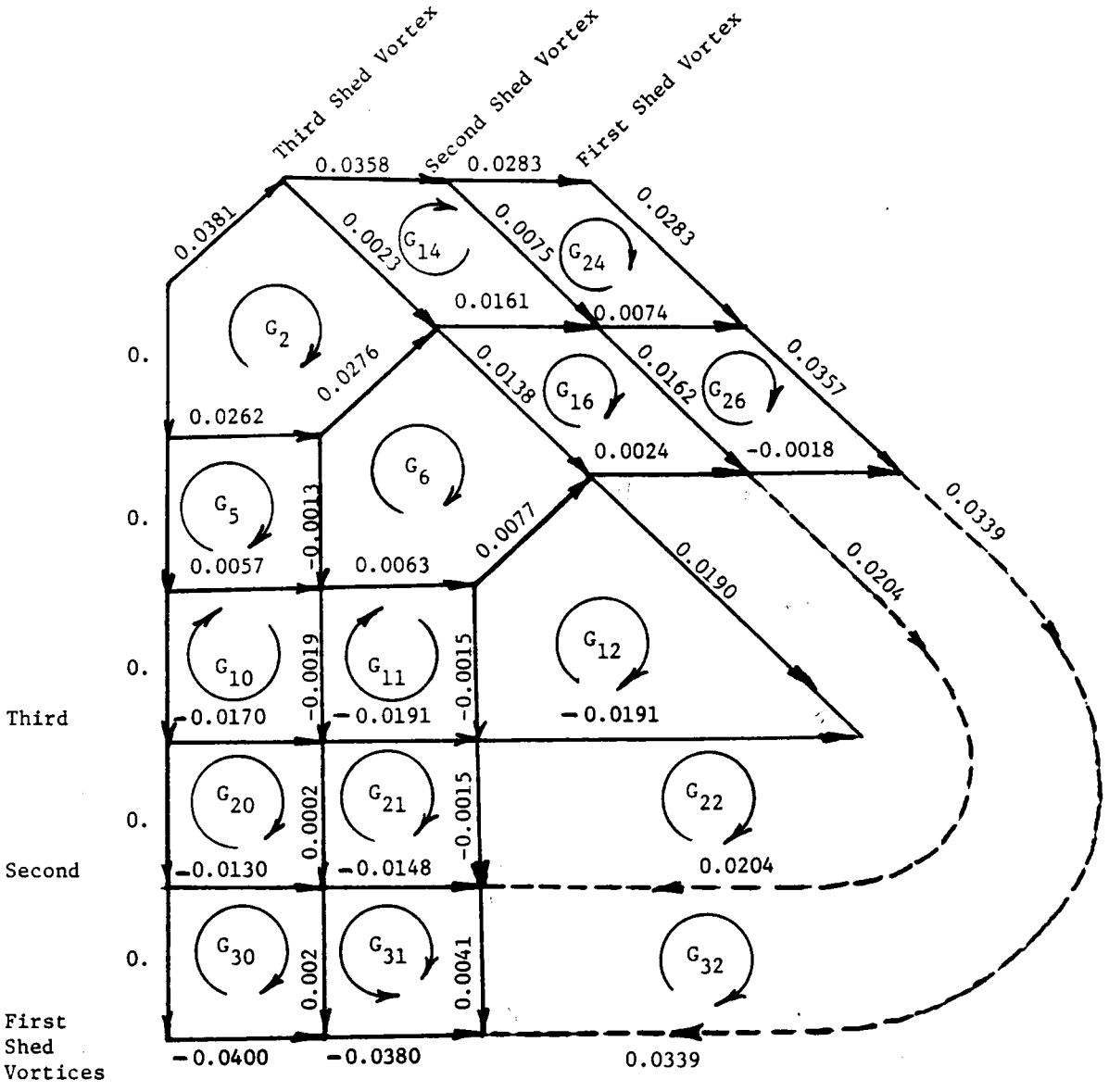

Figure 2.8. Circulations around individual vortex segments two time steps after impulsive start.

Table 2.6. The values of $G/4\pi$ for the case described in Figure 2.8.

G_2= 0.0380939888	G_{14}= 0.035798638	G_{24}= 0.028283727
G_5= 0.0643109862	G_{16}= 0.051909098	G_{26}= 0.035673917
G_6= 0.0656640220	G_{20}= 0.052953838	G_{30}= 0.039984335
G_{10}= 0.069998120	G_{21}= 0.052808820	G_{31}= 0.038013725
G_{11}= 0.071921176	G_{22}= 0.054284304	G_{32}= 0.033883504
G_{12}= 0.073386672		

(a)

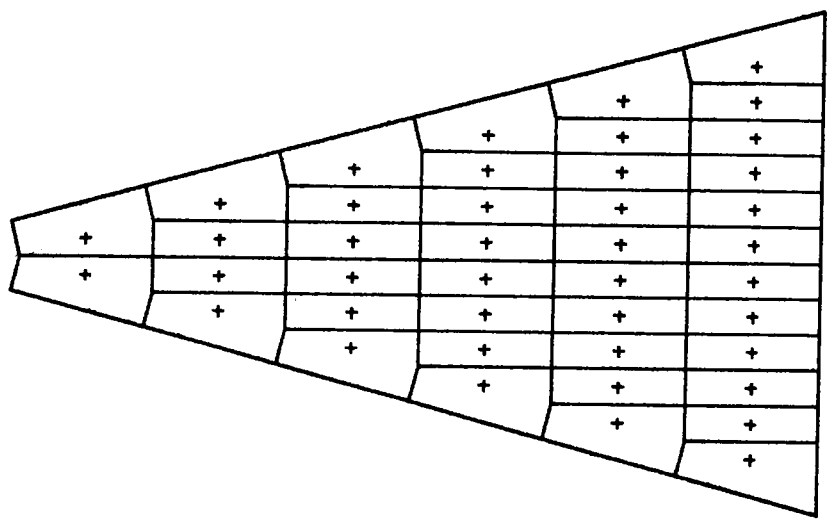

Figure 2.9. Steady-state results for a unit-aspecct-ratio delta wing at 20° angle of attack. Here yaw angle = 0. (a) Actual bound lattice used to make these calculations. (b) Top view in global frame of free lattice. (c) Side view in global frame. (d) End view in global frame.

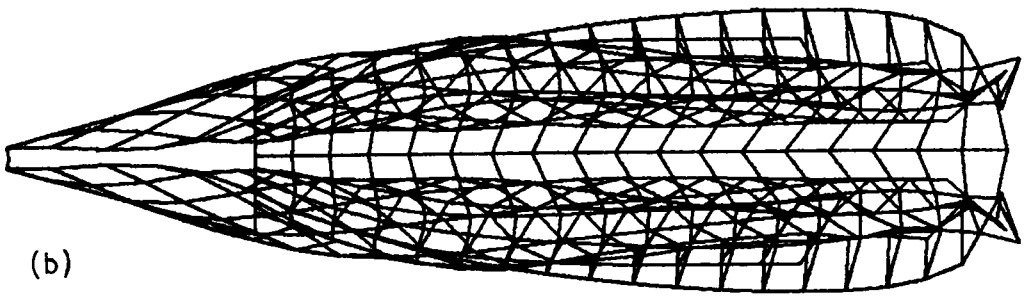

(b)

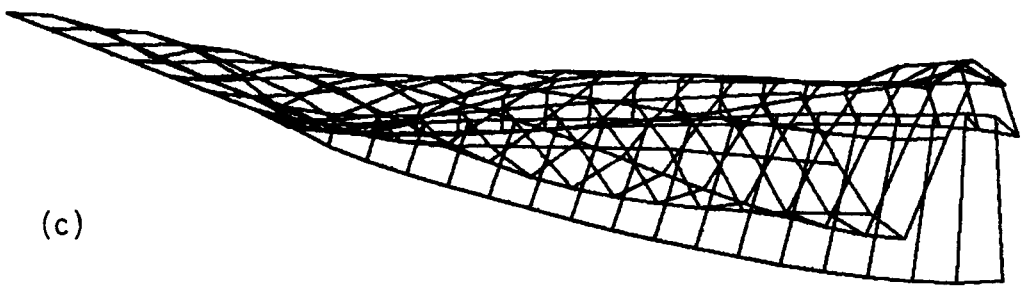

(c)

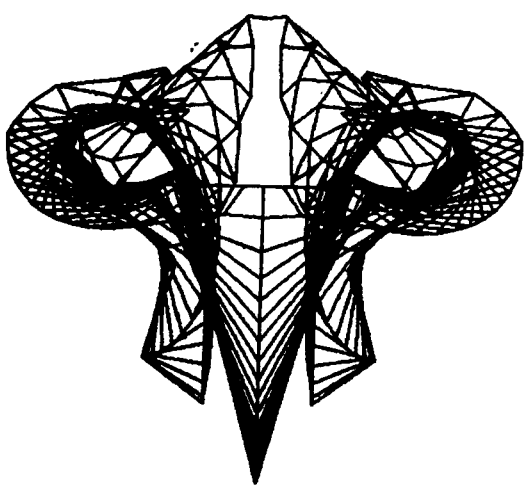

(d)

Figure 2.9. (continued).

results for the same delta wing at an angle of yaw of 10° are shown in Figure 2.10.

2.8 Calculation of Loads

The loads are obtained from Bernoulli's equation. The difference in pressures on the upper and lower surfaces at the control points of the elements is multiplied by the area of the element; the result is a force normal to the element and acting through the control point. These forces are then combined to produce force and moment coefficients.

Bernoulli's equation has the following familiar form for unsteady flows:

$$\frac{\partial \phi}{\partial t}\bigg|_{\vec{R}} + \frac{V^2}{2} + \frac{P}{\rho} = H(t) \qquad (2.19)$$

where ϕ is the velocity potential, V is the magnitude of the velocity in the G-F coordinate system, P is the pressure, ρ is the density, H is a spatially uniform function of time, and $\frac{\partial \phi}{\partial t}\big|_{\vec{R}}$ is the partial derivative holding the position in the G-F frame, $\vec{R}$, constant. If $\vec{R}$ is constant, then the position relative to the B-F frame, $\vec{r}$, is changing as a consequence of the rotation and translation of this frame. The relationships among the various derivatives of ϕ are developed next.

2.8.1 Spatial Derivatives of ϕ

The velocity potential function can be expressed in terms of either $\vec{R}$ (position in the G-F frame) or $\vec{r}$ (position in the B-F frame); here $\Phi(\vec{R},t)$ denotes the former and $\phi(\vec{r},t)$ denotes the latter. When $\vec{R}$ and $\vec{r}$ are positions of the same point, $\phi = \Phi$. The partial derivatives

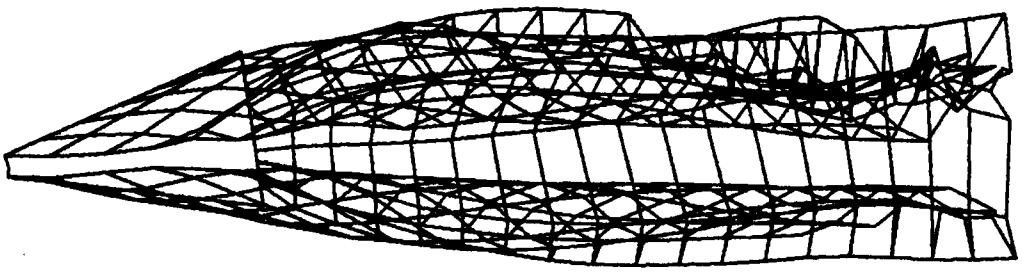

(a)

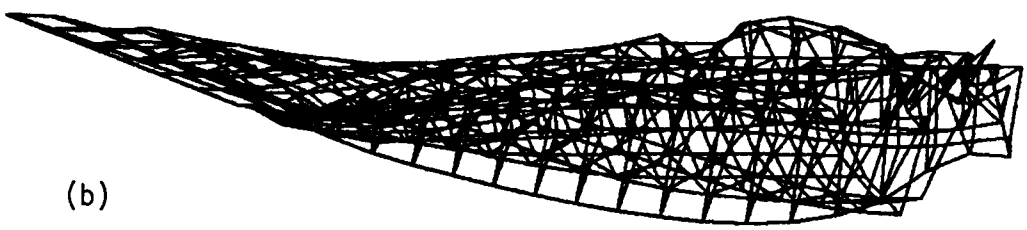

(b)

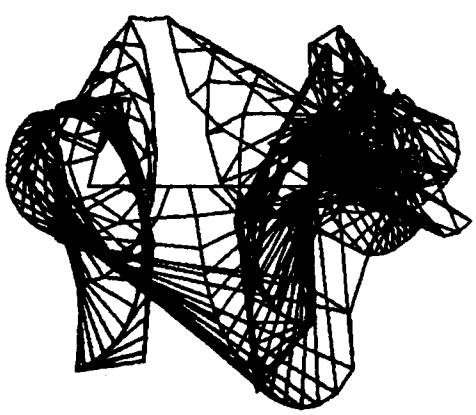

(c)

Figure 2.10. Results for same wing as in Figure 2.9. Here yaw angle = 10°. (a) Top view. (b) Side view. (c) End view.

with respect to position when time is constant (i.e., gradΦ and gradϕ) describe the same velocity:

$$\text{grad } \Phi = \text{grad } \phi = \vec{V} \tag{2.20}$$

where $\vec{V}$ is the absolute velocity (the velocity in the G-F frame). When time is fixed the change in position in the G-F frame equals the change in the B-F frame.

2.8.2 Temporal Derivatives of ϕ

Here the relationship between $\frac{\partial \Phi}{\partial t}$ and $\frac{\partial \phi}{\partial t}$ is determined; the former denotes the derivative of the potential function when $\vec{R}$ is held constant while the latter denotes the derivative when $\vec{r}$ is held constant. If $\vec{R}$ is held constant when time changes, then it follows from Equation (2.6) that $\vec{r}$ must change. In general

$$\frac{d\vec{r}}{dt} = \vec{\Omega} \times \vec{r} + \vec{v}$$

$$= \vec{\Omega} \times \vec{r} + (\dot{x}\vec{i} + \dot{y}\vec{j} + \dot{z}\vec{k}) \tag{2.21}$$

Hence, the change δ in position relative to the B-F frame can be obtained from Equation (2.6):

$$\vec{\delta r} \equiv (\dot{x}\vec{i} + \dot{y}\vec{j} + \dot{z}\vec{k})\Delta t$$

$$= -(\vec{V}_A + \vec{\Omega} \times \vec{r})\Delta t \tag{2.22}$$

Thus,

$$\Delta\phi\Big|_{\vec{R}} = \frac{\partial \phi}{\partial t}\Delta t + \text{grad } \phi \cdot \vec{\delta r}$$

$$\frac{\partial \Phi}{\partial t} = \frac{\partial \phi}{\partial t} - \vec{V} \cdot (\vec{V}_A + \vec{\Omega} \times \vec{r}) \tag{2.23}$$

2.8.3 Bernoulli's Equation for the Body-Fixed Frame in Dimensionless Form

It follows from Equations (2.19) and (2.23) that Bernoulli's equation takes the form:

$$\frac{\partial \phi}{\partial t} - (\vec{V}_A + \vec{\Omega} \times \vec{r}) \cdot \vec{V} + \frac{\vec{V} \cdot \vec{V}}{2} + \frac{P}{\rho} = H(t) \qquad (2.24)$$

Far from the wing and its wake, the fluid is at rest ($V = 0$) and the pressure is constant (P_∞). Thus, Equation (2.24) can be re-written as follows

$$\frac{P_\infty - P}{\rho} = \frac{\partial \phi}{\partial t} + \frac{\vec{V} \cdot \vec{V}}{2} - \vec{V} \cdot (\vec{V}_A + \vec{\Omega} \times \vec{r}) \qquad (2.25)$$

At this point it is convenient to introduce dimensionless variables (denoted by asterisks):

$$\vec{V}^* = \frac{\vec{V}}{U_C}, \quad \vec{r}^* = \frac{\vec{r}}{L_C}, \quad \text{and} \quad t^* = \frac{U_C}{L_C} t \qquad (2.26)$$

where U_C, L_C, and $\frac{U_C}{L_C}$ are the characteristic speed, length, and time (A reference to Table 2.1 shows that L_C is the chordwise length of the rectangular elements in the bound lattice). Equation (2.25) becomes

$$C_p \equiv \frac{P_\infty - P}{\frac{1}{2} P U_2^2} = 2 \frac{\partial \phi^*}{\partial t^*} + \vec{V}^* \cdot \vec{V}^* - 2(\vec{V}_A + \vec{\Omega} \times \vec{r}) \cdot \vec{V}^* \qquad (2.27)$$

where $\phi^* = \frac{\phi}{U_C L_C}$, $\vec{V}_A^* = \frac{\vec{V}_A}{U_C}$, and $\vec{\Omega}^* = \frac{L_C \vec{\Omega}}{U_C}$.

The dimensionless difference between the pressures on the lower and upper surfaces at a control point i is given by

$$\Delta C_{p_i} \equiv \frac{P_\ell - P_u}{\frac{1}{2}\rho U_c^2} = 2\frac{\partial}{\partial t}(\phi_u^* - \phi_\ell^*) + (\vec{V}_u^* \cdot \vec{V}_u^* - \vec{V}_\ell^* \cdot \vec{V}_\ell^*)$$

$$+ 2(\vec{V}_\ell^* - \vec{V}_u^*) \cdot (\vec{V}_A^* + \vec{\Omega}^* \times \vec{r}^*) \qquad (2.28)$$

One can write

$$\vec{V}_u^* \cdot \vec{V}_u^* - \vec{V}_\ell^* \cdot \vec{V}_\ell^* = (\vec{V}_u^* - \vec{V}_\ell^*) \cdot (\vec{V}_u^* + \vec{V}_\ell^*) \qquad (2.29)$$

and

$$\vec{V}_u^* = \vec{V}_m^* + \frac{1}{2}\Delta\vec{V}^* \qquad (2.30)$$

$$\vec{V}_\ell^* = \vec{V}_m^* - \frac{1}{2}\Delta\vec{V}^* \qquad (2.31)$$

where $\vec{V}_m^*$ is the velocity generated by all the vortex segments and $\Delta\vec{V}^*$ is the local discontinuity created by the vortex sheet. We note that $\Delta\vec{V}^*$ can be expressed in terms of the circulations around the element. Both rectangular and triangular elements must be considered.

Rectangular elements are shown in Figure 2.11. Half the circulation around a given segment is associated with the element on either side, and this circulation is considered to be the vorticity times the thickness times the dimension of the element. The y-component of the vorticity times thickness, γ_y, is given by

$$\gamma_y \equiv \Delta V_x^* = \frac{\Gamma_1 + \Gamma_3}{2\ell_x} \qquad (2.32)$$

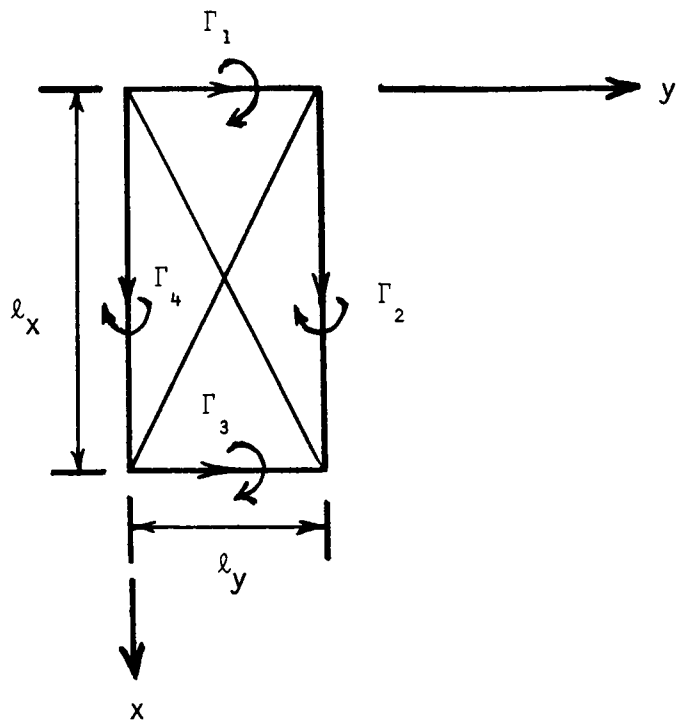

Figure 2.11. Typical rectangular element with nomenclature for pressure calculations.

while the x-component of vorticity times thickness, γ_x, is given by

$$\gamma_x \equiv \Delta V_y^* = - \frac{(\Gamma_2 + \Gamma_4)}{2\ell_y} \tag{2.33}$$

These equations can be combined into a single equation:

$$\vec{\Delta V}^* = - \vec{n} \times [(\Gamma_1 + \Gamma_3)\vec{\ell}_y + (\Gamma_2 + \Gamma_4)\vec{\ell}_x]/2A \tag{2.34}$$

where

$$A = \ell_x \ell_y$$

and $\vec{n}$ is the unit, upward-pointing vector normal to the surface.

Triangular elements are shown in Figure 2.12. Now the discontinuity is taken to be

$$\vec{\Delta V}^* = - \vec{n} \times [(F\Gamma_5 + \Gamma_3)\vec{\ell}_n + \Gamma_4\vec{\ell}_t]/2A \tag{2.35}$$

where on the left-hand side

$$\vec{\ell}_n = DS(\sin\beta\vec{i} + \cos\beta\vec{j})$$

$$\vec{\ell}_t = DP(\cos\beta\vec{i} - \sin\beta\vec{j})$$

and on the right-hand side

$$\vec{\ell}_n = DS(- \sin\beta\vec{i} + \cos\beta\vec{j})$$

$$\vec{\ell}_t = DP(\cos\beta\vec{i} + \sin\beta\vec{j})$$

On both sides

$$A = (DS)(DP)$$

where $DP = \sqrt{1 + DS^2}$

DS = spanwise dimension of the rectangular elements
= 0.25 x (ASPECT RATIO)

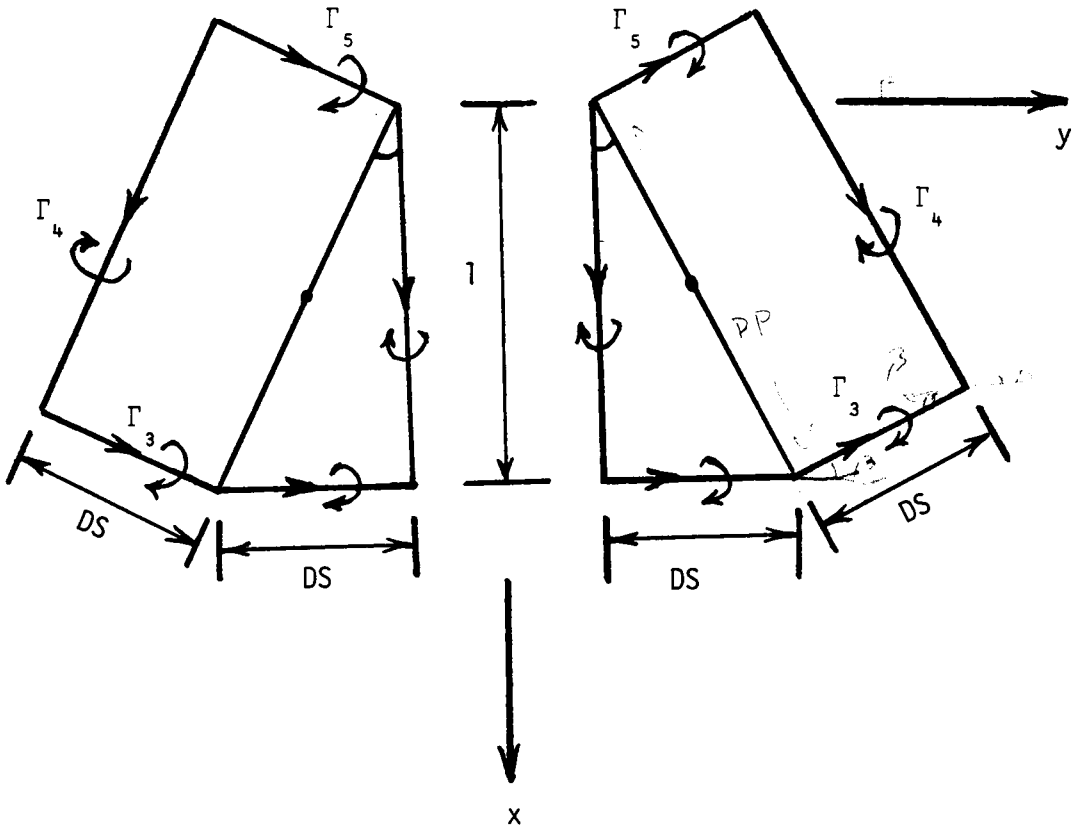

Figure 2.12. Typical triangular elements with nomenclature for pressure calculations.

The factor F is two for elements in the first row and unity for all others. As before $\vec{n}$ is the unit upward-pointing vector normal to the surface.

These values of $\Delta\vec{V}^*$ are substituted into Equations (2.30) and (2.31) and that result is substituted into Equation (2.29). Finally Equation (2.28) can be written in the form

$$\Delta C_{p_i} = 2\frac{\partial}{\partial t}(\phi_u^* - \phi_\ell^*) + 2\Delta\vec{V}^* \cdot (\vec{V}_m^* - \vec{V}_A^* - \vec{\Omega}^* \times \vec{r}^*) \qquad (2.36)$$

The term $(\phi_u^* - \phi_\ell^*)$ can be expressed in terms of the loop circulations, the G's. As an example, the value of $(\phi_u^* - \phi_\ell^*)$ is obtained at the control point of element 5 in Figure 2.5. The change in the value of ϕ^* can be related to a line integral as follows

$$\Delta\phi^* = \int_C d\phi^* = \int_C \text{grad}\ \phi^* \cdot d\vec{r}^* = \int_C \vec{V}^* \cdot d\vec{r}^*$$

The path of integration begins at a point just below the control point of element 5 and runs parallel to the x-axis just below the surface around the leading edge and back along a path just above the surface to a point above the control point of element 5.

From Stokes' theorem it follows that this line integral is equal to the sum of the circulations around the vortex segments encircled by the path. The circulation around the spanwise vortex segment between elements 5 and 2 is $G_5 - G_2$, and for the segment at the leading edge it is G_2. Addition yields

$$\phi_u - \phi_\ell = G_5$$

This result is general so that for any element, say element i,

$$\frac{\partial(\phi_u - \phi_\ell)_i}{\partial t} = \frac{\partial G_i}{\partial t} \tag{2.37}$$

It follows from Equations (2.36) and (2.37) that

$$\Delta C_{p_i} = 2\frac{\partial G_i^*}{\partial t} + 2\Delta \vec{V}^* \cdot (\vec{V}_m^* - \vec{V}_A^* - \vec{\Omega}^* \times \vec{r}^*) \tag{2.38}$$

where $\frac{\partial G_i}{\partial t}$ is evaluated from a two-point finite-difference formula:

$$\frac{\partial G_i}{\partial t}(t) = \frac{G_i(t) - G_i(t - \Delta t)}{\Delta t} \tag{2.39}$$

Equation (2.38) provides the pressure jump across the surface at the control point i. Assuming cambered surface, one can use Equation (2.38) to obtain the elemental force vector, i.e.,

$$\vec{F}_i = \Delta c_{p_i} \cdot A_i \vec{n}_i \tag{2.40}$$

where A_i is the elemental area and $\vec{n}_i$ is the unit normal vector of element i. Equation (2.40) can be rewritten as

$$\vec{F}_i = F_{xi}\vec{i} + F_{yi}\vec{j} + F_{zi}\vec{k} \tag{2.41}$$

Summing the z-component of all forces, the normal-force coefficient can be defined as

$$CN = \frac{\sum_{i=1}^{N} F_{zi}}{S} \tag{2.42}$$

where N is the total number of surface elements and S is the plan area of the surface. Then we introduce Equation (2.41) in G-F frame

$$\vec{F}_i = \begin{Bmatrix} F_{xi} \\ F_{yi} \\ F_{zi} \end{Bmatrix}^T \begin{Bmatrix} \vec{i} \\ \vec{j} \\ \vec{k} \end{Bmatrix} = \begin{Bmatrix} F_{xi} \\ F_{yi} \\ F_{zi} \end{Bmatrix}^T [C_n] \begin{Bmatrix} \vec{I} \\ \vec{J} \\ \vec{K} \end{Bmatrix}$$

or

$$\vec{F}_i^G = \begin{Bmatrix} F_{xi}^G \\ F_{yi}^G \\ F_{zi}^G \end{Bmatrix}^T \begin{Bmatrix} \vec{I} \\ \vec{J} \\ \vec{K} \end{Bmatrix} \tag{2.43}$$

where the superscript G implies forces are in the G-F frame. Again, summing over all surface elements, the drag and the lift coefficients are defined as

$$CD = \frac{\sum_{i=1}^{N} F_{xi}^G}{S} \quad \text{and} \quad CL = \frac{\sum_{i=1}^{N} F_{zi}^G}{S} \tag{2.44}$$

Finally, using Equation (41), the moment-coefficient vector can be defined as follows

$$\vec{CM} = \frac{\sum_{i=1}^{N} \vec{r}_i \times \vec{F}_i}{SC} \tag{2.45}$$

where $\vec{r}_i$ is the vector connecting the control point i and the point about which the moment is taken (usually the origin of the wing), and C is the dimensionless chord. Equation (2.45) can be written as

$$\vec{CM} = CMR\ \vec{i} + CMP\ \vec{j} + CMY\ \vec{k} \tag{2.46}$$

where CMR, CMP, and CMY are the rolling-moment, pitching-moment, and yawing-moment coefficients, respectively.

2.8.4 The Numerical Example Revisited

The wing represented by the lattice in Figure 2.5 is considered again. After the first and second time steps the solution is represented in Figures 2.7 and 2.8 (as discussed before). The differences in pressure across the lifting surface at the control points are given in Table 2.7.

Table 2.7. Pressure discontinuities for the solutions represented in Figures 2.7, $(\Delta C_p)_7$, and 2.8, $(\Delta C_p)_8$. (The dimensionless area is 2.25).

Element No.	$(\Delta C_p)_7$	$(\Delta C_p)_8$
2	1.3079862621	1.4024005588
5	0.4928671347	0.7382642221
6	0.6212959735	0.7864326125
10	0.2020142104	0.3042593314
11	0.2196936717	0.3597969262
12	0.3117787909	0.3878065361

The steady-state values of CN and CMP, normal-force and pitch-moment coefficients, are given in Table 2.8 for three angles of attack and 4 numbers of rows in the lattice. The pairs of numbers in the parentheses of the first column give the number of rows of elements in the wake and the number of time steps used to approximate the steady state. In all cases the wing started impulsively and then maintained a constant angle of attack and velocity. These results show what one can expect convergence as the number of elements increases and as the number of time steps increases. The actual length of the time steps is connected to the number of rows (Section 2.6.4 and 2.8.3); hence time steps needed to reach the steady state increase with the number of rows.

Table 2.8. Steady-state values of normal-force and pitch-moment coefficients for different angles of attack and numbers of rows of elements in the lattice. The pairs of numbers in the parentheses in the first column give the number of rows of elements in the wake and the number of time steps used to establish the steady state. In all cases the minimum distance above the plane of the wing for the vortex line in the wake was 0.05 x chord and the cutoff lengths in the bound and free lattices were 0.1 x (length of the vortex segment). The aspect ratio was unity.

	$\alpha = 10^{\circ}$		$\alpha = 15^{\circ}$		$\alpha = 20^{\circ}$	
Rows	CN	CMP	CN	CMP	CN	CMP
3						
(8,11)	0.256	-0.139	0.455	-0.242	0.689	-0.355
(8,12)	0.255	-0.139	0.456	-0.242	0.686	-0.356
4						
(10,14)	0.279	-0.157	0.495	-0.278	0.751	-0.417
(10,16)	0.279	-0.158	0.497	-0.279	0.756	-0.420
5						
(13,18)	0.304	-0.175	0.518	-0.297	0.774	-0.439
(13,20)	0.304	-0.175	0.519	-0.298	0.778	-0.441
6						
(15,21)	0.332	-0.194	0.542	-0.316	0.787	-0.452
(15,24)	0.333	-0.194	0.543	-0.317	0.790	-0.454

CHAPTER III

DYNAMIC/AERODYNAMIC INTERACTION

3.1 Introduction

The numerical procedure described in this section predicts the motion of the wing, which is caused by the aerodynamic loads acting on it. These loads are obtained by the general unsteady vortex-lattice method described in Chapter II. The problem is complicated by the fact that in order to calculate the loads one must know the motion while to calculate the motion one must know the loads. To avoid an impasse, the present procedure uses iteration.

Because the unsteady vortex-lattice method is designed to use unit steps in time, the present development is based on a Predictor-Corrector Scheme instead of a Runge-Kutta Scheme. The details are provided in Section 3.3 below.

3.2 Equations of Motion

We consider the motion of a thin, flat, uniform wing, supported on a ball-and-socket sting at point c, as shown in Figure 3.1. For such a rigid body, the general vector set of Eulerian Rotational Equations of Motion are of the form

$$\vec{M}_c = I_c \dot{\vec{\Omega}} + \vec{\Omega} \times (I_c \cdot \vec{\Omega}) \qquad (3.1)$$

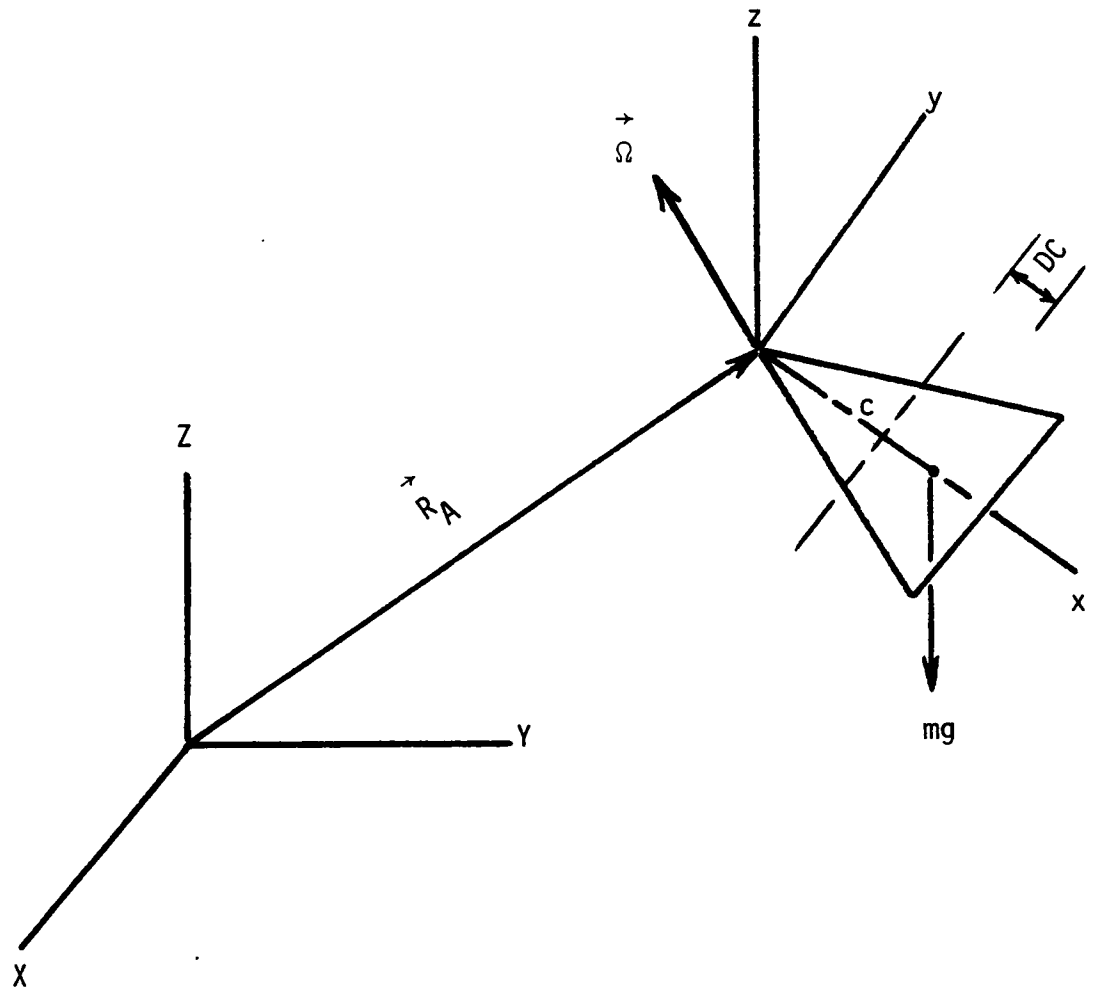

Figure 3.1. Schematic of the delta wing used in the numerical simulation (not to scale).

where $\vec{M}_c$ is the external moment vector around point c, $\vec{\Omega}$ is the angular velocity vector, and I_c is the inertia matrix about point c. For the special choice of principal body-fixed axes,

$$I_c = \begin{bmatrix} I_{xx} & 0 & 0 \\ 0 & I_{yy} & 0 \\ 0 & 0 & I_{zz} \end{bmatrix} ,$$

Equation (1) yields the following equations of motion

$$M_x = I_{xx}\dot{\Omega}_x + (I_{zz} - I_{yy})\Omega_z\Omega_y \tag{3.2a}$$

$$M_y = I_{yy}\dot{\Omega}_y + (I_{xx} - I_{zz})\Omega_x\Omega_z \tag{3.2b}$$

$$M_z = I_{zz}\dot{\Omega}_z + (I_{yy} - I_{xx})\Omega_y\Omega_x \tag{3.2c}$$

where M_x, M_y, M_z are the components of the external moment around point c, $\vec{M}_c$, directed along the body-fixed coordinate axes; Ω_x, Ω_y, Ω_z are the components of the angular velocity of the wing, $\vec{\Omega}$, also directed along the body-fixed coordinate axes; and I_{xx}, I_{yy}, and I_{zz} are the components of the inertia tensor with respect to body-fixed axes having their origin at point c.

The components of $\vec{\Omega}$ can be written in terms of the Euler angles, as given in Equations (2.4) and (2.5). Differentiating these equations, then substituting the result into Equations (3.2), and noting that

$$I_{zz} \approx I_{yy} + I_{xx} , \tag{3.3}$$

we can obtain

$$M_x = I_{xx}(\ddot{\xi} - S\theta\ddot{\psi}) + I_{xx}[C\xi S\xi(C^2\theta\dot{\psi}^2 - \dot{\theta}^2) - 2C\theta S^2\xi\dot{\theta}\dot{\psi}] \tag{3.4}$$

$$M_y = I_{yy}(C\xi\ddot{\theta} + S\xi C\theta\ddot{\psi}) + I_{yy}[S\theta(C\theta C\xi\dot{\psi}^2 - 2S\xi\dot{\theta}\dot{\psi})] \tag{3.5}$$

$$M_z = I_{zz}(C\xi C\theta\ddot{\psi} - S\xi\ddot{\theta}) + I_{xx}[S\theta C\theta S\xi\dot{\psi}^2 - 2S\xi C\theta\dot{\xi}\dot{\psi}$$

$$- 2C\xi\dot{\xi}\dot{\theta}] + I_{yy}[- S\theta C\theta S\xi\dot{\psi}^2 - 2C\xi S\theta\dot{\psi}\dot{\theta}] \tag{3.6}$$

The moments involved here are generated by the aerodynamic forces, whatever small damping there is in the ball and socket, and gravity. The moment due to gravity can be computed as follows:

$$\vec{M}_G = DC\ \vec{i} \times (-mg\vec{K})$$

where DC is the distance between point c and the center of gravity and $\vec{K}$ is the unit vector parallel to the vertical direction. From Equations (2.1) and (2.2), we obtain

$$\vec{K} = - S\theta\vec{i} + S\xi C\theta\vec{j} + C\xi C\theta\vec{k}$$

Then it follows that

$$\vec{M}_G = mg\ DC(C\xi C\theta\vec{j} - S\xi C\theta\vec{k}) \tag{3.7}$$

The damping moment $\vec{D}$ is written as

$$\vec{D} = - \mu_x\Omega_x\vec{i} - \mu_y\Omega_y\vec{j} - \mu_z\Omega_z\vec{k}$$

which can be re-written in terms of the Euler angles as

$$\vec{D} = - \mu_x(\dot{\xi} - S\theta\dot{\psi})\vec{i} - \mu_y(C\xi\dot{\theta} + S\xi C\theta\dot{\psi})\vec{j}$$

$$- \mu_z(C\xi C\theta\dot{\psi} - S\xi\dot{\theta})\vec{k} \tag{3.8}$$

The aerodynamic moment is

$$\vec{A} = \frac{1}{2}\rho U_c^2 SC(C_x\vec{i} + C_y\vec{j} + C_z\vec{k}) \tag{3.9}$$

where ρ is the density of the air, U_c is a characteristic speed, S is the plan area of the wing, C is the chord, and C_x, C_y, C_z are the aerodynammic moment coefficients supplied by the general unsteady vortex-lattice method. C_x, C_y, and C_z are equivalent to CMR, CMP, and CMY, respectively (see Equation (2.46)).

By substituting Equations (3.7)-(3.9) into Equations (3.3)-(3.6) and introducing dimensionless variables, one can obtain

$$\begin{bmatrix} 1 & 0 & -S\theta \\ 0 & C\xi & S\xi C\theta \\ 0 & -S\xi & C\xi C\theta \end{bmatrix} \begin{Bmatrix} \ddot{\xi} \\ \ddot{\theta} \\ \ddot{\psi} \end{Bmatrix} = \begin{Bmatrix} R_x \\ R_y \\ R_z \end{Bmatrix} \tag{3.10}$$

where

$$R_x = C_1 C_x - C_2(\dot{\xi} - S\theta\dot{\psi}) - C\xi S\xi(C^2\theta\dot{\psi}^2 - \dot{\theta}^2) + 2C\theta S^2\xi\dot{\theta}\dot{\psi} \tag{3.11}$$

$$R_y = C_3 C_y - C_4(C\xi\dot{\theta} + S\xi C\theta\dot{\psi}) + C_5 C\xi C\theta - S\theta(C\theta C\xi\dot{\psi}^2 - 2S\xi\dot{\theta}\dot{\psi}) \tag{3.12}$$

$$R_z = C_6 C_z - C_7(C\xi C\theta\dot{\psi} - S\xi\dot{\theta}) - C_8 S\xi C\theta + 2C_9(S\xi C\theta\dot{\psi} + C\xi\dot{\theta})\dot{\xi} - (C_9 - C_{10})S\theta C\theta S\xi\dot{\psi}^2 + 2C_{10}C\xi S\theta\dot{\psi}\dot{\theta} \tag{3.13}$$

and

$$C_1 = \frac{\rho S C L_c^2}{2I_{xx}}, \quad C_2 = \frac{\mu_x L_c}{I_{xx} U_c} \tag{3.14a,b}$$

$$C_3 = \frac{\rho S C L_c^2}{2I_{yy}}, \quad C_4 = \frac{\mu_y L_c}{I_{yy} U_c} \tag{3.14c,d}$$

$$C_5 = \frac{mgDCL_c^2}{I_{yy} U_c^2}, \quad C_6 = \frac{\rho S C L_c^2}{2I_{zz}} \tag{3.14e,f}$$

$$C_7 = \frac{\mu_z L_c}{I_{zz} U_c}, \qquad C_8 = \frac{mg\ DCL_c^2}{I_{zz} U_c^2} \tag{3.14g,h}$$

$$C_9 = \frac{I_{xx}}{I_{zz}}, \qquad C_{10} = \frac{I_{yy}}{I_{zz}} \tag{3.14i,j}$$

Finally, one can solve Equation (3.10) to obtain expressions for the second derivatives of the Euler angles as

$$\begin{Bmatrix} \ddot{\xi} \\ \ddot{\theta} \\ \ddot{\psi} \end{Bmatrix} = \begin{bmatrix} 1 & S\xi S\theta/C\theta & C\xi S\theta/C\theta \\ 0 & C\xi & -S\xi \\ 0 & S\xi/C\theta & C\xi/C\theta \end{bmatrix} \begin{Bmatrix} R_x \\ R_y \\ R_z \end{Bmatrix} \tag{3.15}$$

Equation (3.15) is singular at $\theta = \pm \pi/2$; these values of θ are beyond the range considered here and hence this does not cause problems.

The scheme used to integrate Equation (3.15) numerically treats a system of first-order equations; hence, we must re-write Equation (3.15). To this end, we put

$$Y_1 = \xi, \quad Y_3 = \theta, \quad Y_5 = \psi$$

$$Y_2 = \dot{\xi}, \quad Y_4 = \dot{\theta}, \quad Y_6 = \dot{\psi} \tag{3.16}$$

Then Equation (3.15) can be replaced by

$$\dot{Y}_i = F_i(Y_1, Y_2, Y_3, Y_4, Y_5, Y_6) \tag{3.17}$$

for $i = 1, \ldots, 6$ where

$$\dot{Y}_1 = Y_2 = F_1 \tag{3.18a}$$

$$\dot{Y}_2 = R_X + (SY_1SY_3/CY_3)R_y + (CY_1SY_3/CY_3)R_z = F_2 \tag{3.18b}$$

$$\dot{Y}_3 = Y_4 = F_3 \tag{3.18c}$$

$$\dot{Y}_4 = (CY_1)R_y - (SY_1)R_z = F_4 \tag{3.18d}$$

$$\dot{Y}_5 = Y_6 = F_5 \tag{3.18e}$$

$$\dot{Y}_6 = (SY_1/CY_3)R_y + (CY_1/CY_3)R_z = F_6 \tag{3.18f}$$

and R_x, R_y, R_z, given by Equations (3.11)-(3.13), are also expressed in terms of $Y_1,\ldots, Y_6$. In the above analysis, dots imply derivatives with respect to the nondimensional time $t^* = (U_c/L_c)t$.

3.3 General Concepts of the Predictor-Corrector Technique

In this section we discuss the procedure (Garnahan, 1969) for determining the numerical solutions of systems of first-order equations having the following form:

$$\frac{dY_i}{dt} \equiv \dot{Y}_i = F_i(Y_1,\ldots,Y_N,t) \tag{3.19}$$

for $i = 1,\ldots, N$. The functions F_i can be nonlinear.

To start the general procedure, one must know all the Y_i and F_i at four sequential time steps. Typically, this much initial information is not known, so that one must resort to a special starting procedure then switch to the general procedure. First we discuss the general procedure and then the starting procedure.

3.3.1 General Procedure

We suppose that the Y_i and F_i are known at four previous time steps, and denote these by $Y_{i,j}$; $Y_{i,j-1}$; $Y_{i,j-2}$; $Y_{i,j-3}$; $F_{i,j}$; $F_{i,j-1}$;

$F_{i,j-2}$; $F_{i,j-3}$. We want to compute the values of the Y_i and F_i at the next time step; these values of the Y_i and F_i are denoted $Y_{i,j+1}$ and $F_{i,j+1}$.

Step 1:

A first estimate of the values of the $Y_{i,j+1}$, called the "predicted solutions", is computed according to

$$Y^P_{i,j+1} = Y_{i,j-3} + \frac{4\Delta t}{3}(2F_{i,j} - F_{i,j-1} + 2F_{i,j-2}) \qquad (3.20)$$

Step 2:

The predicted solution is modified according to

$$Y^M_{i,j+1} = Y^P_{i,j+1} + \frac{112}{9} E_{i,j} \qquad (3.21)$$

where $E_{i,j}$ is the vector of "truncation errors" at time step j. The calculation of the $E_{i,j}$ is described below.

When j = 3, there are no values for the $E_{i,j}$, and this step is by-passed; more precisely, the $E_{i,3}$ are set equal to zero.

Step 3:

Iteration is used to solve for the $Y_{i,j+1}$ according to Hamming's "corrector equation"

$$Y^{k+1}_{i,j+1} = \frac{1}{8}[9Y_{i,j} - Y_{i,j-2} + 3\Delta t(F^k_{i,j+1} + 2F_{i,j} - F_{i,j-1})] \qquad (3.22)$$

where k denotes the number of the iteration and

$$F^k_{i,j+1} \equiv F_i(Y^k_{1,j+1}, \ldots, Y^k_{N,j+1}; t + \Delta t) \qquad (3.23)$$

The $Y^M_{i,j+1}$ are used as initial values to start the iterative process. Iteration is continued until a convergence criterion is satisfied.

Step 4:

The vector of truncation errors is computed according to

$$E_{i,j+1} = \frac{9}{121} \left(Y^{k+1}_{i,j+1} - Y^{p}_{i,j+1}\right) \tag{3.24}$$

where the $Y^{k+1}_{i,j+1}$ are the last values computed in Step 3 and the $Y^{p}_{i,j+1}$ are the predicted solution computed in Step 1.

Step 5:

A final modification is made according to

$$Y_{i,j+1} = Y^{k+1}_{i,j+1} - E_{i,j+1} \tag{3.25}$$

Step 6:

The $F_{i,j+1}$ are evaluated using the latest values of the $Y_{i,j+1}$.

Step 7:

The number of the time step is checked against a final value (which is an input) to determine whether the procedure stops or continues. If the procedure continues, the second index on all quantities is shifted and Steps 1-7 are repeated.

3.3.2 Starting Procedure

A complete set of the Y_i and F_i are required to start the numerical integration; these are denoted by $Y_{i,o}$ and $F_{i,o}$. Because the general unsteady vortex lattice method works best with unit time steps, a Runge-Kutta procedure is not used. Instead, we use the following procedure:

Step 1:

Using the known initial conditions (the $Y_{i,o}$ and $F_{i,o}$), we compute the $Y_{i,1}$ and $F_{i,1}$ from

$$Y_{i,1} = Y_{i,o} + \Delta t\, F_{i,o} \tag{3.26}$$

Step 2:

Using the $Y_{i,1}$ just computed, we compute the $F_{i,1}$.

Step 3:

Using the $Y_{i,o}$, $Y_{i,1}$, $F_{i,o}$, and $F_{i,1}$, we compute the $Y_{i,2}$ according to

$$Y_{i,2} = \frac{1}{3}(4Y_{i,1} - Y_{i,o}) + \frac{2\Delta t}{3}(2F_{i,1} - F_{i,o}) \tag{3.27}$$

Step 4:

Using the $Y_{i,2}$ just computed, we compute the $F_{i,2}$.

Step 5:

Using the previously computed $Y_{i,j}$ and $F_{i,j}$, we compute the $Y_{i,3}$ from

$$Y_{i,3} = \frac{1}{11}\left[2Y_{i,o} - 9Y_{i,1} + 18Y_{i,2} + 6\Delta t(F_{i,o} - 3F_{i,1} + 3F_{i,2})\right] \tag{3.28}$$

Step 6:

Finally we compute the $F_{i,3}$.

At this point, we have developed enough information to begin the general procedure. Equations (3.26)-(3.28) can be developed from Taylor series in a very straightforward way.

Next we apply this numerical scheme to the integration of Equation (3.17).

3.4 Numerical Integration of the Equations of Motion

The information needed to start the numerical procedure must include the Euler angles, their derivatives, and the moments; these were

denoted by $Y_{i,o}$ and $F_{i,o}$ in the section above. In addition, the aerodynamic model requires a complete description of the wakes adjoining the leading and trailing edges, which must include positions of the nodes in the lattice and the circulations in the bound lattice representing the lifting surface. With this information available, the numerical integration procedes as follows:

Step 1:

Subroutine OMEGAS is called to provide the components of the angular velocity, $\vec{\Omega}$, along the body-oriented axes, see Equations (2.4) and (2.5).

Step 2:

Subroutine CMATRX is called to obtain the components of the transformation matrix, see Equations (2.1) and (2.2).

Step 3:

Subroutine VELOTR is called to provide the components of the velocity of the origin of the moving frame (Point A in Figure 2.1) along the body-oriented axes. Here we consider the origin of the body-fixed coordinate system to be moving at constant velocity parallel to the ground-fixed X-axis.

Step 4:

The circulation vector, GS is saved so that the derivatives with respect to time can be computed, see Equation (2.39).

Step 5:

Subroutine CNVECT is called to convect the wake to its new position (see Equation (2.16)), the position it will occupy at the end of the first time step.

Step 6:

Subroutine RENGES is called to convect the circulation in the wake. Steps 5 and 6 are done to satisfy the requirements of temporal conservation of circulation dictated by the Kelvin-Helmholtz theory of vorticity.

Step 7:

Subroutine EULER is called to provide the Euler angles and their derivatives at the end of the next time step according to Step 1 of Starting Procedure above.

A DO-LOOP is started here, and this is only the first of four steps. The index of the DO-LOOP is also a parameter in the call statement and determines which step of Starting Procedure is used.

Step 8:

Subroutine OMEGAS is called again.

Step 9:

Subroutine CMATRX is called again.

Step 10:

Subroutine VELOTR is called again.

Step 11:

Subroutine OBBVEC is called to provide the normal component of the velocity of the lifting surface at the control points (see Equation

(2.14): OBBVEC provides $\vec{V}_{LS} \cdot \vec{n}$ at each control point). These are stored in the vector OBB(I).

Step 12:

Subroutine WINCOF is called to provide the normal component of the velocity induced by the wake at the control points (see Equation (2.14): WINCOF provides $\vec{V}_F \cdot \vec{n}$ at each control point). These are stored in the vector OBW(I).

Step 13:

The two vectors that make up the right-hand side of Equation (2.14) are added.

Step 14:

Subroutine SOLVE is called to obtain the circulations in the bound lattice at the new time. These are stored in the vector GS(I).

Step 15:

Subroutine DLOAD is called to provide the aerodynamic loads at the new time step. Everything is known at the new time. Although this is not the end of the DO-LOOP, the new time step begins.

Step 16:

Subroutine FTERM is called to provide the right-hand sides of the governing equation from the loads, angles, derivatives, damping coefficients etc., see Equation (3.17).

Step 17:

Subroutine CNVECT is called.

Step 18:

Subroutine RENGES is called. This step is the end of the DO-LOOP that performs the starting procedure. After four passes through this DO-LOOP, enough information has been generated to begin the general procedure.

Step 19:

Subroutine PRAMOD is called. This subroutine performs Steps 1 and 2 of General Procedure above; it predicts and modifies. This step essentially begins a new DO-Loop.

Step 20:

Subroutine OMEGAS is called. This subroutine uses the values of the Euler angles and their derivatives, just provided by PRAMOD, to find the components of the angular velocity in the body-fixed axes.

Step 21:

Subroutine VELOTR is called.

Step 22:

Subroutine OBBVEC is called.

Step 23:

Subroutine WINCOF is called.

Step 24:

Subroutine SOLVE is called.

Step 25:

Subroutine DLOAD is called. At this point the bound circulations and loads corresponding to the modified predicted solution are known.

The iterative procedure, Step 3 of General Procedure above, is about to begin.

Step 26:

Subroutine FTERM is called.

Step 27:

Subroutine YFITER is called, which performs Step 3 in General Procedure.

Step 28:

The maximum difference between the solutions for two successive iterations is compared to an allowable tolerance, which is input. If the difference is greater than the tolerance, the program shifts back to Step 20. If the difference is less, then the program procedes to Step 29.

Step 29:

Subroutine ERAFM is called, which computes the vector of truncation errors and the final modification. At this point the values of the Euler angles and their derivatives are known, but as a result of the final modification, the vector of circulations GS(I) and the loads must be calculated.

Step 30:

Subroutine OMEGAS is called.

Step 31:

Subroutine CMATRX is called.

Step 32:

Subroutine VELOTR is called.

Step 33:

Subroutine OBBVEC is called.

Step 34:

Subroutine WINCOF is called.

Step 35:

Subroutine SOLVE is called.

Step 36:

Subroutine DLOAD is called.

Step 37:

Subroutine FTERM is called. These will be used in PRAMOD in the next time step.

Step 38:

The vector GS(I) is saved so that the derivative can be calculated by a finite-difference formula at the next time step.

Step 39:

Subroutine CNVECT is called. As before, this step begins the calculation at the next time.

Step 40:

Subroutine RENGES is called. This ends the DO-LOOP, and the program shifts back to Step 19 above.

CHAPTER IV

NUMERICAL EXAMPLES OF DYNAMIC/AERODYNAMIC INTERACTION: SUBSONIC WING ROCK OF SLENDER DELTA WINGS

4.1 Introduction

The numerical procedure described in Chapter III is used to predict the response of a slender delta wing to initial disturbances. The properties of the wing are nearly the same as those of the wing used by Levin and Katz (1982) in their wind-tunnel experiment. Their experiment considered a wing that was free to roll. Here we consider a wing that is free to roll and pitch. The hinge for rotation in pitch is located so that the wing is in equilibrium at 25 degrees angle of pitch (attack) when the air speed is 16.1 m/s. This permits a direct comparison between the numerical results for roll only and the experimental data of Levin and Katz at this angle of attack.

4.2 Equations of Motion

The equations of motion for three degrees of freedom, Equation (3.15), are reduced as follows: For two degrees of freedom,

$$\psi \equiv \dot{\psi} \equiv \ddot{\psi} \equiv 0 \tag{4.1}$$

Then it follows that

$$R_y S\xi + R_z C\xi = 0 \tag{4.2}$$

Hence,

$$\ddot{\xi} = R_x \tag{4.3}$$

and

$$\ddot{\theta} = R_y C\xi - R_z S\xi \tag{4.4}$$

From Equation (4.2) it follows that

$$\ddot{\theta} = R_y / C\xi \tag{4.5}$$

The quantities R_x, R_y, and R_z are defined in Equation (3.11)-(3.13). For this case, R_x reduces to

$$R_x = C_1 C_x - C_2 \dot{\xi} + C\xi S\xi \dot{\theta}^2 \tag{4.6}$$

and R_y reduces to

$$R_y = C_3 C_y - C_4 C\xi \dot{\theta} + C_5 C\xi C\theta \tag{4.7}$$

The coefficients are defined in Equations (3.14).

For one degree of freedom,

$$\theta \equiv \dot{\theta} \equiv \ddot{\theta} \equiv 0 \tag{4.8}$$

in addition to Equation (4.1) above. R_x reduces to

$$R_x = C_1 C_x - C_2 \dot{\xi} \tag{4.9}$$

and ξ is still governed by Equation (4.3).

4.3 Physical Parameters

Chord = 0.429 m

Leading-edge-sweep angle = 80 degrees

Aspect ratio = 0.705

Area = 0.324×10^{-1} m^2

Mass = 0.284 kg

$$DC = 0.737 \times 10^{-1} \text{ m}$$

$$I_{xx} = 2.7 \times 10^{-4} \text{ kg-m}^2$$

$$I_{yy} = 0.44 \times 10^{-2} \text{ kg-m}^2$$

$$I_{zz} = 0.47 \times 10^{-2} \text{ kg-m}^2$$

$$\rho_{air} = 0.12 \times 10^{-2} \text{ kg/m}^3$$

Levin and Katz (1982) gave only the value of I_{xx}. Here we have estimated the corresponding values of mass, I_{yy}, and I_{zz} by assuming the wing to be a thin, flat, uniform plate. (The actual wing had a hump in the center that housed the bearing assembly of the free-to-roll sting).

4.4 Numerical Results

Here we consider four angles of attack: α = 15 degrees, a stable angle; α = 20 degrees, a borderline unstable angle; α = 22.5 degrees, an angle for which in essence only roll is excited; and α = 25 degrees, an angle for which both roll and pitch are strongly excited.

4.4.1 α = 15 Degrees

Here we choose the freestream speed to be

$$U_\infty = 22.1 \text{ m/s} \tag{4.10}$$

and the damping coefficients to be

$$\mu_x = 0.378 \times 10^{-4}, \quad \mu_y = \mu_z = 0 \tag{4.11}$$

The coefficients become

$$C_1 = 0.354 \tag{4.12a}$$

$$C_2 = 0.678\times10^{-3} \tag{4.12b}$$

$$C_3 = 0.0215 \tag{4.12c}$$

$$C_4 = 0. \tag{4.12d}$$

$$C_5 = 0.108\times10^{-2} \tag{4.12e}$$

For this choice of freestream speed, the wing is in equilibrium at 15 degrees angle of attack.

The results for one degree of freedom in roll are given in Figure 4.1. In part a, the roll angle is shown as a function of time, and in part b, the phase plane is given. Clearly, the response to an initial disturbance (here ξ = 5 degrees and $\dot{\xi}$ = 0 at time = 0) decays with time. The roll-moment, pitch-moment, and normal-force coefficients are given as functions of time in parts c, d, and e, respectively. These results are typical. In fact, the motion decays for all the initial conditions considered.

The results for one degree of freedom in pitch also show a decay. Results for α = 25 degrees are discussed in Section 4.4.4. These are typical of all angles of attack.

The results for two degrees of freedom (roll and pitch) are given in Figure 4.2. In part a, the roll angle is shown as a function of time. Again the disturbance decays. Decay is also indicated by the results shown in part b giving the deviation of the pitch angle from its equilibrium position as a function of time. The phase plane for roll, roll-moment, pitch-moment, and normal-force coefficients are given in parts c, d, e and f, respectively.

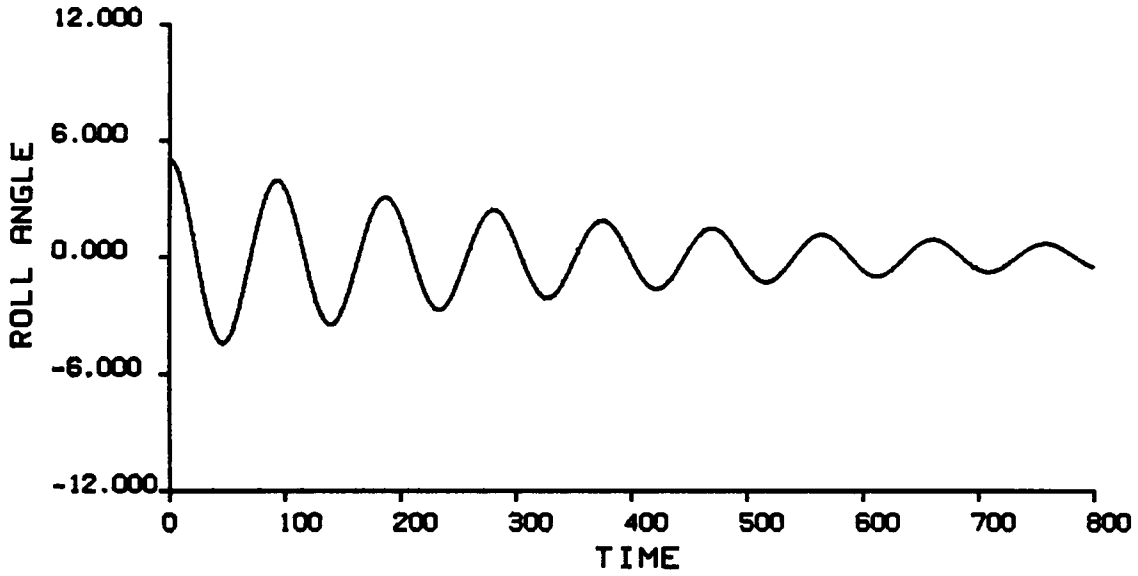

(a)

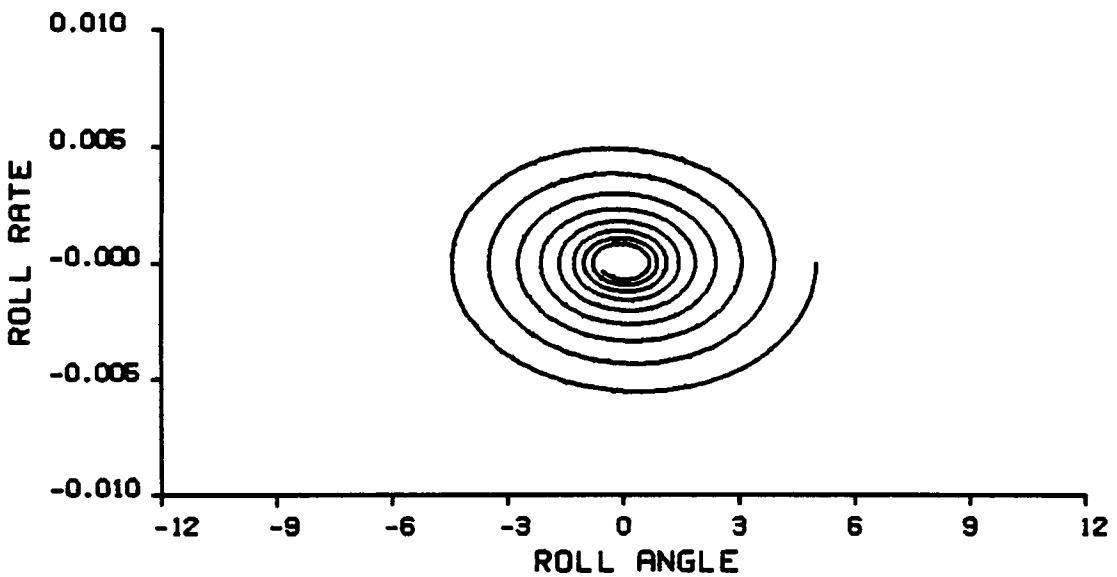

(b)

Figure 4.1. Numerical results for one degree of freedom in roll, $\alpha = 15°$, $\xi(0) = 5°$, $\dot{\xi}(0) = 0$:
(a) Roll angle as a function of time.
(b) Phase plane.

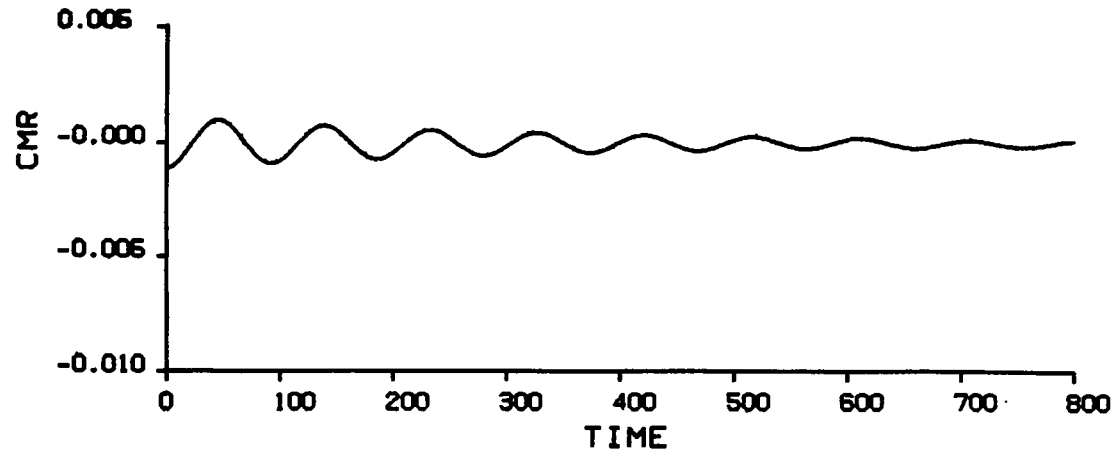

(c)

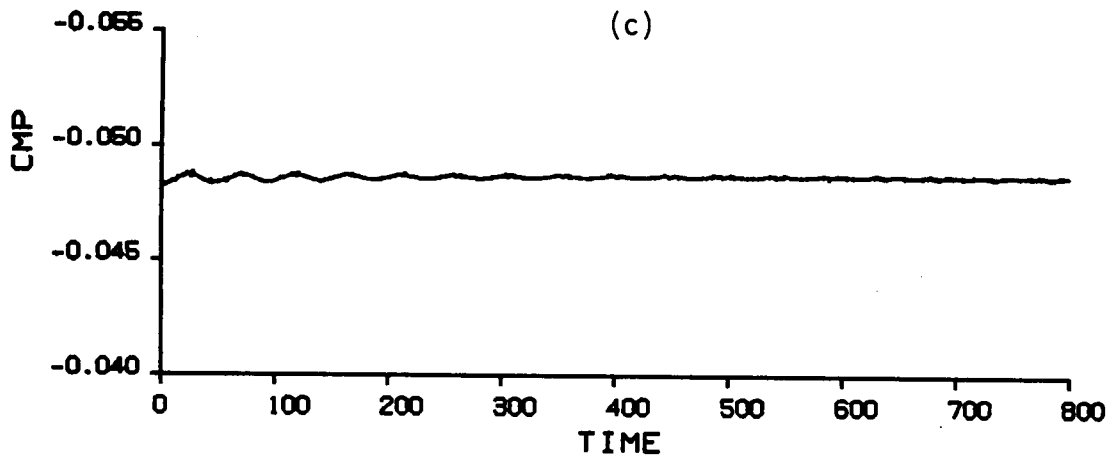

(d)

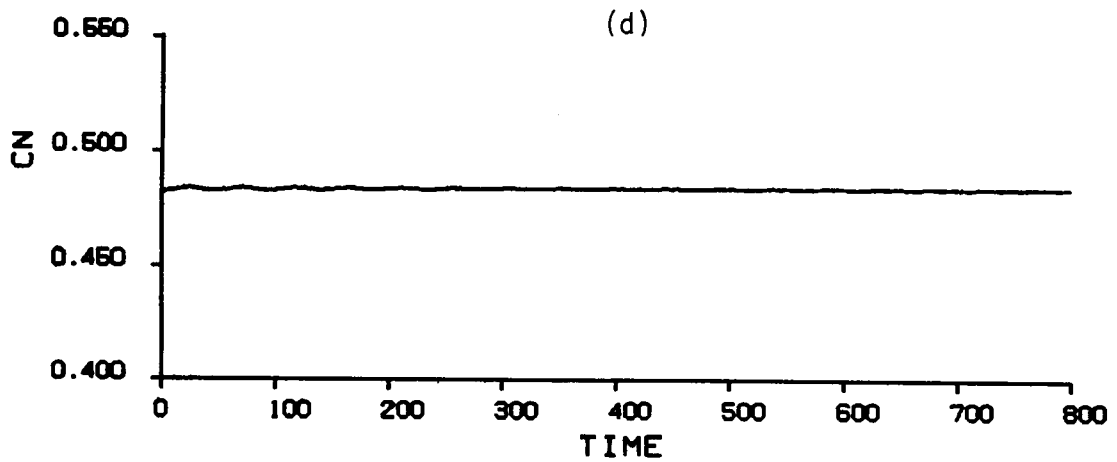

(e)

Figure 4.1. (c) Roll-moment coefficient as a function of time.
(d) Pitch-moment coefficient as a function of time.
(e) Normal-force coefficient as a function of time.

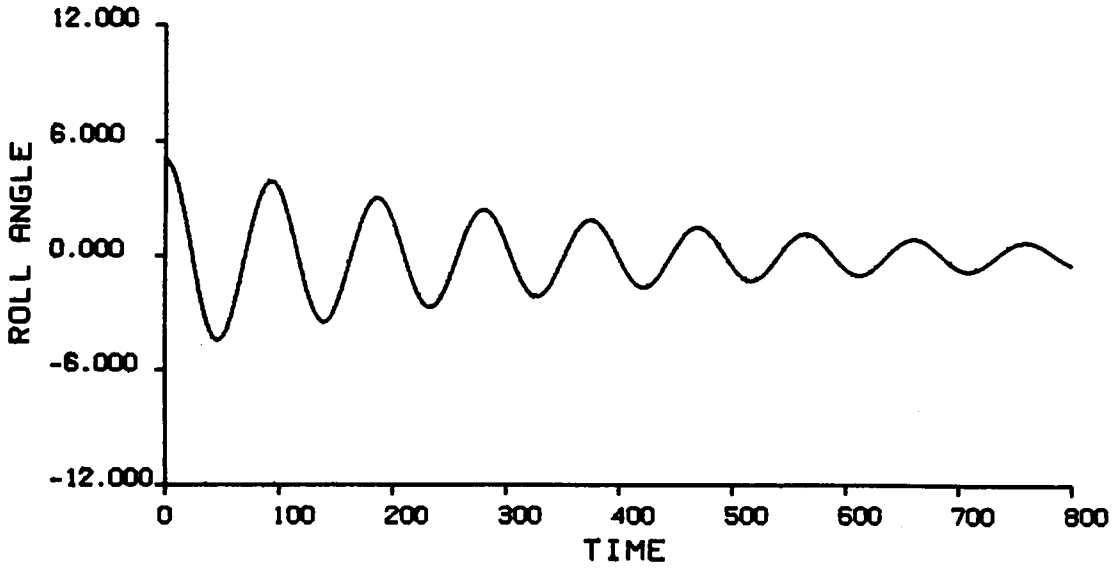

(a)

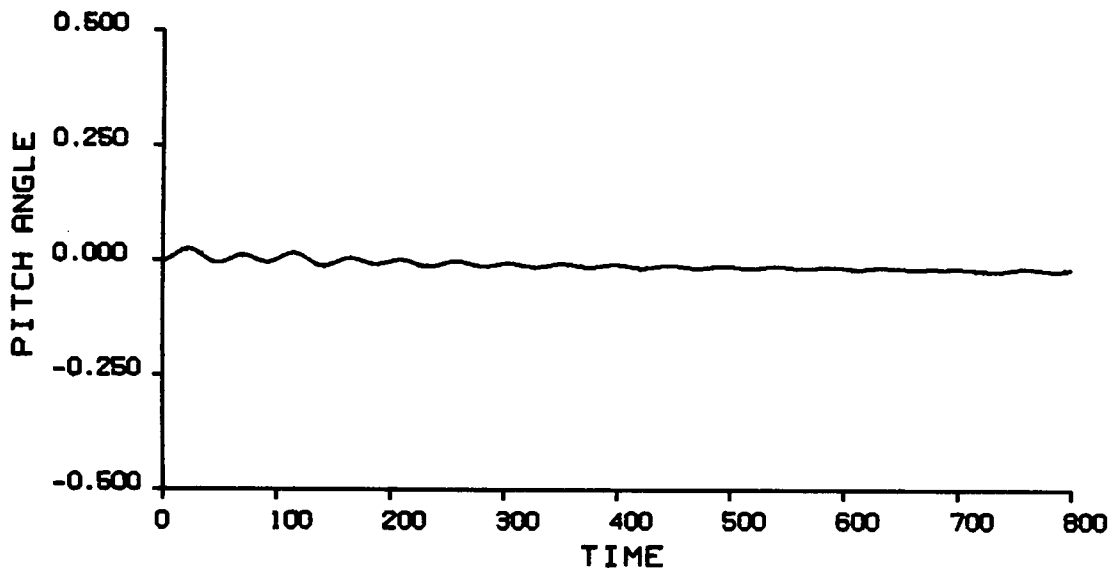

(b)

Figure 4.2. Numerical results for two degrees of freedom in roll and pitch, $\alpha = 15°$, $\xi(0) = 5°$, $\dot{\xi}(0) = 0$:
(a) Roll angle as a function of time.
(b) Pitch angle as a function of time.

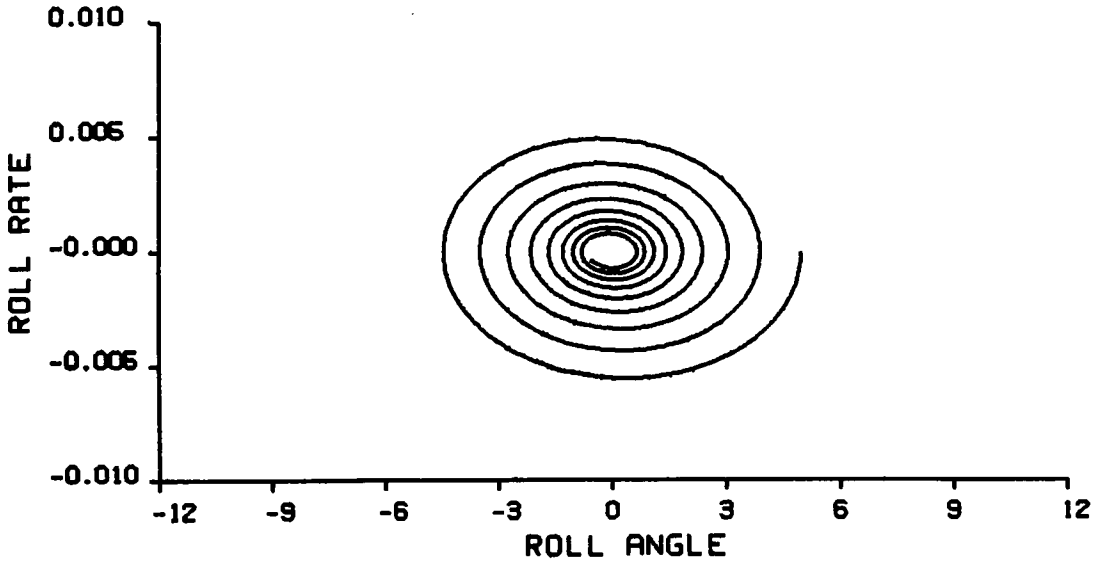

(c)

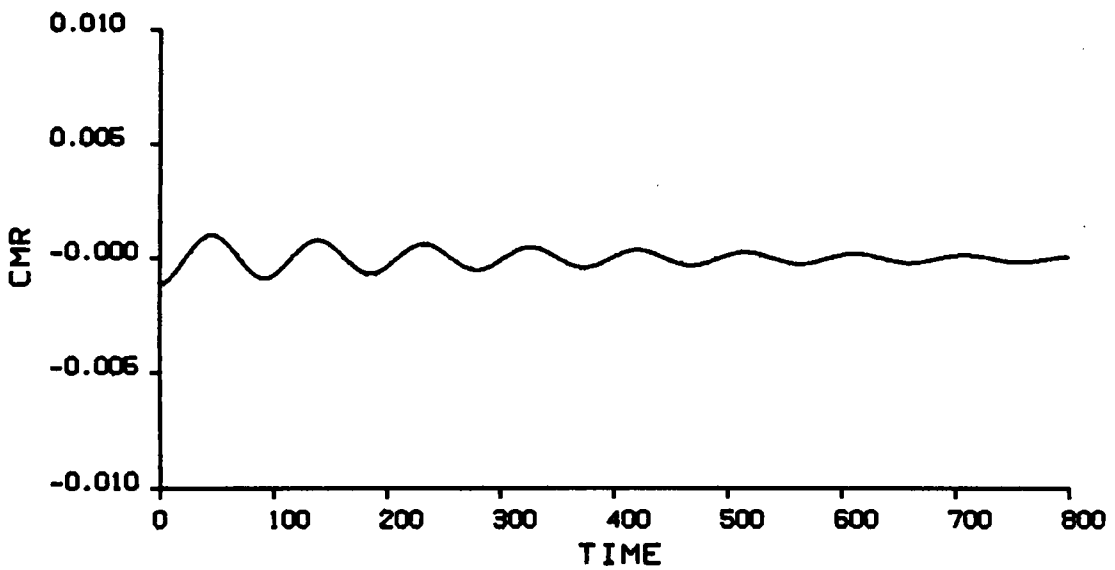

(d)

Figure 4.2. (c) Phase plane.
(d) Roll-moment coefficient as a function of time.

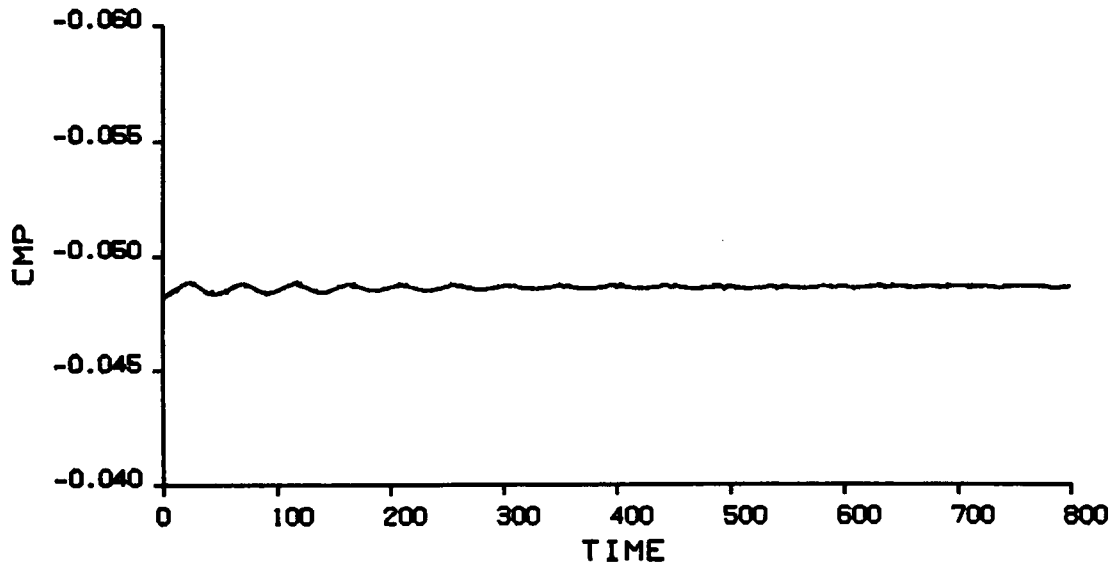

(e)

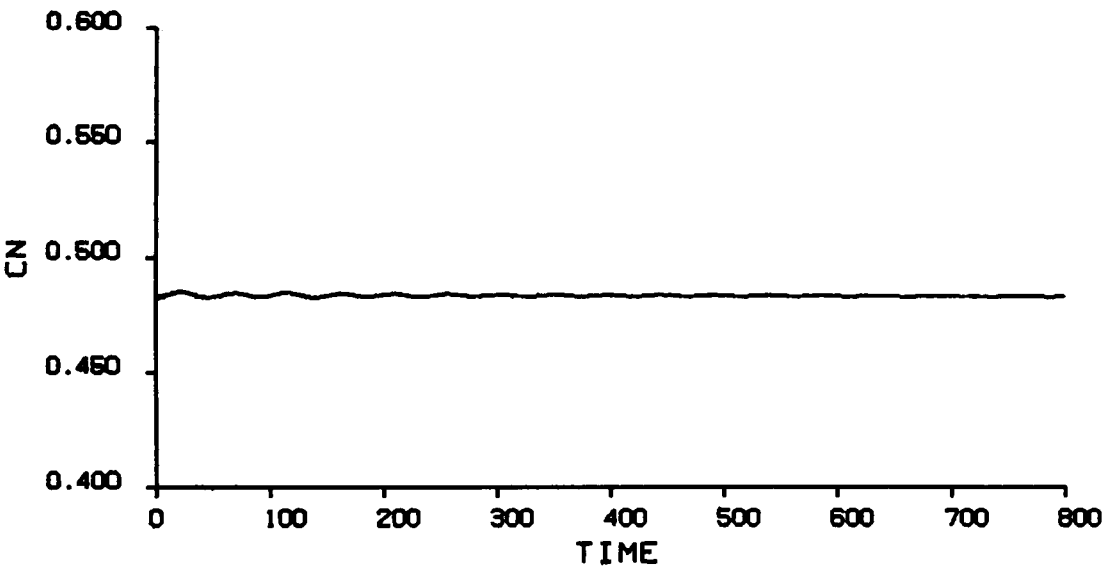

(f)

Figure 4.2. (e) Pitch-moment coefficient as a function of time.
(f) Normal-force coefficient as a function of time.

It is interesting to note that the predicted roll moment and roll angle have the same frequency, but are not in phase for both one and two degrees of freedom. The phase changes with angle of attack and eventually leads to negative damping and self-excited motions.

4.4.2 α = 20 Degrees

Here we choose the freestream speed to be

$$U_\infty = 18.3 \text{ m/s} \tag{4.13}$$

and the damping coefficients to be

$$\mu_x = 0.378\text{x}10^{-4}, \quad \mu_y = \mu_z = 0 \tag{4.14}$$

The coefficients become

$$C_1 = 0.354 \tag{4.15a}$$

$$C_2 = 0.818\text{x}10^{-3} \tag{4.15b}$$

$$C_3 = 0.0215 \tag{4.15c}$$

$$C_4 = 0. \tag{4.15d}$$

$$C_5 = 0.158\text{x}10^{-2} \tag{4.15e}$$

The results for one degree of freedom in roll are shown in Figure 4.3. In part a, the roll angle is given as a function of time; the phase plane is given in part b. These results show the initial disturbance (ξ = 5 degrees and $\dot{\xi}$ = 0 at t = 0) leads to a slowly growing motion, indicating that this is an unstable angle of attack.

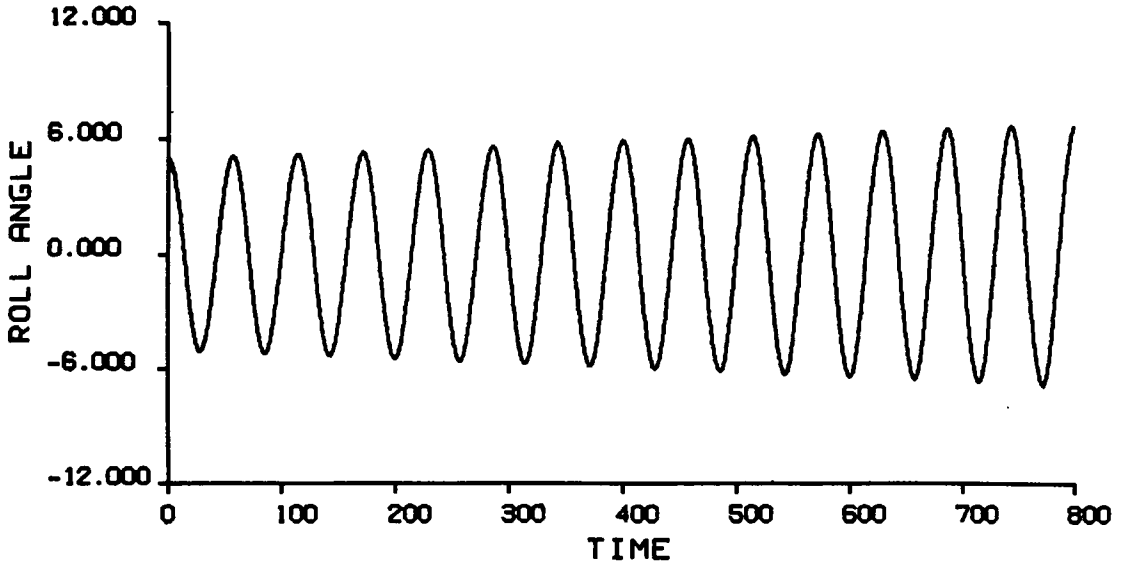

(a)

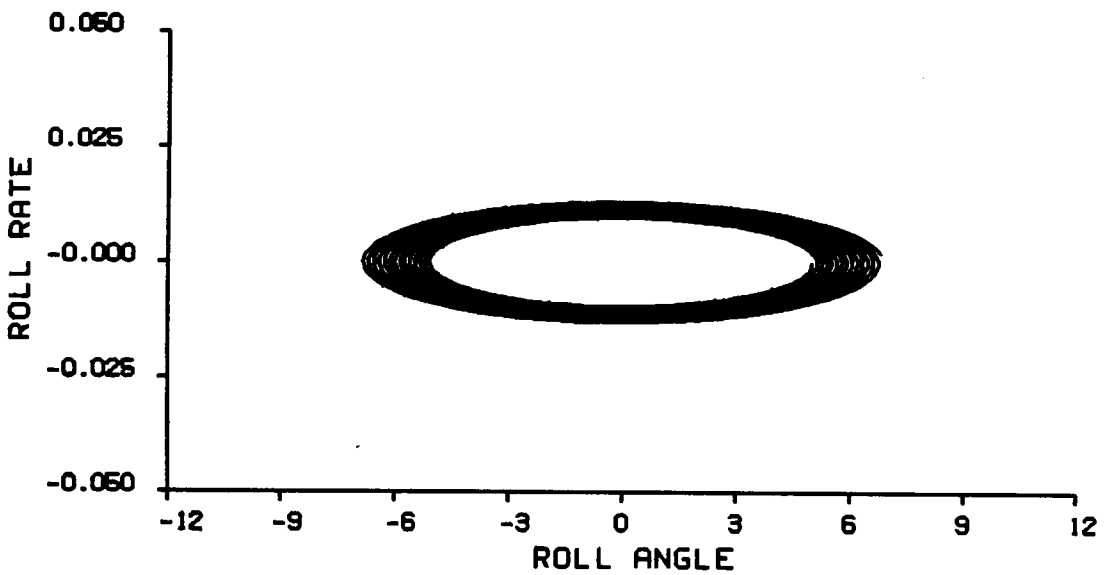

(b)

Figure 4.3. Numerical results for one degree of freedom in roll, $\alpha = 20°$, $\xi(0) = 5°$, $\dot{\xi}(0) = 0$:
(a) Roll angle as a function of time.
(b) Phase plane.

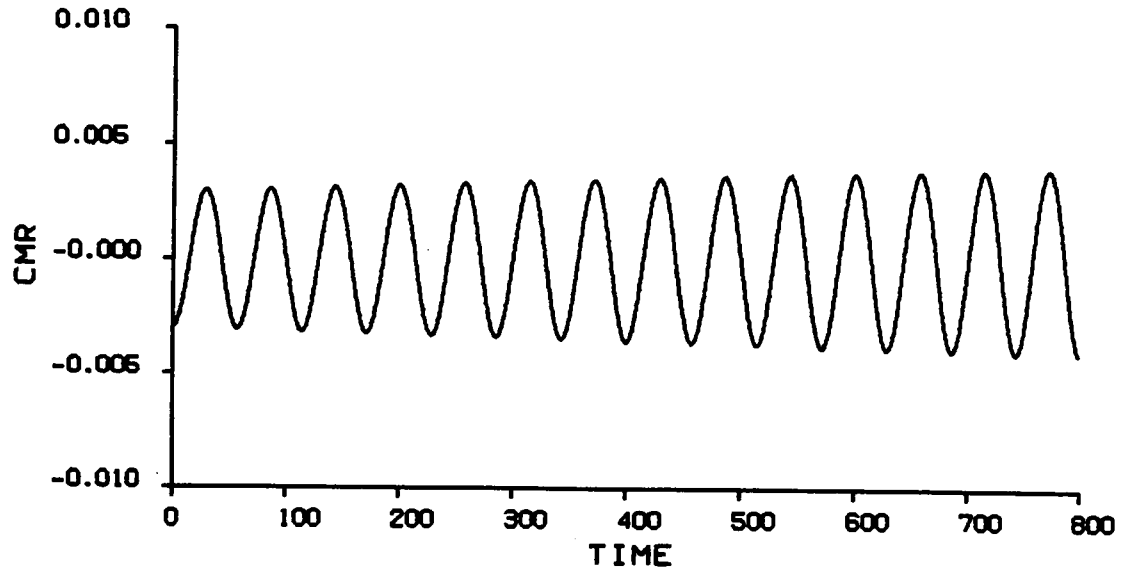

(c)

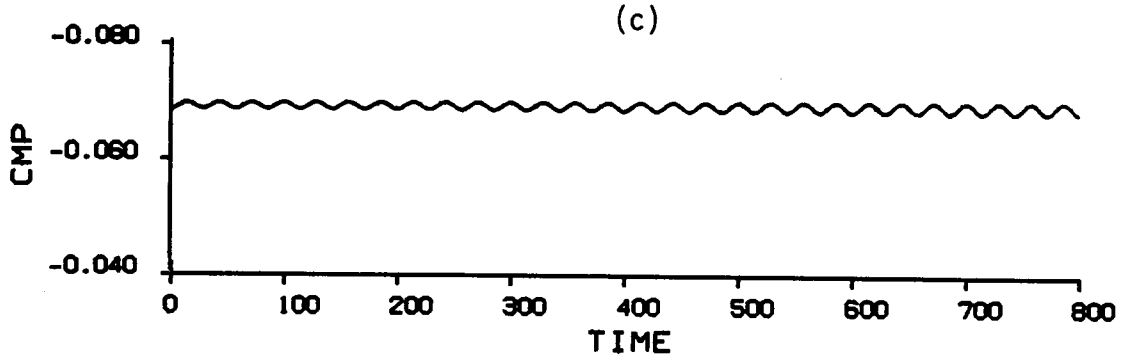

(d)

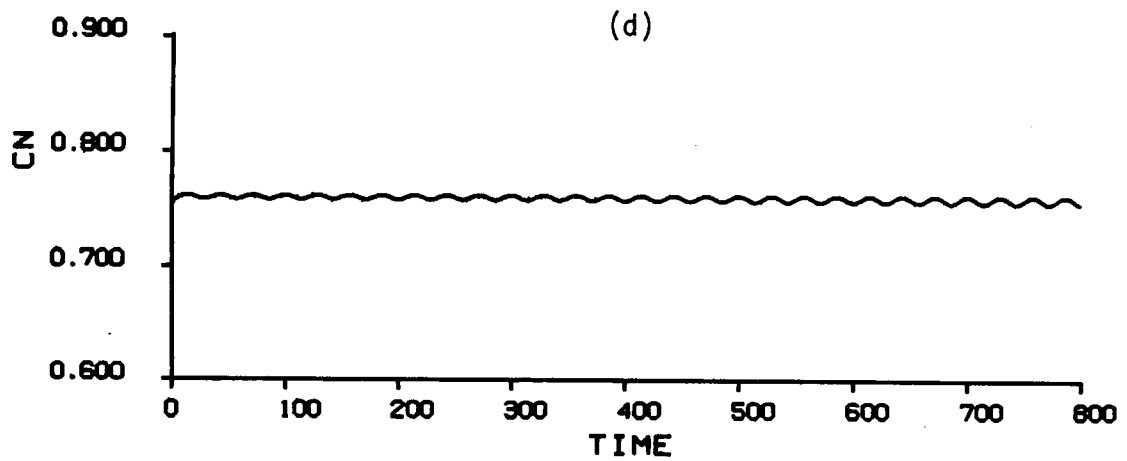

(e)

Figure 4.3. (c) Roll-moment coefficient as a function of time.
(d) Pitch-moment coefficient as a function of time.
(e) Normal-force coefficient as a function of time.

The roll-moment, pitch-moment, and normal-force coefficients are given as functions of time in parts c, d, and e, respectively.

The results for two degrees of freedom (roll and pitch) are given in Figure 4.4 where the initial disturbance is $\xi = 5$ degrees and $\dot{\xi} = 0$ at $t = 0$. In this case, the pitching motion is very small after a few hundred time steps, while the rolling motions appear to be approaching the same limit cycle as in the one-degree-of-freedom case.

As in the case of 15 degrees angle of attack, the additional degree of freedom in pitch does not appear to have any significant effect on the motion. Comparison of Figures 4.3 and 4.4 show the rolling motion, moments, and forces have the same period, and presumably all will eventually arrive at the same limit cycle.

4.4.3 α = 22.5 Degrees

Here we choose the freestream speed to be

$$U_\infty = 17.2 \text{ m/s} \tag{4.16}$$

and the damping coefficient to be

$$\mu_x = 0.378\text{x}10^{-4}, \quad \mu_y = \mu_z = 0 \tag{4.17}$$

The coefficient become

$$C_1 = 0.354 \tag{4.18a}$$

$$C_2 = 0.872\text{x}10^{-3} \tag{4.18b}$$

$$C_3 = 0.0215 \tag{4.18c}$$

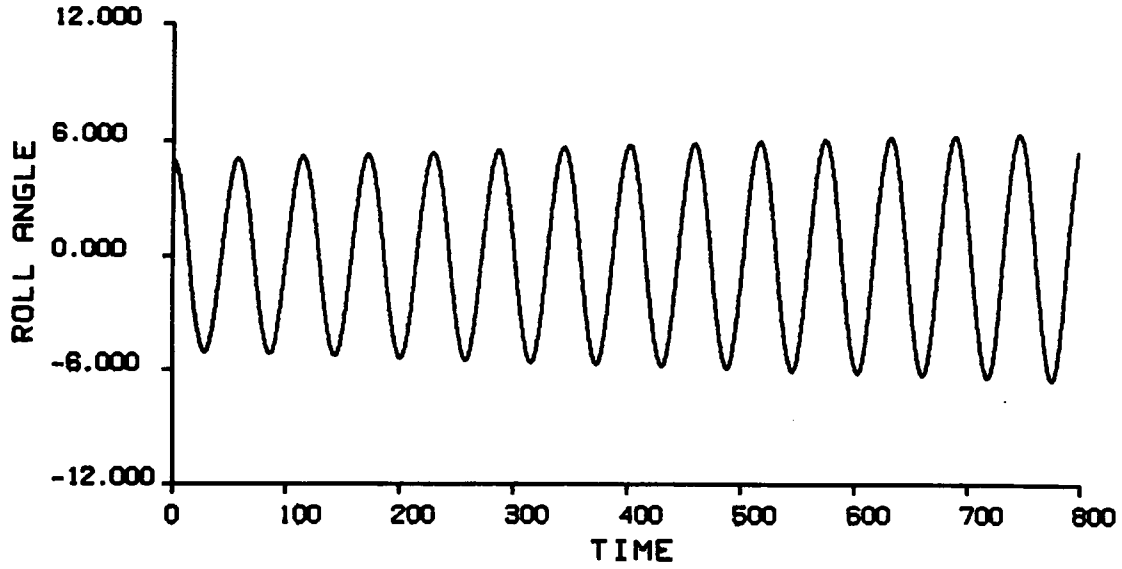

(a)

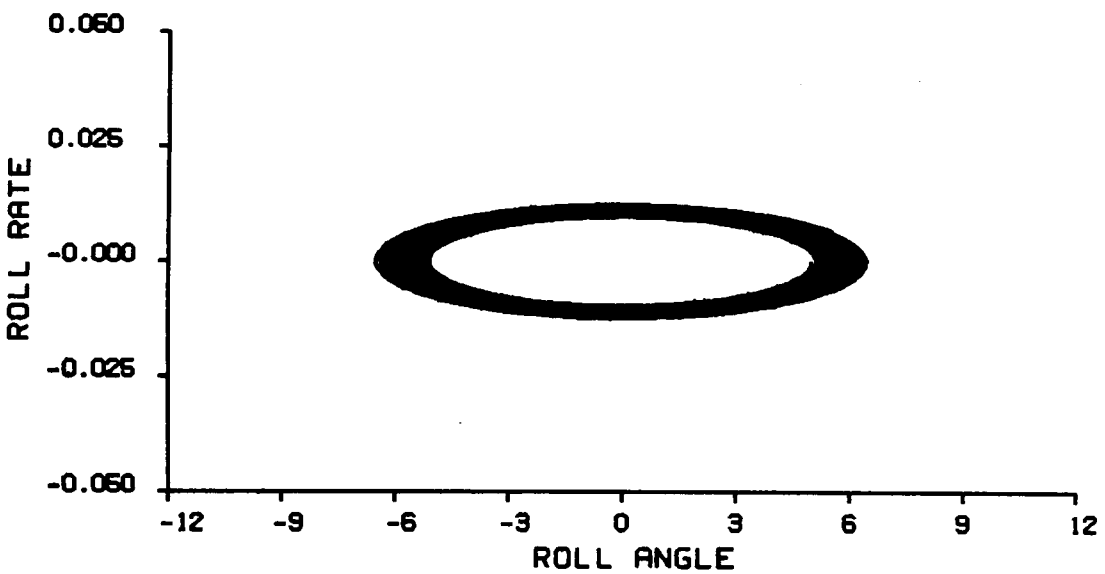

(b)

Figure 4.4. Numerical results for two degrees of freedom in roll and pitch, $\alpha = 20°$, $\xi(0) = 5°$, $\dot{\xi}(0) = 0$:
(a) Roll angle as a function of time.
(b) Phase plane.

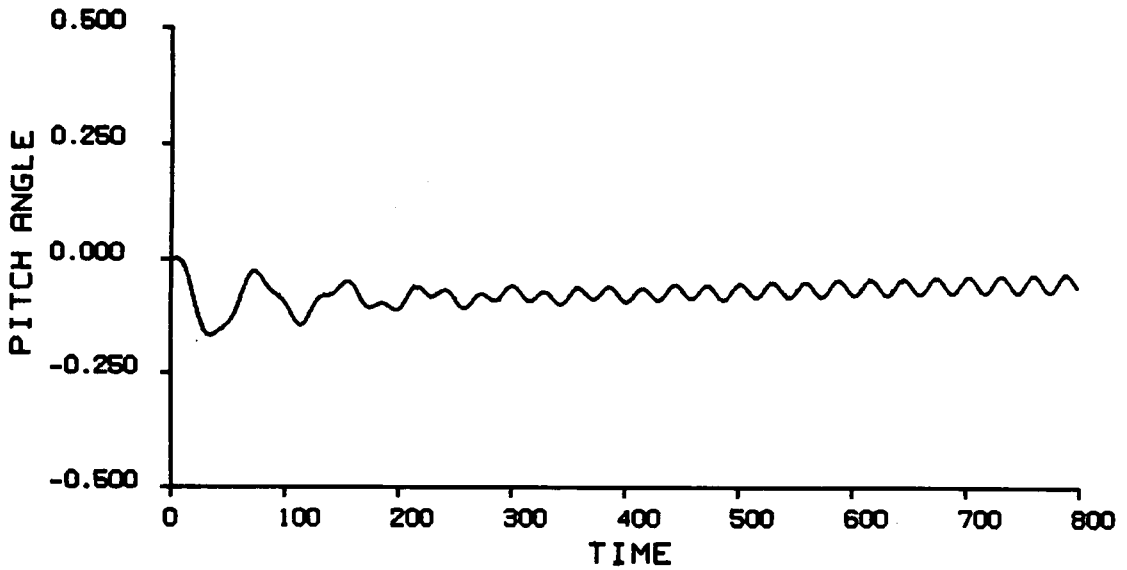

(c)

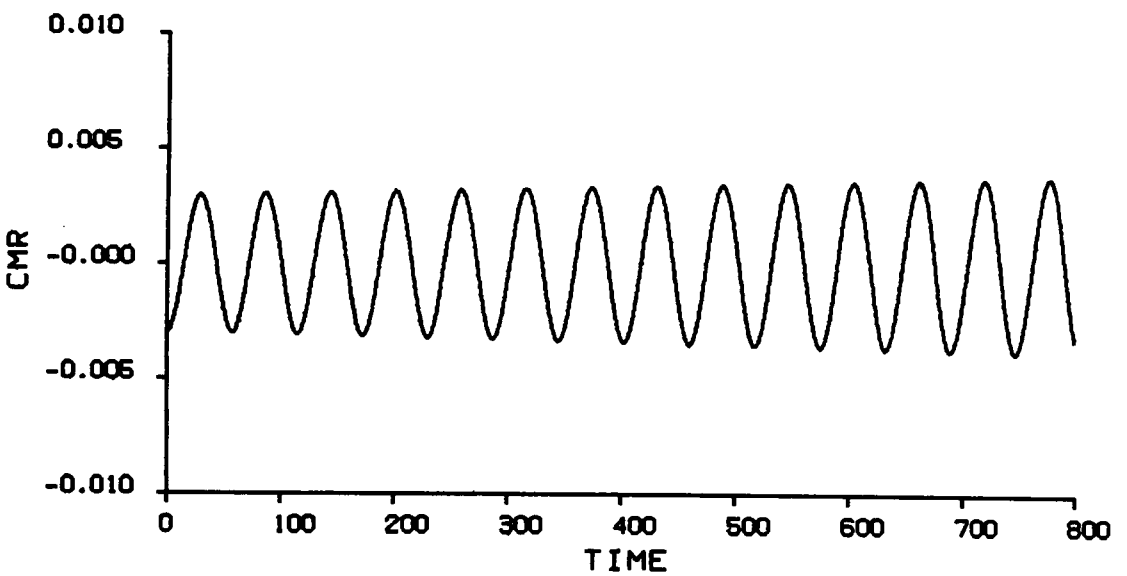

(d)

Figure 4.4. (c) Pitch angle as a function of time.
(d) Roll-moment coefficient as a function of time.

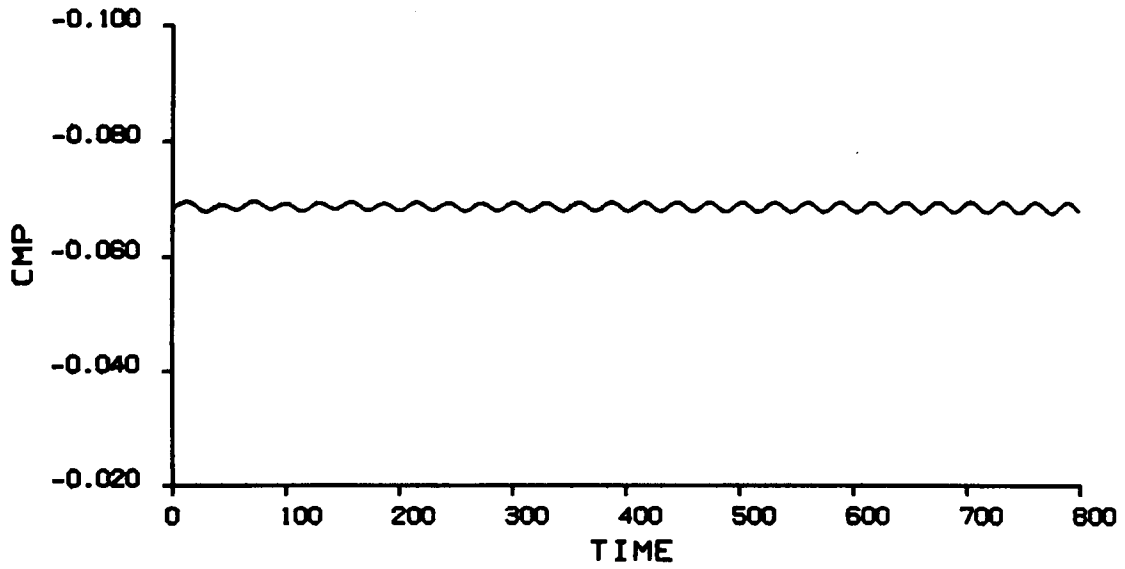

(e)

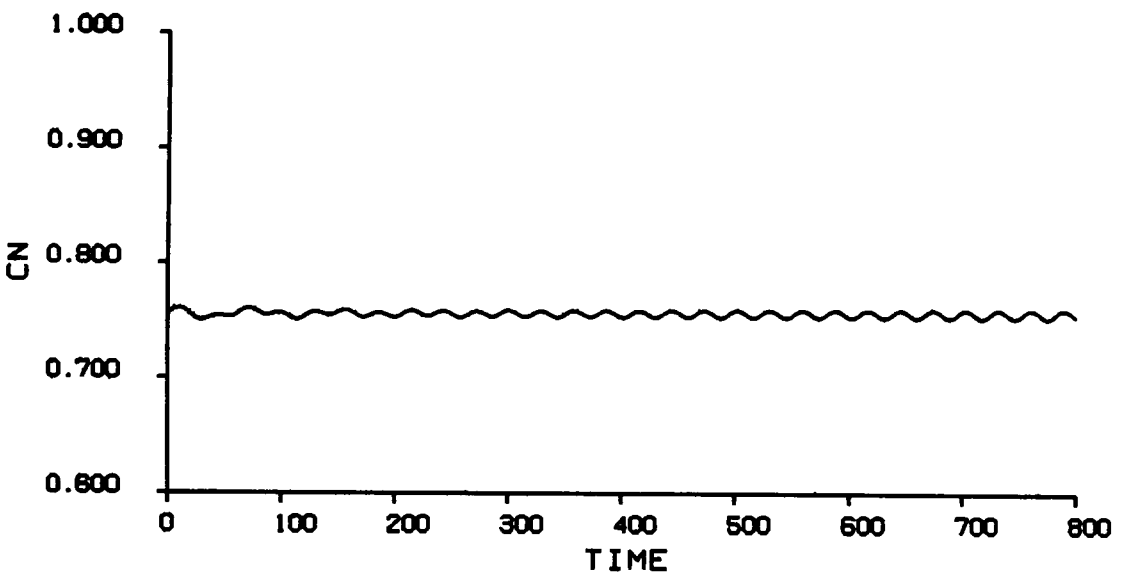

(f)

Figure 4.4. (e) Pitch-moment coefficient as a function of time.
(f) Normal-force coefficient as a function of time.

$$C_4 = 0.0 \tag{4.18d}$$

$$C_5 = 0.179 \times 10^{-2} \tag{4.18e}$$

The results for one degree of freedom in roll are given in Figure 4.5. Clearly, the motion rapidly approaches a limit cycle as indicated in part a, where the roll angle is shown as a function of time, and in part b, where the phase plane is shown. The roll-moment, pitch-moment, and normal-force coefficients are given as functions of time in parts c, d, and e, respectively. Again the roll angle and roll moment have the same period, but are not in phase. The pitch-moment and normal-force coefficients have half the period of the roll angle and roll-moment coefficient. Moreover, the mean pitch-moment coefficient significantly increases toward zero, while the mean normal-force coefficient correspondingly decreases. These results suggest that for two degrees of freedom the wing may pitch up while oscillating in roll.

The results for two degrees of freedom (roll and pitch) are shown in Figure 4.6. The motion appears to be approaching a limit cycle, as in the case of one degree of freedom. But here both the amplitude and period are less than in the case of one degree of freedom. In part c, the deviation in the pitch angle from the equilibrium position is given as a function of time. The mean pitch angle increases by approximately one degree. The roll-moment, pitch-moment, and normal-force coefficients are shown in parts d, e, and f, respectively.

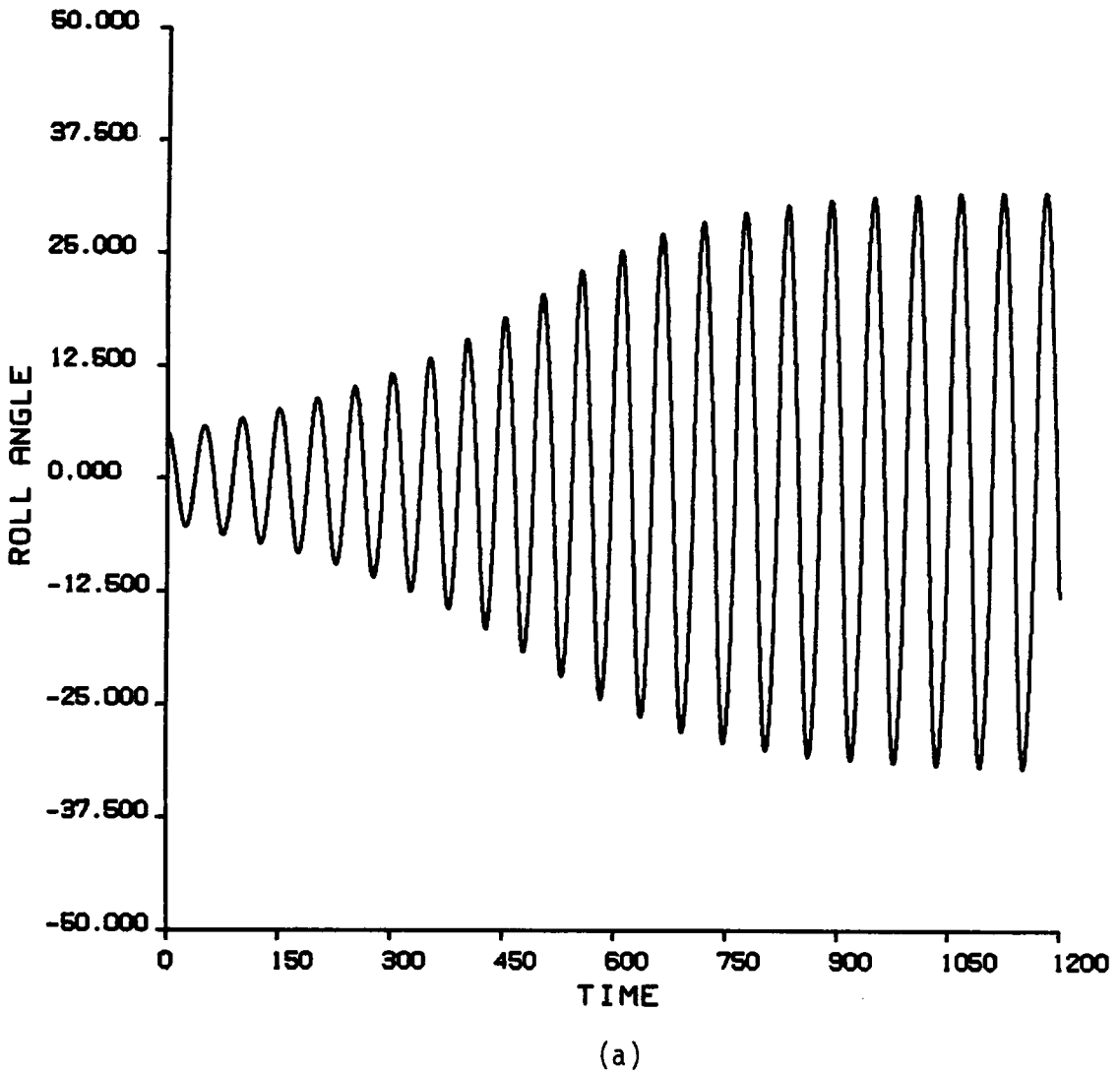

(a)

Figure 4.5. Numerical results for one degree of freedom in roll, $\alpha = 22.5°$, $\xi(0) = 5°$, $\dot{\xi}(0) = 0$:
(a) Roll angle as a function of time.

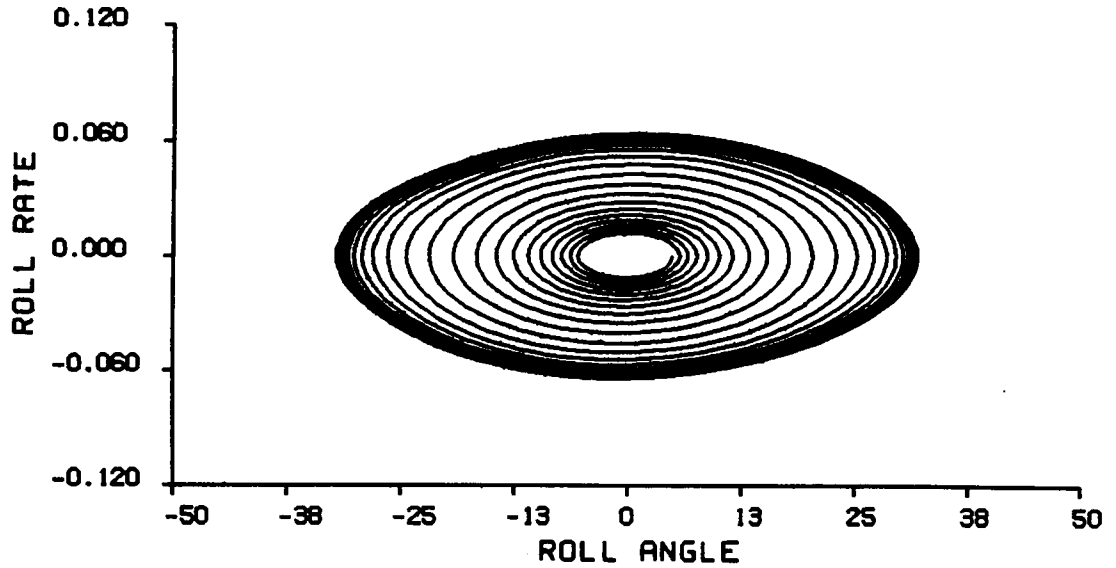

(b)

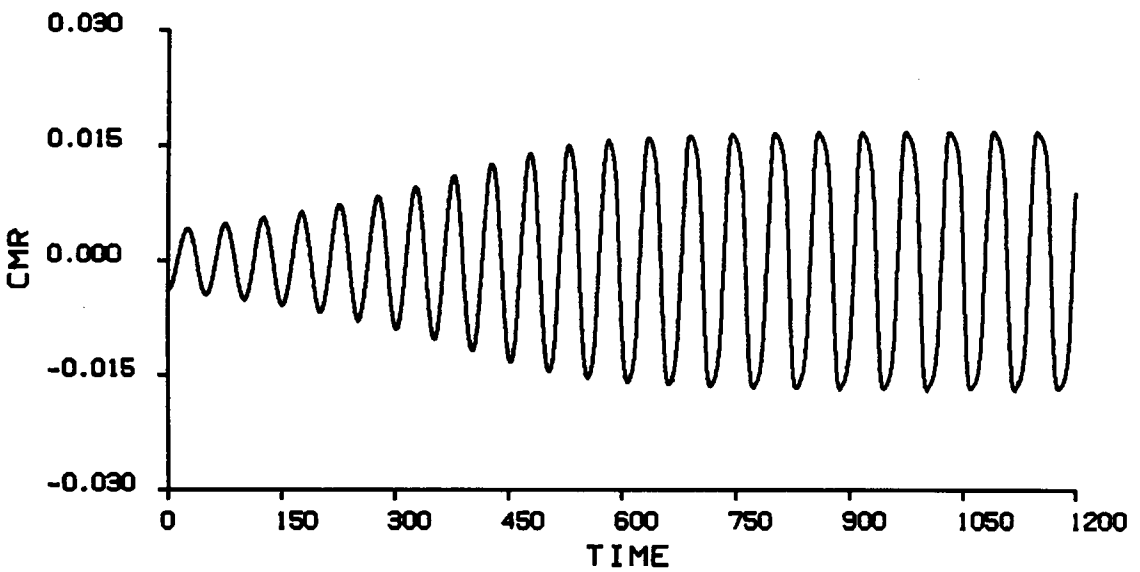

(c)

Figure 4.5. (b) Phase plane.
(c) Roll-moment coefficient as a function of time.

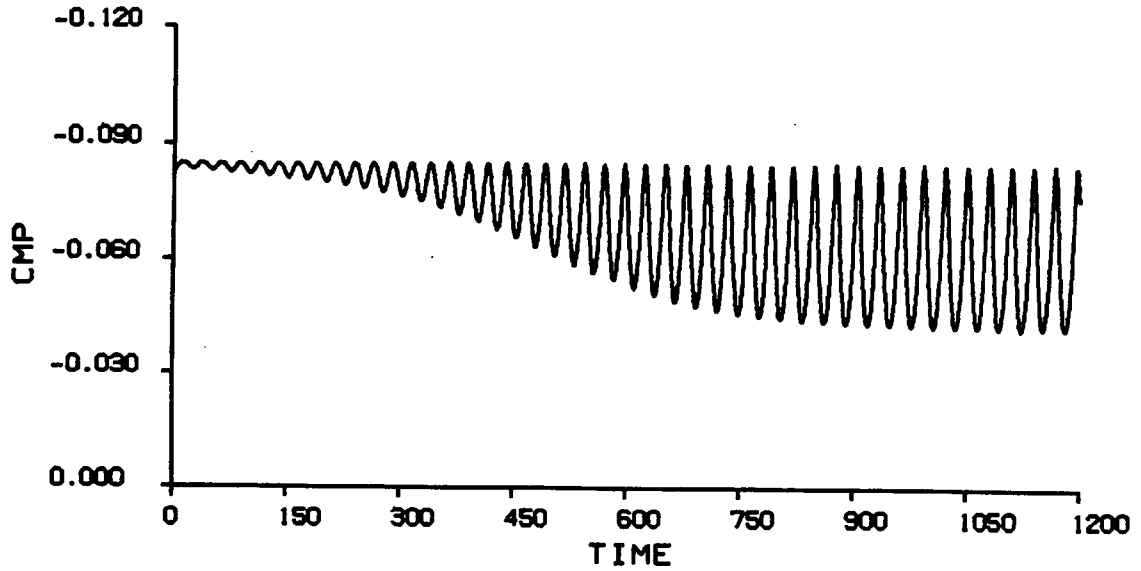

(d)

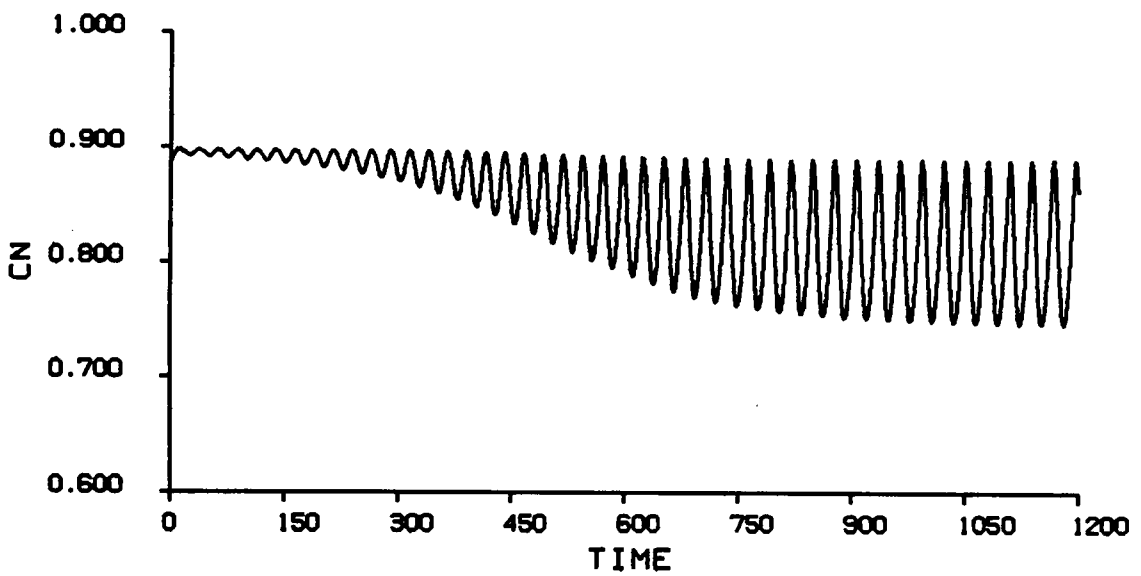

(e)

Figure 4.5. (d) Pitch-moment coefficient as a function of time.
(e) Normal-force coefficient as a function of time.

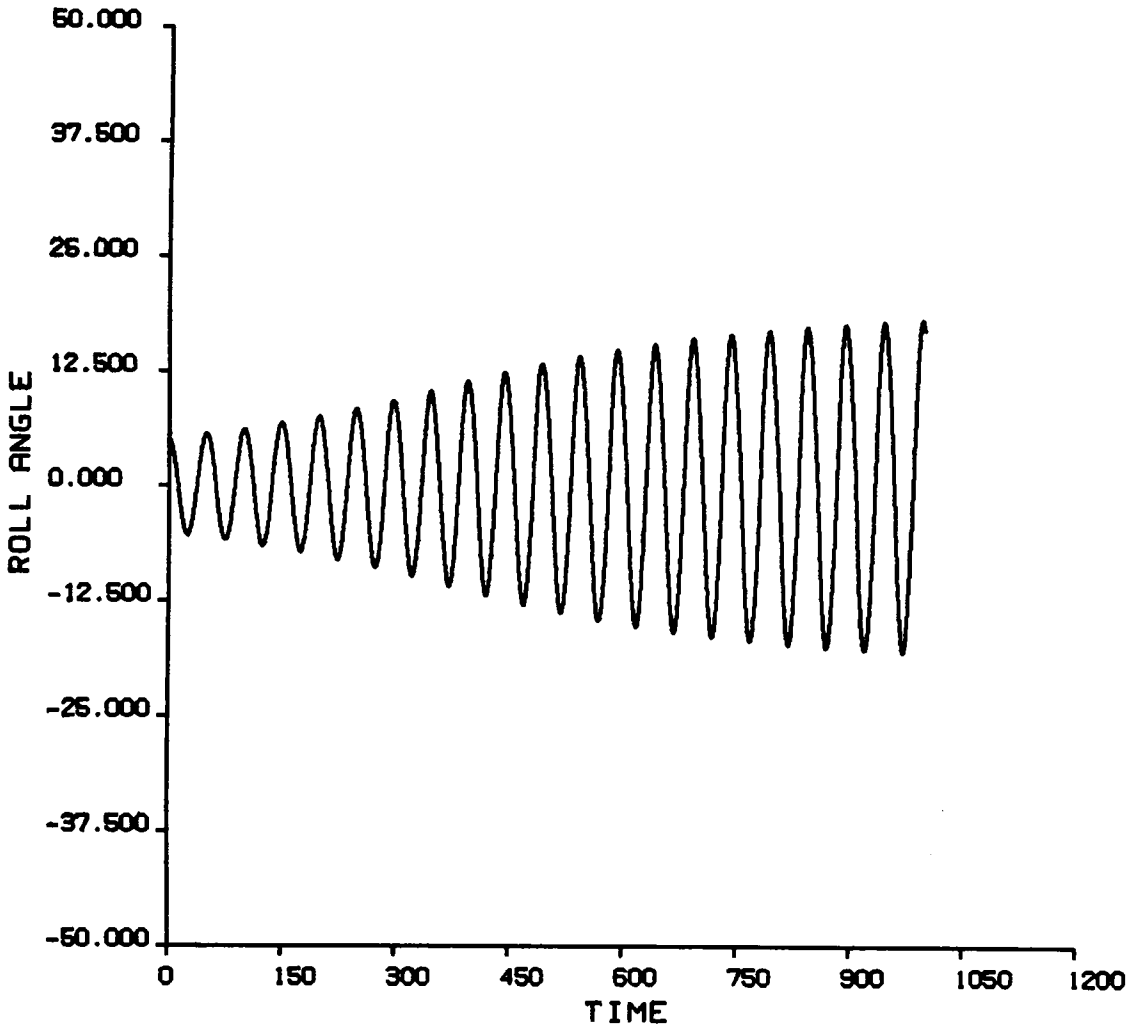

(a)

Figure 4.6. Numerical results for two degrees of freedom in roll and pitch, $\alpha = 22.5°$, $\xi(0) = 5°$, $\dot{\xi}(0) = 0$:
(a) Roll angle as a function of time.

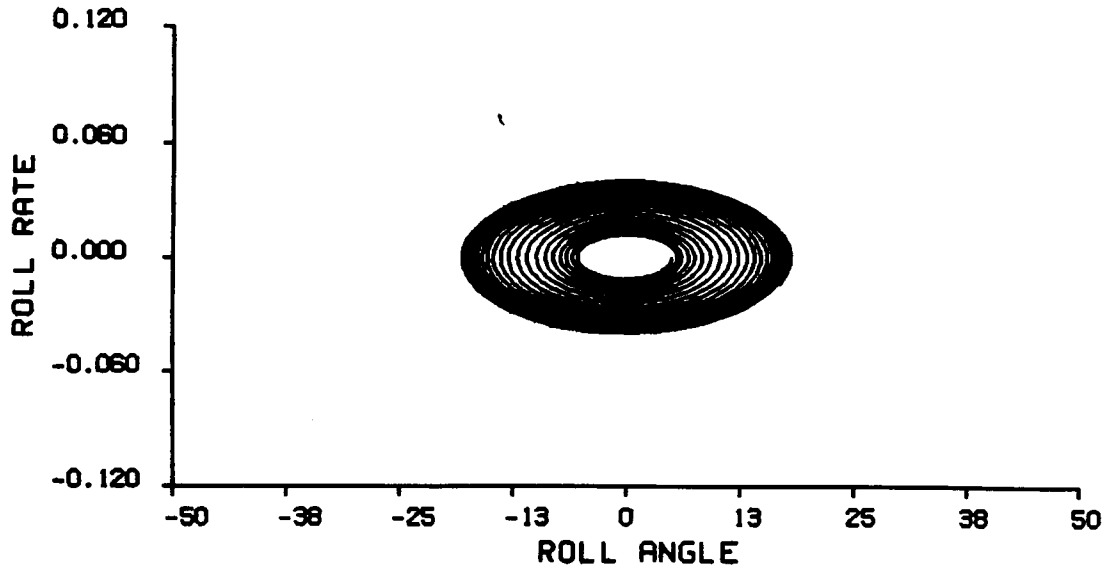

(b)

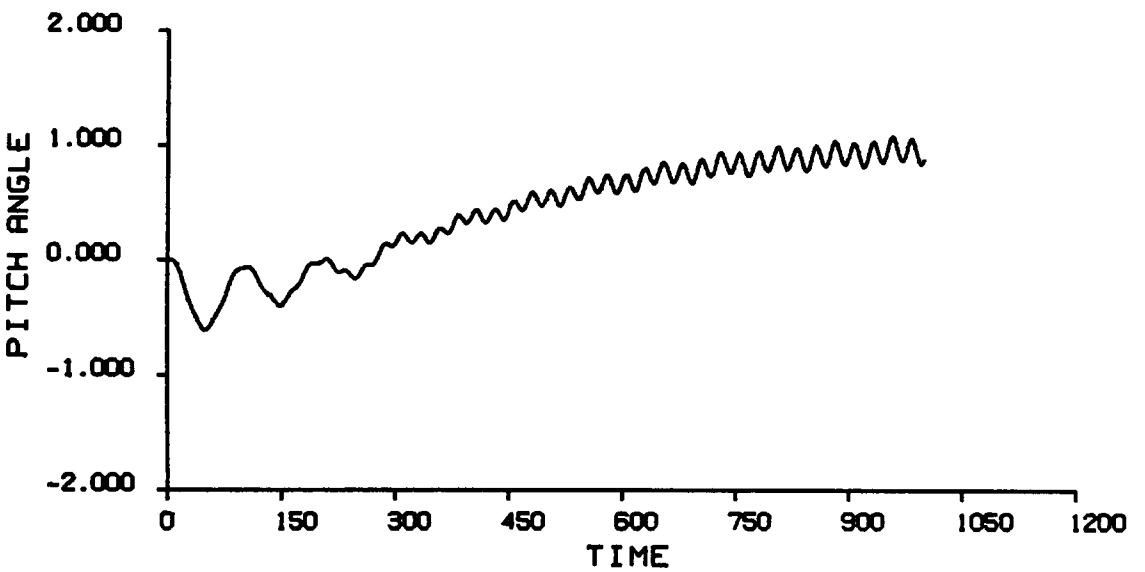

(c)

Figure 4.6. (b) Phase plane.
(c) Pitch angle as a function of time.

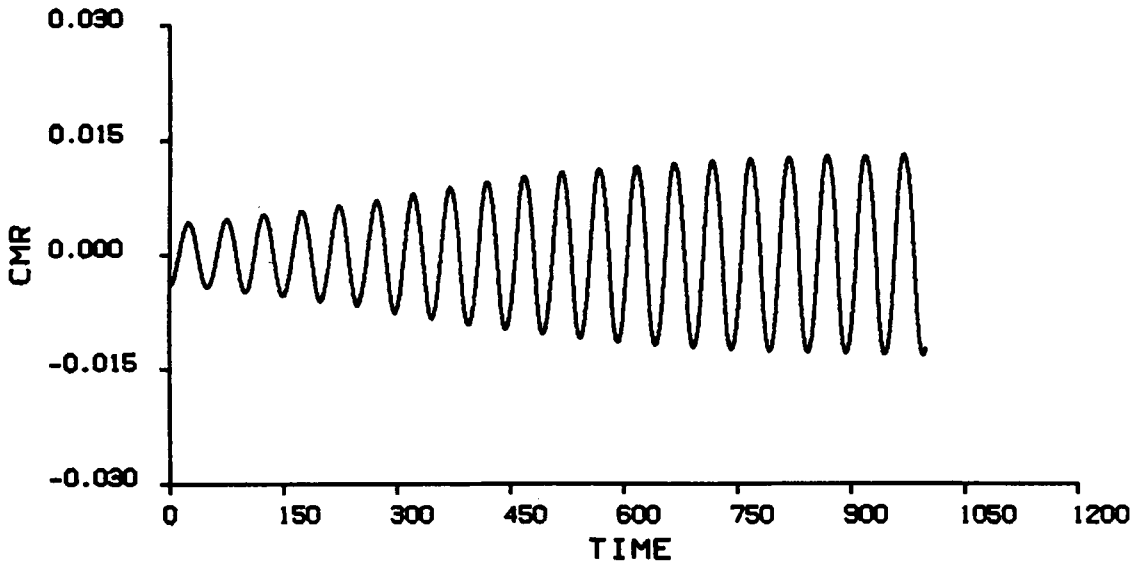

(d)

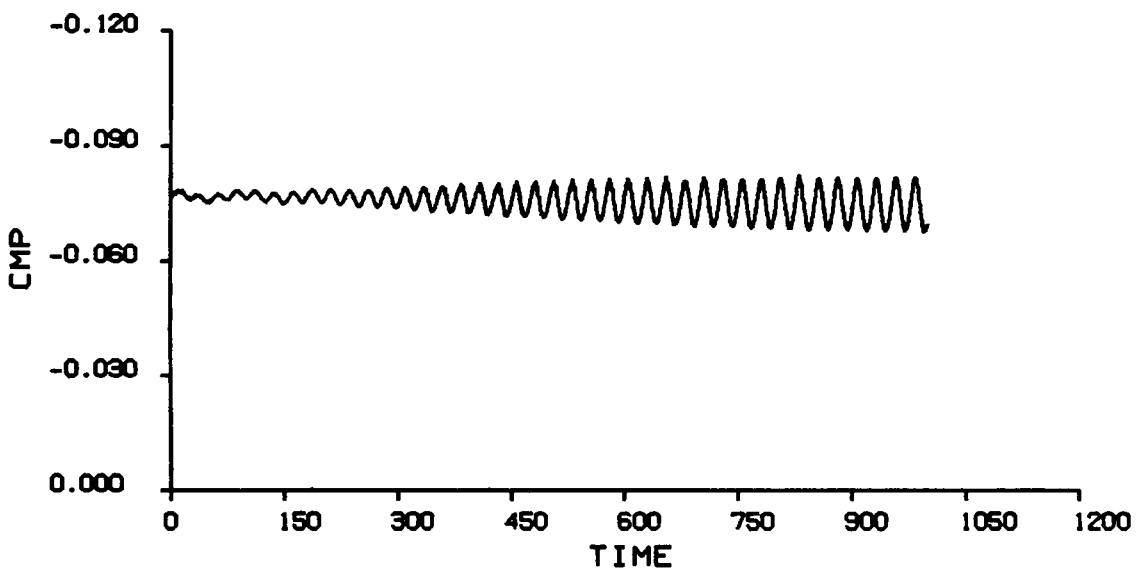

(e)

Figure 4.6. (d) Roll-moment coefficient as a function of time.
(e) Pitch-moment coefficient as a function of time.

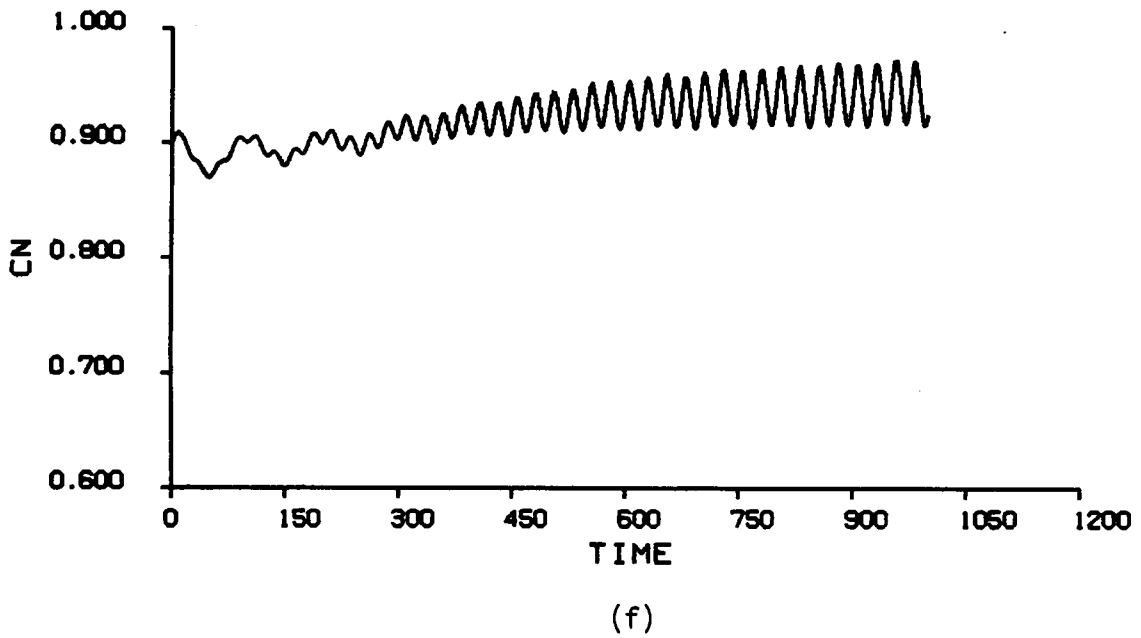

(f)

Figure 4.6. (f) Normal-force coefficient as a function of time.

4.4.4 α = 25 Degrees

Here we choose the freestream speed to be

$$U_\infty = 16.1 \text{ m/s} \tag{4.19}$$

and the damping coefficients to be

$$\mu_x = 0.378\text{x}10^{-4}, \quad \mu_y = \mu_z = 0 \tag{4.20}$$

The coefficients become

$$C_1 = 0.354 \tag{4.21a}$$

$$C_2 = 0.933\text{x}10^{-3} \tag{4.21b}$$

$$C_3 = 0.0215 \tag{4.21c}$$

$$C_4 = 0. \tag{4.21d}$$

$$C_5 = 0.206\text{x}10^{-2} \tag{4.21e}$$

The results for one degree of freedom in roll are given in Figure 4.7. Clearly, the motion reaches a limit cycle as shown in parts a and b. A comparison of parts a and b of Figures 4.3, 4.5 and 4.7 shows that the limit cycle is reached more quickly at high angles of attack. The amplitude of the limit-cycle motion is about 33 degrees and the period is approximately 0.4 seconds. Both agree closely with the observations of Levin and Katz (1982). Table 4.1 shows how the variations in C_2 values affect the amplitude and the period of the limit-cycle motion. The roll-moment, pitch-moment, and normal-force coefficients are, respectively, given as function of the time in parts c, d, and e of Figure 4.7. The mean values of both the pitch moment and the normal

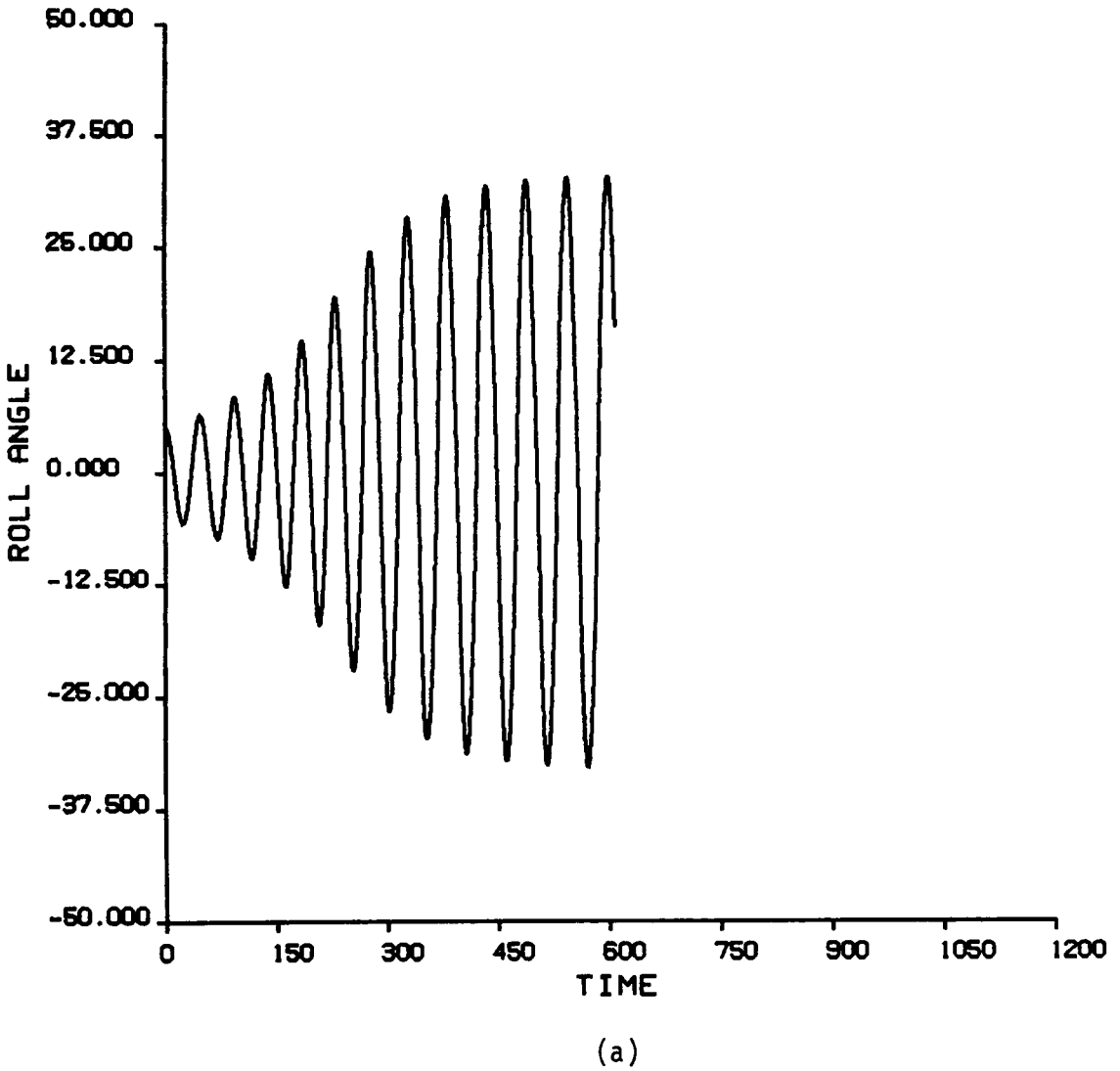

(a)

Figure 4.7. Numerical results for one degree of freedom in roll, $\alpha = 25°$, $\xi(0) = 5°$, $\dot{\xi}(0) = 0$:
(a) Roll angle as a function of time.

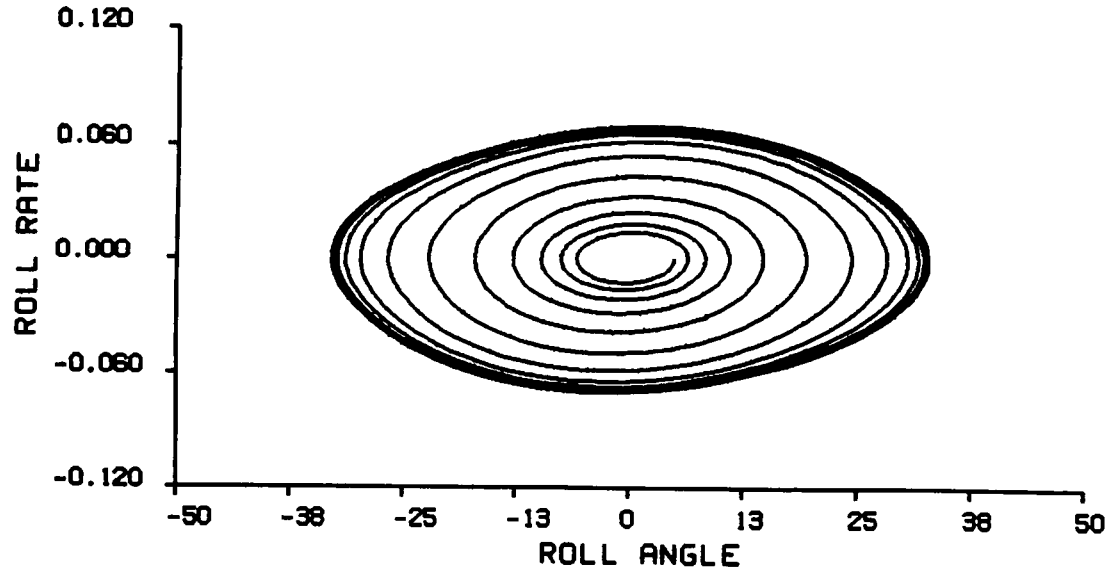

(b)

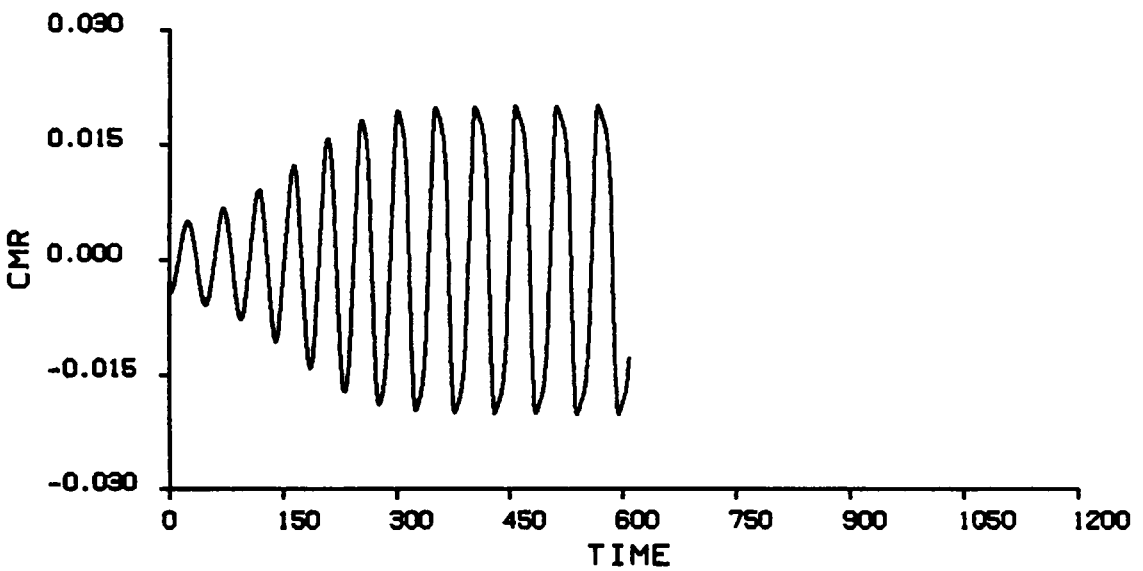

(c)

Figure 4.7. (b) Phase plane.
(c) Roll-moment coefficient as a function of time.

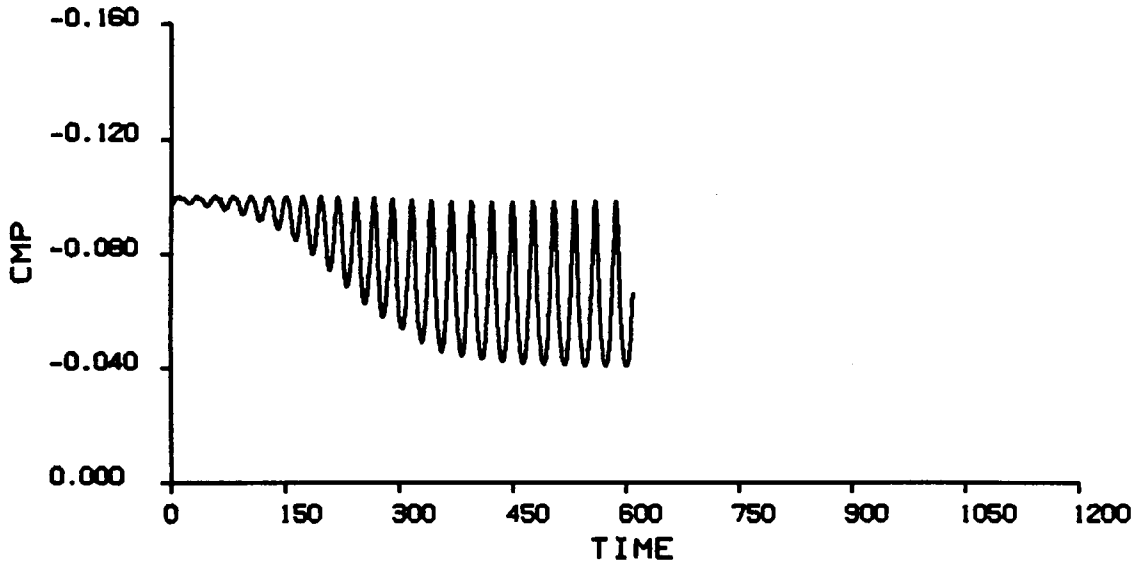

(d)

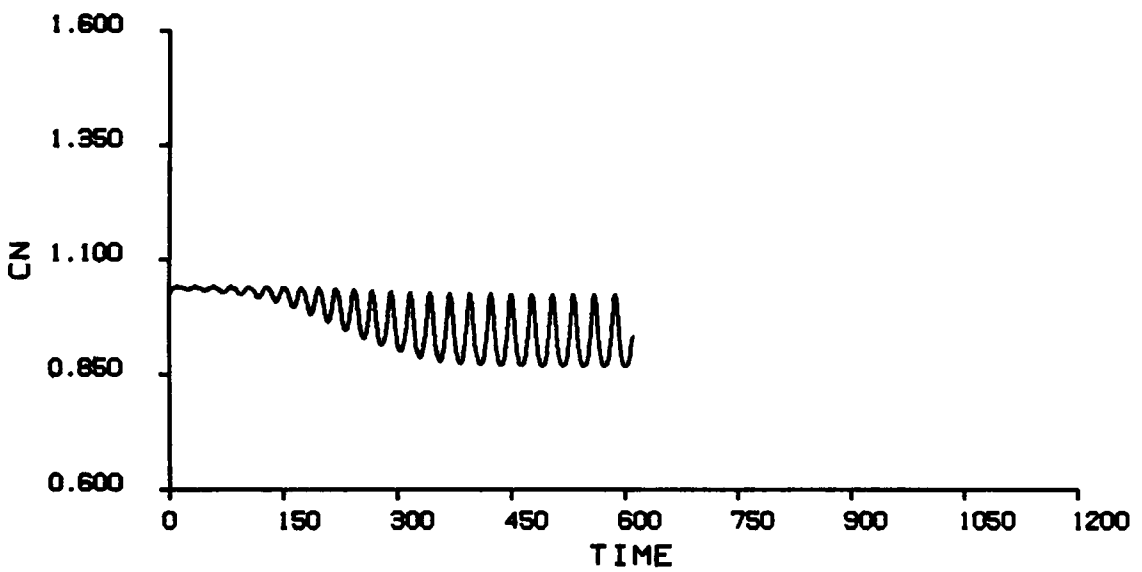

(e)

Figure 4.7. (d) Pitch-moment coefficient as a function of time.
(e) Normal-force coefficient as a function of time.

Table 4.1 The amplitude and the period of the limit-cycle motion as functions of C_2 (for α = 25 degrees; in roll only).

C_2	Amplitude (degrees)	Period (sec)
0.008	23.7	0.350
0.004	28.4	0.370
0.002	31.2	0.385
0.001	32.9	0.393
Levin & Katz (1982)	33	0.40

force are less than those for the static case. This suggests that for the two-degree-of-freedom the wing will pitch up.

The results for one degree of freedom in pitch are shown in Figure 4.8. These results are typical of all angles of attack. The motion rapidly decays to the static equilibrium position. Part a gives the deviation of the pitch angle from the equilibrium position as a function of time, and part b gives the corresponding phase-plane portrait. The roll-moment, pitch-moment, and normal-force coefficients are given as functions of time in parts c, d, and e, respectively.

The results for two degrees of freedom (roll and pitch) are given in Figure 4.9. In part a the roll angle is shown as a function of time, and in part b the corresponding phase plane is shown. Part c gives the pitch angle as function of time. The motion is growing slowly compared with the motion in Figure 4.7. A limit cycle has not developed in Figure 4.9, but after 600 time steps the amplitude of the roll motion for two degrees of freedom is only about one third of the amplitude for one degree of freedom. The period in roll is slightly less than that for one degree of freedom. Moreover, the period in pitch is slightly less than twice the period in roll. This suggests, as does the obvious change in amplitude, that transient solutions are still present in the response. The deviation in pitch angle appears to oscillate around zero. Here the amplitude of the pitching motion is much larger than that shown in Figure 4.6c. The roll motion appears to loose energy to the pitch motion. The roll-moment, pitch-moment, and normal-force coefficients are given as functions of time in parts d, e and f,

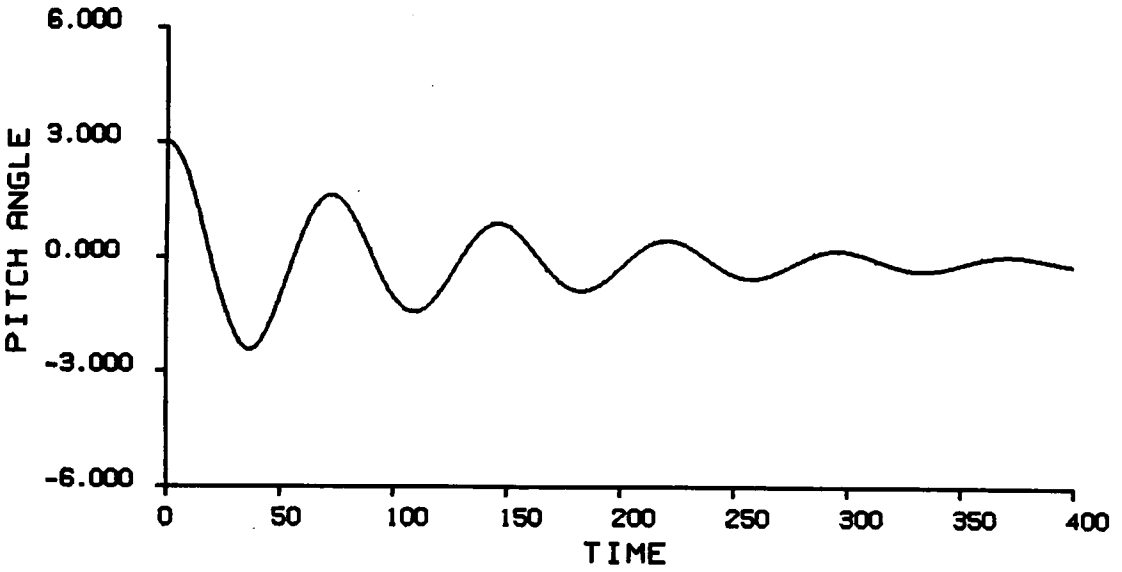

(a)

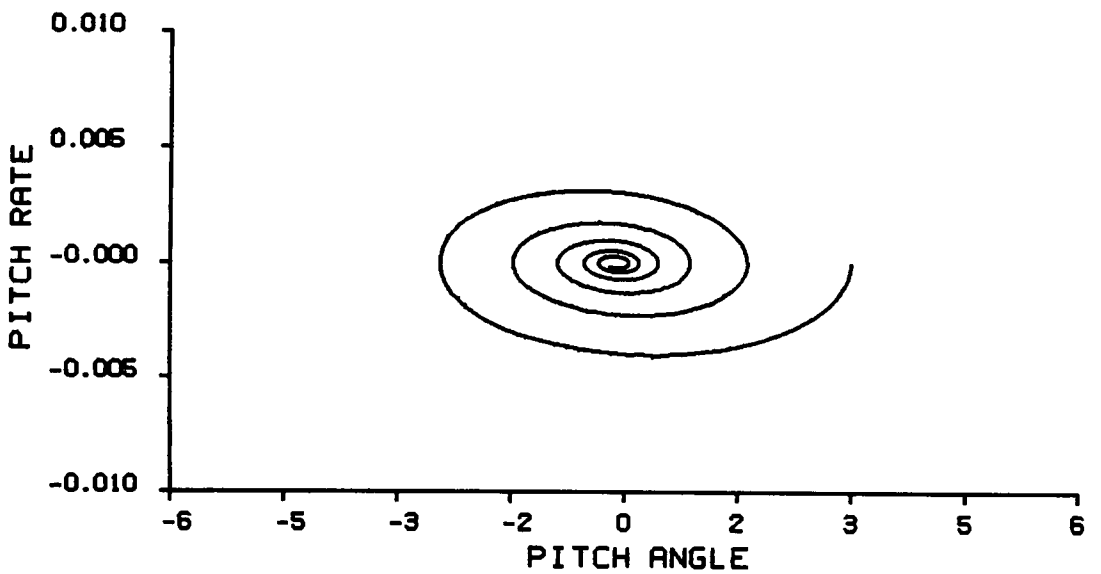

(b)

Figure 4.8. Numerical results for one degree of freedom in pitch, $\alpha = 25°$, $\theta(0) = 3°$, $\dot{\theta}(0) = 0$:
(a) Pitch angle as function of time.
(b) Phase plane.

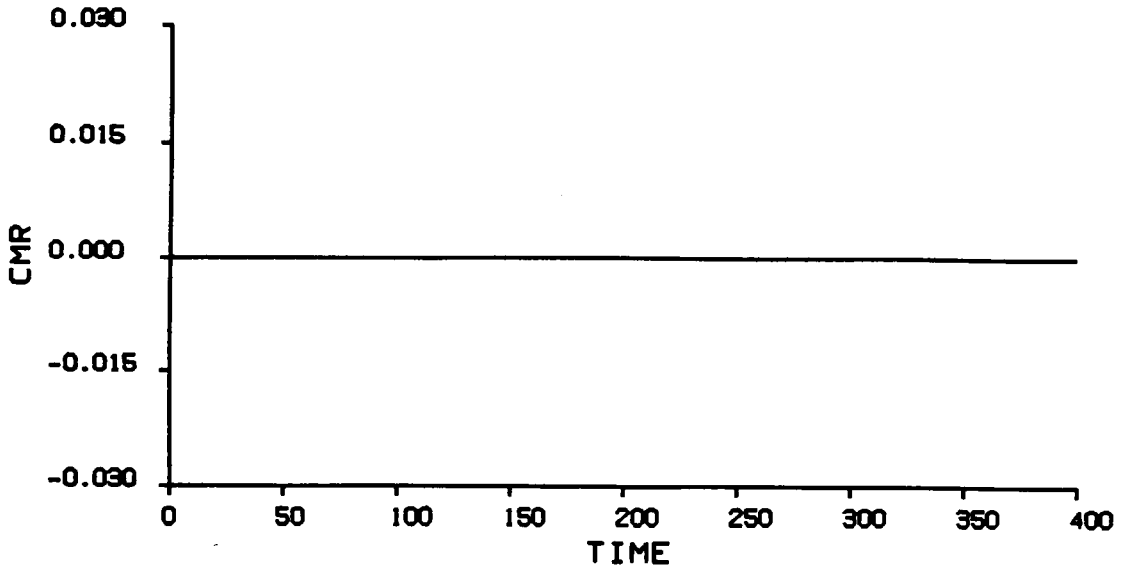

(c)

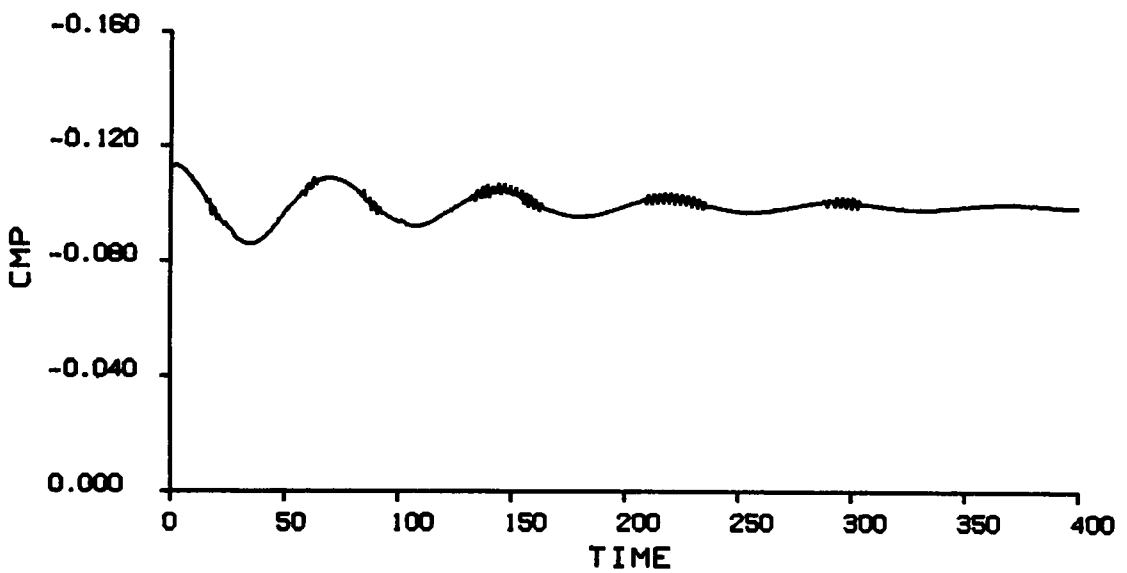

(d)

Figure 4.8. (c) Roll-moment coefficient as a function of time.
(d) Pitch-moment coefficient as a function of time.

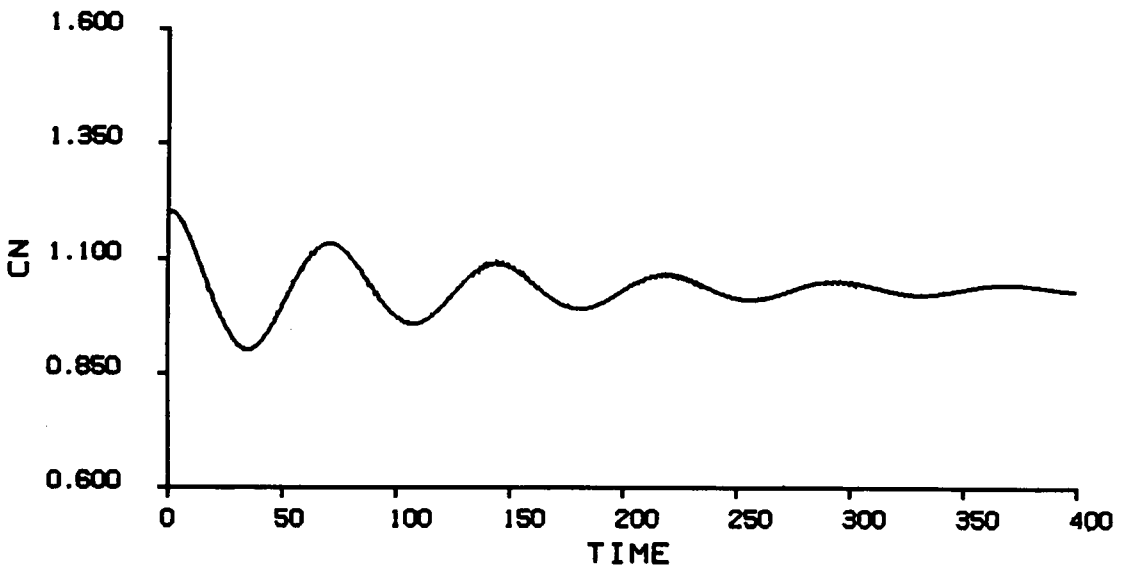

(e)

Figure 4.8. (e) Normal-force coefficient as a function of time.

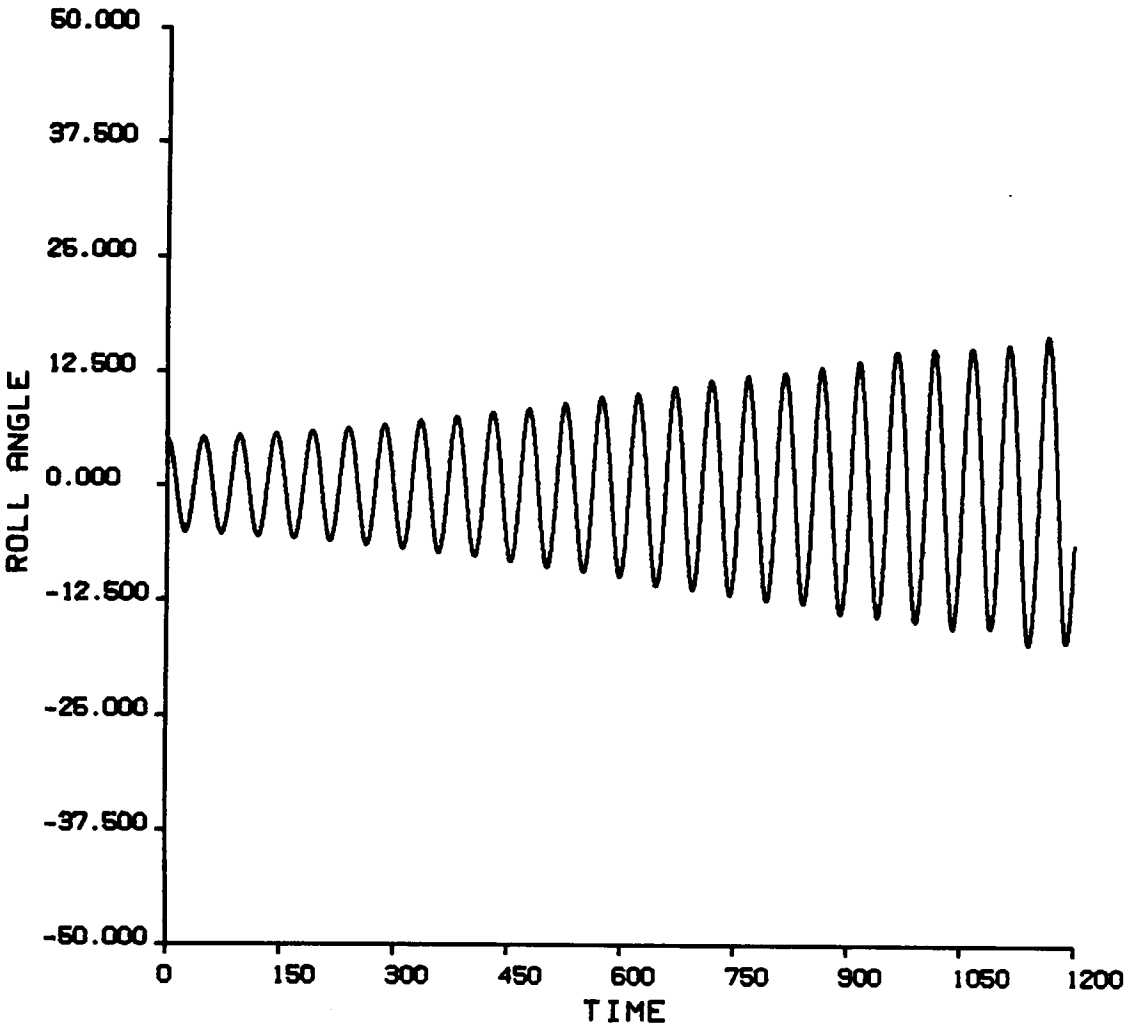

(a)

Figure 4.9. Numerical results for two degree of freedom in roll and pitch, $\alpha = 25°$, $\xi(0) = 5°$, $\dot{\xi}(0) = 0$:
(a) Roll angle as a function of time.

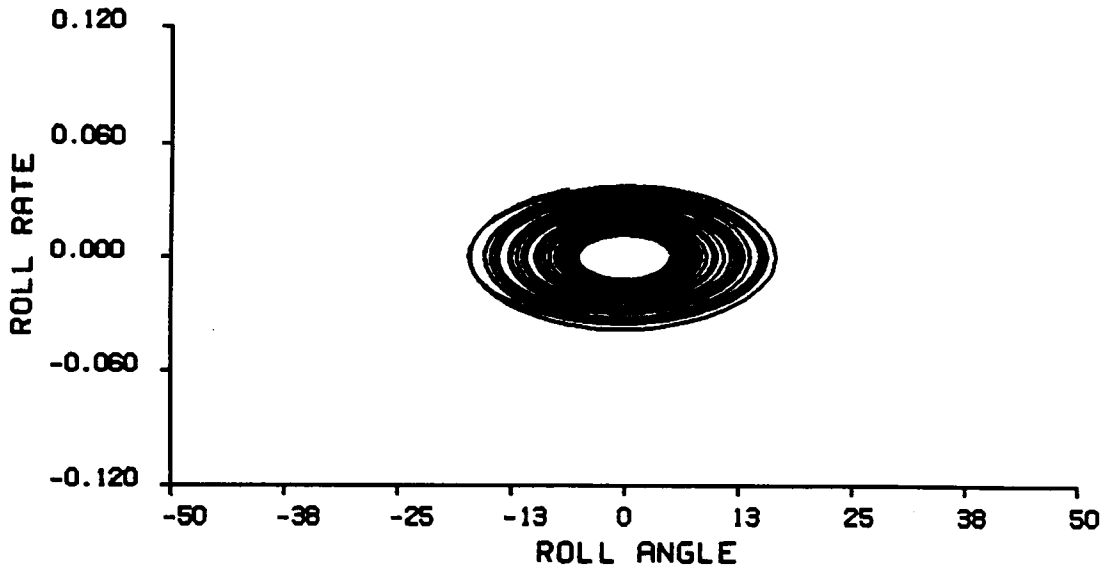

(b)

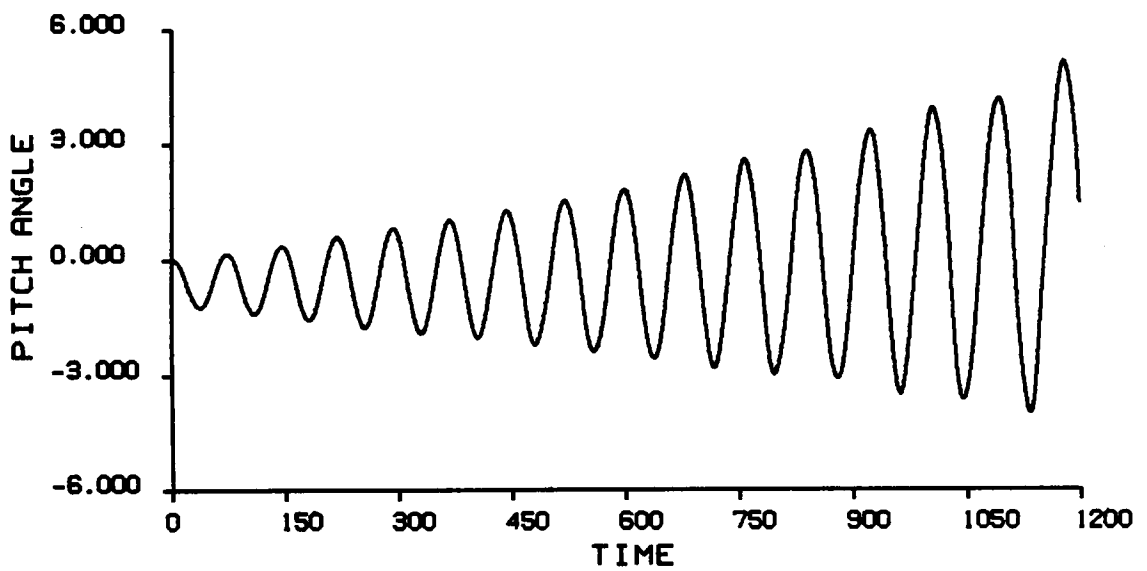

(c)

Figure 4.9 (b) Phase plane.
(c) Pitch angle as a function of time.

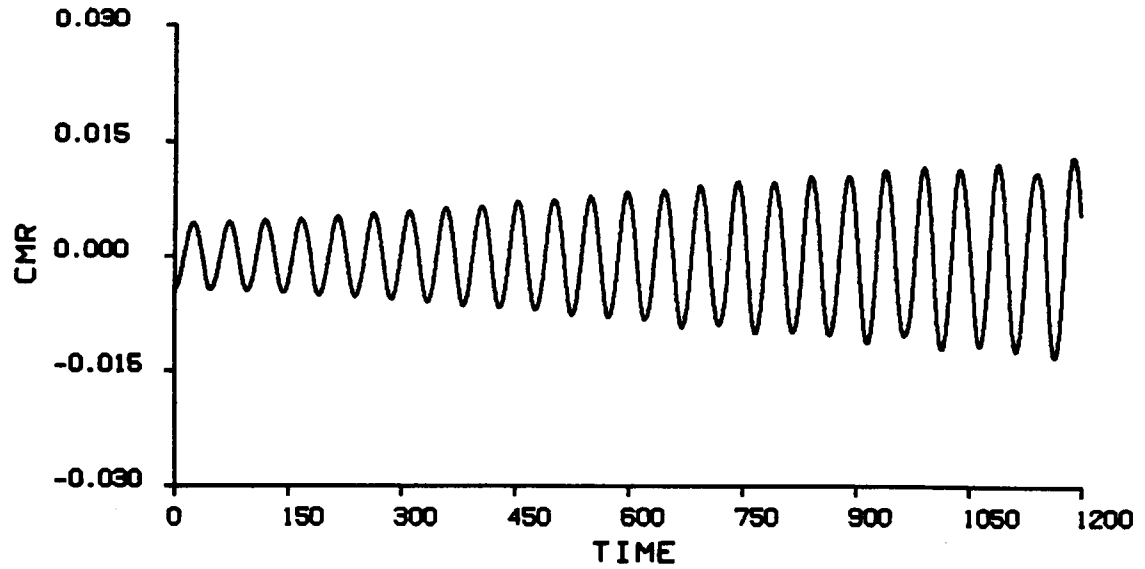

(d)

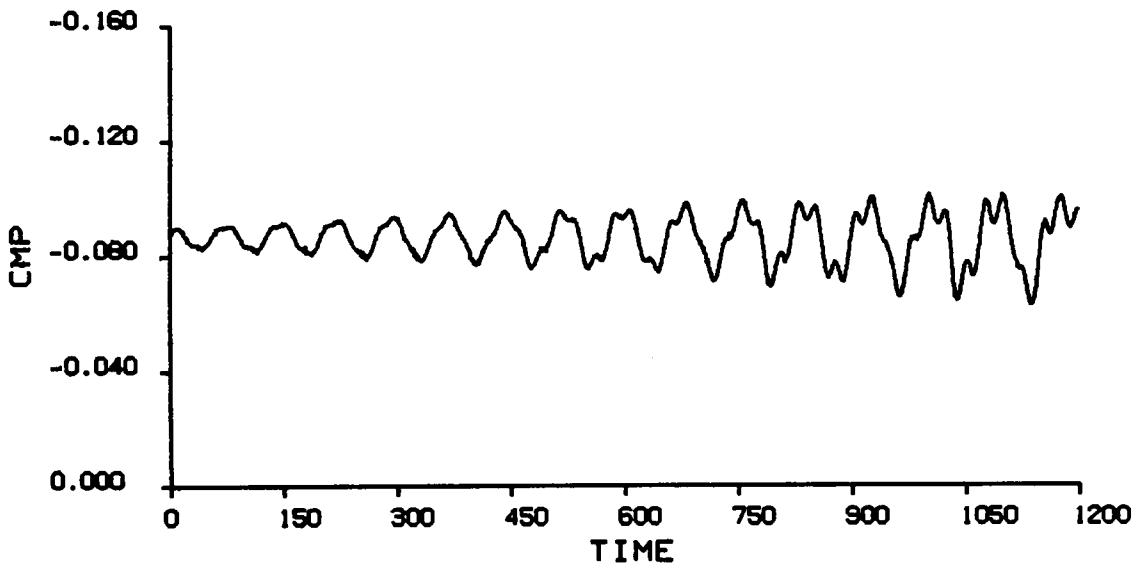

(e)

Figure 4.9. (d) Roll-moment coefficient as a function of time.
(e) Pitch-moment coefficient as a function of time.

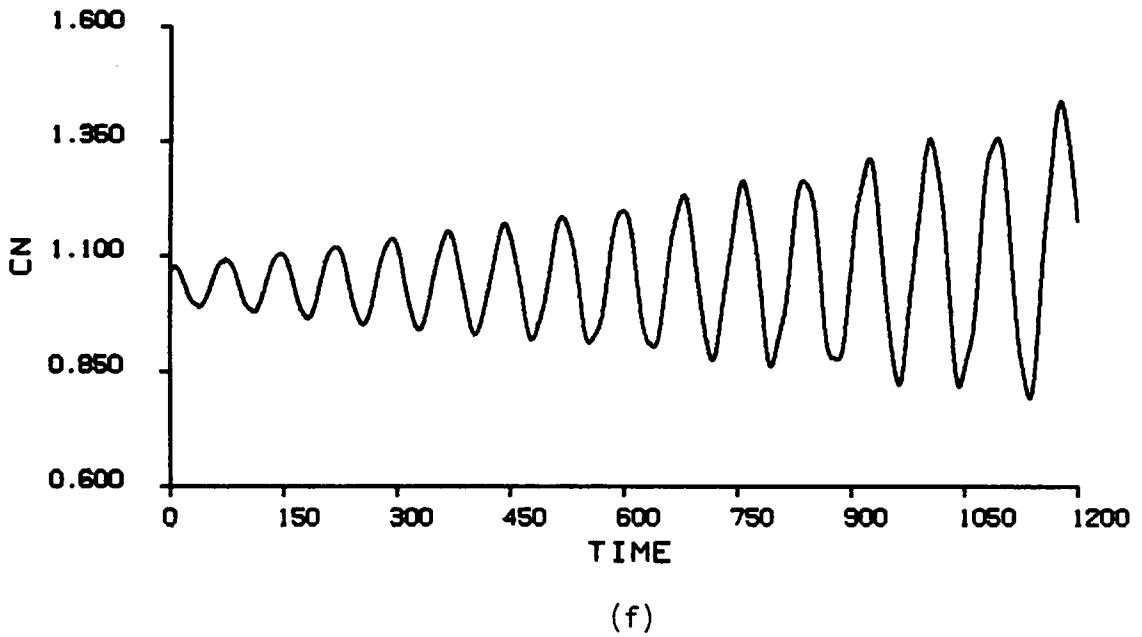

(f)

Figure 4.9. (f) Normal-force coefficient as a function of time.

respectively. The pitch-moment coefficient clearly appears to have several harmonics; it is not clear yet whether these are numerical problems or actually represent the response accurately.

4.4.5 Mathematical Modelling of Wing Rock

(One Degree of Freedom, α = 25 Degrees)

Since the problem at hand is nonlinear by nature, we assumed the rolling-moment coefficient to be a nonlinear function of ξ and $\dot{\xi}$ with the possibility of having a quintic nonlinearity, hence; we tried the following form

$$CMR = a_1\xi + a_2\dot{\xi} + a_3\xi^3 + a_4\xi^2\dot{\xi} + a_5\xi\dot{\xi}^2 + a_6\dot{\xi}^3 + a_7\xi^5 + a_8\xi^4\dot{\xi}$$
$$+ a_9\xi^3\dot{\xi}^2 + a_{10}\xi^2\dot{\xi}^3 + a_{11}\xi\dot{\xi}^4 + a_{12}\dot{\xi}^5 \qquad (4.22)$$

Then we fitted the roll-moment coefficient versus time curve of Figure 4.7c (with time scale enlarged) using a least-square fit to determine the coefficients a_i. By dropping one term at a time we were able to identify some terms that have negligible contribution to the roll moment. Consequently, a very helpful simpler model for a future analytical investigation is introduced

$$CMR = -(0.05601)\xi + (0.03791)\dot{\xi} + (0.05665)\xi^3 - (0.53231)\xi^2\dot{\xi}$$
$$+ (1.57346)\xi\dot{\xi}^2 + (0.04961)\xi^5 + (0.69800)\xi^4\dot{\xi} \qquad (4.23)$$

where the values of a_i are for one degree of freedom in roll and angle of attack α = 25 degrees. Figure 4.10 shows the predicted roll-moment coefficient versus time as it is given in Figure 4.7c and the

"analytical" one as it is computed by Equation (4.23). In part 4.10a we found the roll-moment coefficient of Figure 4.7c using only a_1 and in part 4.10b, 4.10c, 4.10d, 4.10e, 4.10f, and 4.10g we added one term at a time until in part 4.10g we obtained the best possible fit. From the above analysis one can conclude that quintic nonlinearities are important and must be considered when modeling wing rock mathematically.

Mathematical modelling of the two-degree-of-freedom wing rock is being investigated.

4.4.6 Concluding Remarks

The present results lead to the following conclusions:

(1) Below the first critical angle of attack (approximately 18 or 19 degrees), all disturbances decay for both one and two degrees of freedom.

(2) The first critical angle appears to be the same for one and two degrees of freedom.

(3) For one degree of freedom in roll, when the angle of attack is above the first critical angle, the motion develops a limit cycle. The higher the angle of attack, the faster the limit cycle develops.

(4) For two degrees of freedom in roll and pitch, when the angle of attack is above the first critical angle and below the second critical angle (approximately 23 degrees), the motion is almost entirely in roll. The deviation in the pitch angle from the static angle of attack is small and has both a steady and an oscillatory component. The mean angle of attack increases slightly.

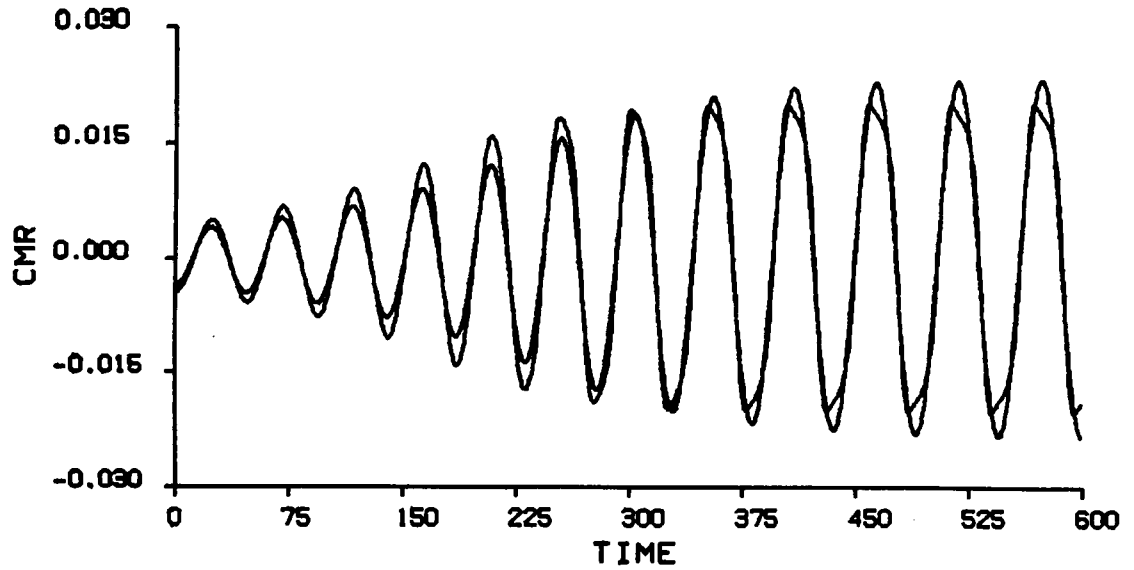

(a)

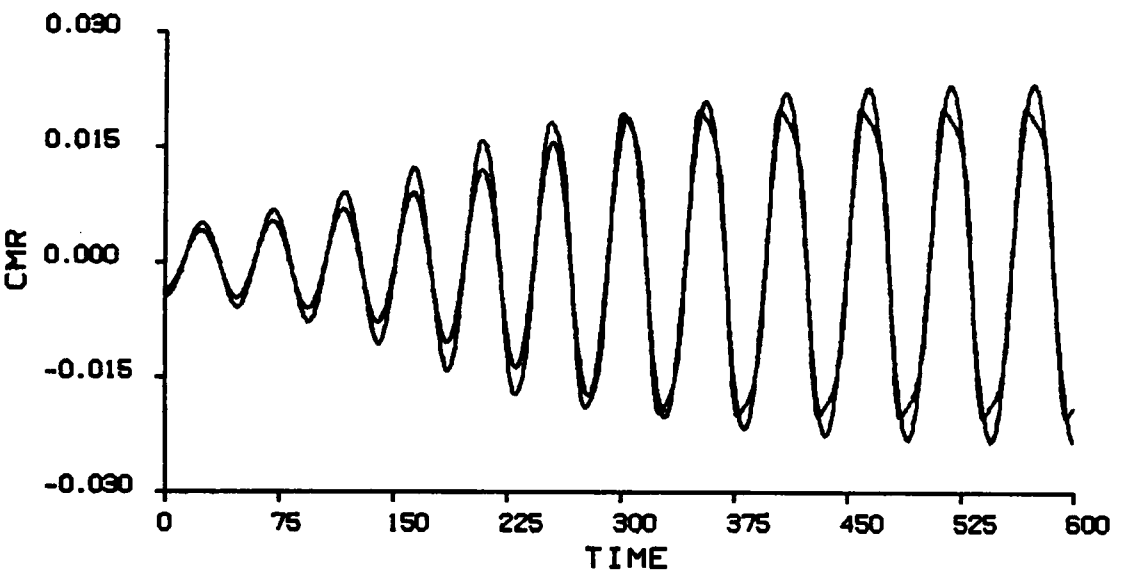

(b)

Figure 4.10. Numerical results for the "predicted" and the "analytical" solutions of the roll-moment coefficient for the case of Figure 4.7(c).
(a) One term fit.
(b) Two term fit.

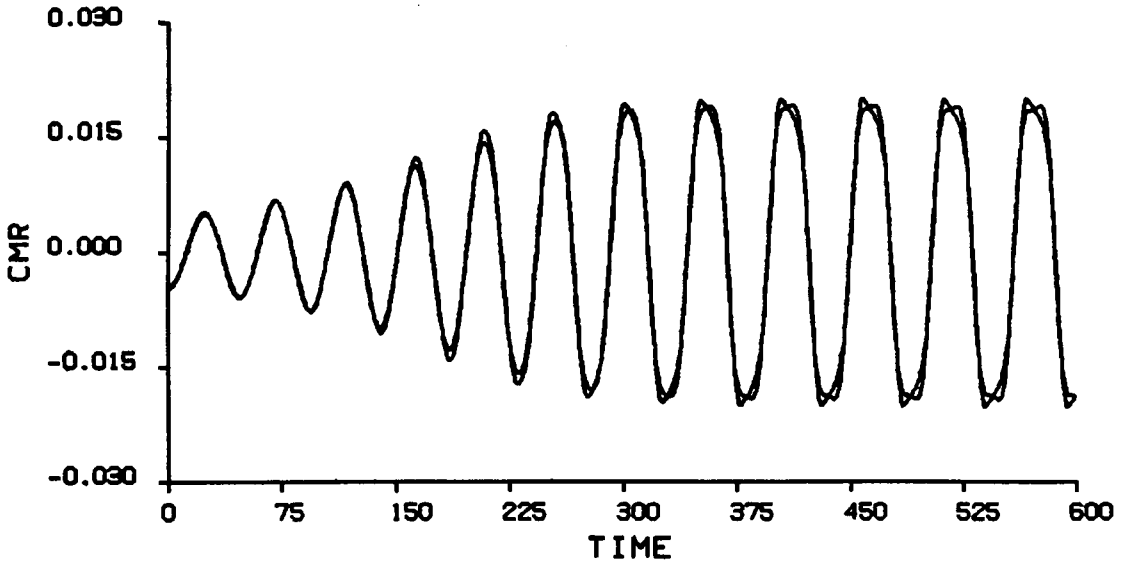

(c)

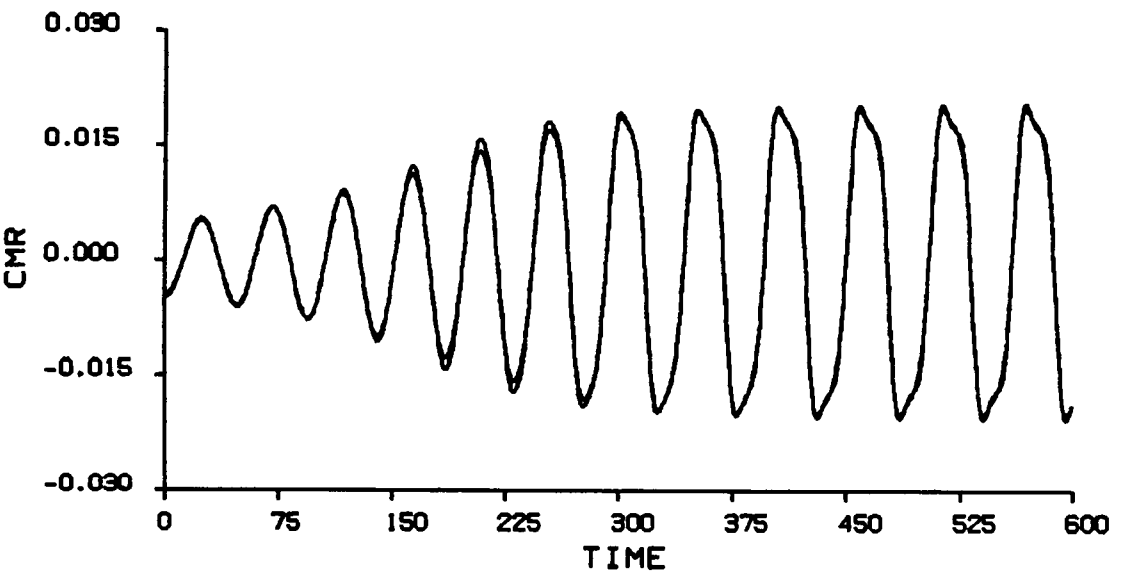

(d)

Figure 4.10. (c) Three term fit.
(d) Four term fit.

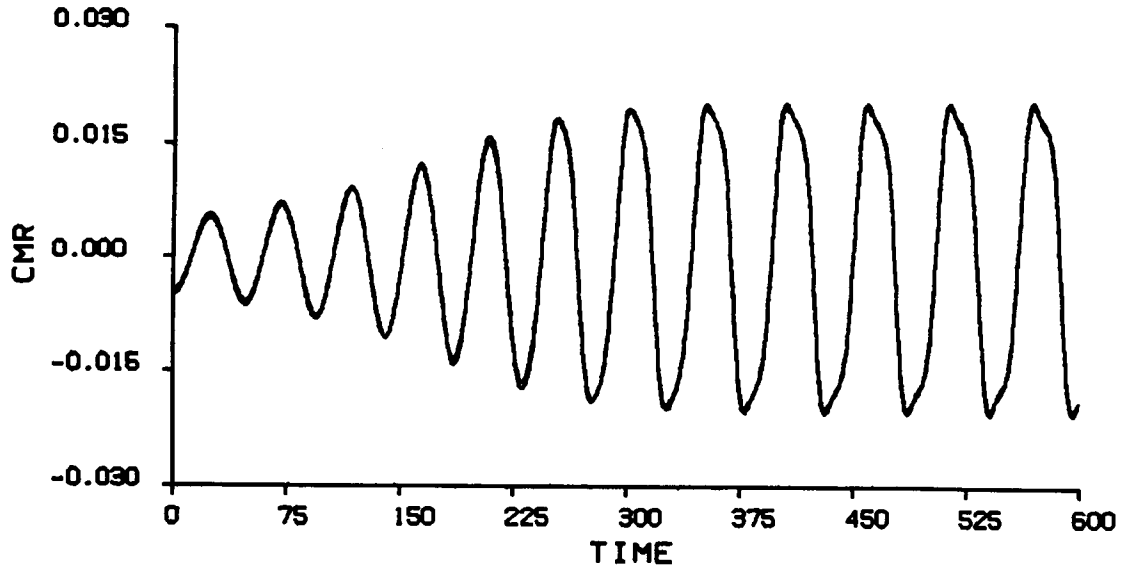

(e)

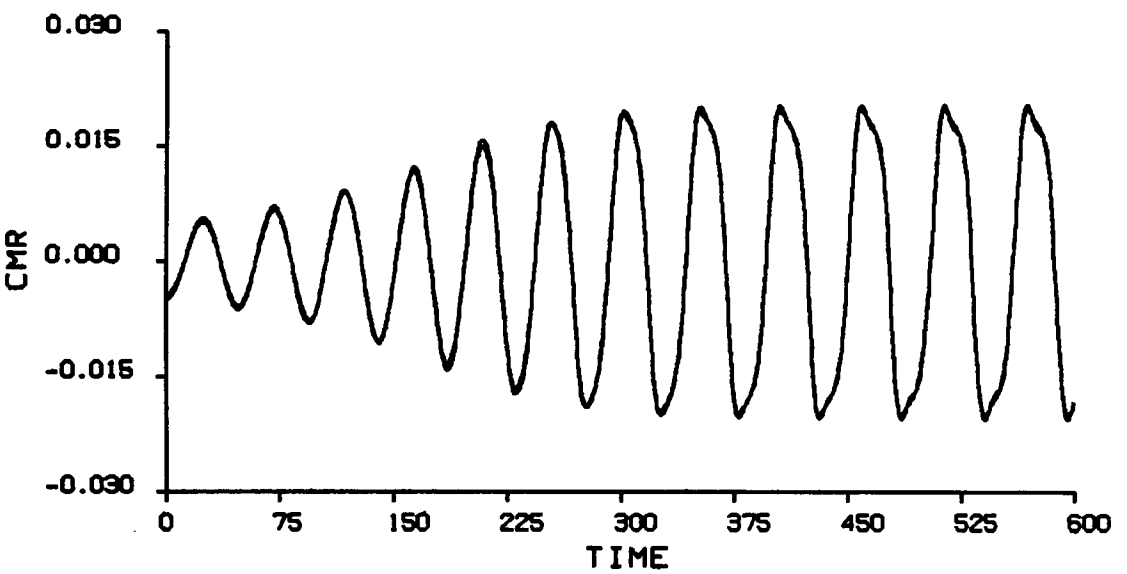

(f)

Figure 4.10. (e) Five term fit.
(f) Six term fit.

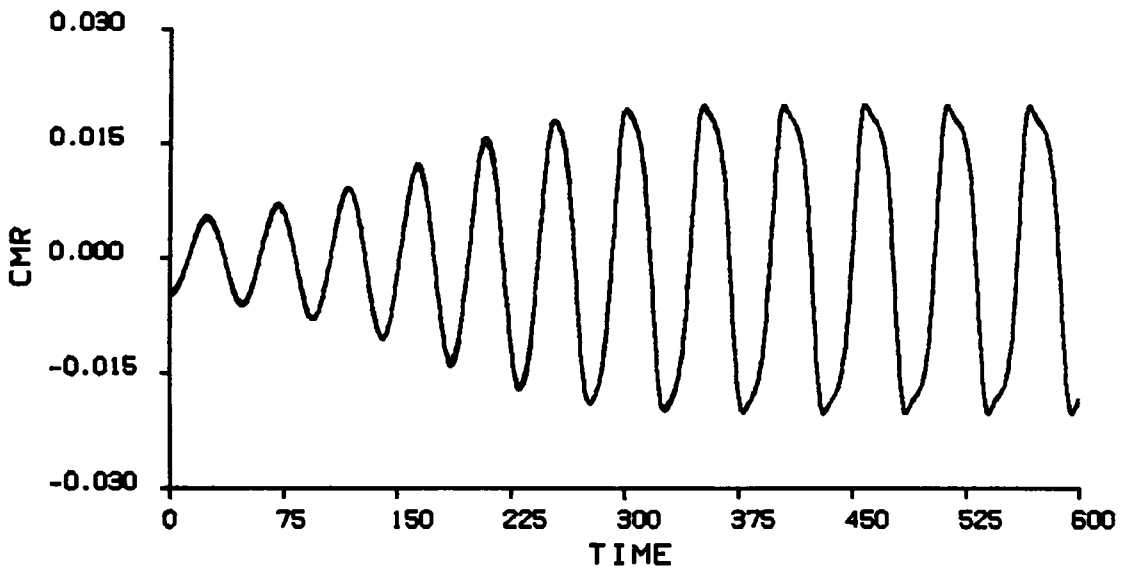

(g)

Figure 4.10. (g) Seven term fit.

(5) For two degrees of freedom, when the angle of attack is above the second critical angle, the motion consists of significant roll and pitch components.

(6) For two degrees of freedom, the time for a steady state to develop increases rapidly with the amplitude of the pitch motion. As a result, the amplitude of the roll motion for two degrees of freedom is considerably less than it is for one degree of freedom at a given time after the same initial disturbance.

(7) For one degree of freedom in pitch, the motion always decays to the static equilibrium position.

(8) For one degree of freedom, quintic nonlinearities must be included when modeling wing rock mathematically.

CHAPTER V

APPLICATION OF THE GENERAL UNSTEADY VORTEX-LATTICE METHOD TO MULTIPLE CLOSE-COUPLED LIFTING SURFACES

5.1 Introduction

The general unsteady vortex-lattice method described in Chapter II can be extended to model flows past configurations of multiple lifting surfaces. One such extension is discussed here.

The mutual interference of the lifting surfaces occurs through the no-penetration condition. When the normal component of the velocity at a control point on one of the lifting surfaces is considered, the induced velocity from all the lifting surfaces and their wakes is taken into account. This makes it necessary to establish a scheme of communication among the various components of the configuration.

First the present scheme of communication among the various components is established. Then several numerical examples are discussed.

5.2 Communication Among the Various Lifting Surfaces

There is a reference frame attached to each of the lifting surfaces and one attached to the ground. These are called body-fixed (B-F) and ground-fixed (G-F) reference frames, as in Chapter II. The position vector of the origin of a B-F reference frame and a set of Euler angles locate and orient the B-F frame, and hence the lifting surface. The scheme for the Euler angles is the same as that given in Section 2.2.

For each lifting surface, the three components of the position vector and the three Euler angles are independnent functions of time. Thus, each lifting surface has six degrees of freedom.

The position vector of B-F frame n is denoted $\vec{R}_n$ and it is understood that the components of $\vec{R}_n$ are given in the G-F frame:

$$\vec{R}_n = \begin{Bmatrix} X_n \\ Y_n \\ Z_n \end{Bmatrix}^T \begin{Bmatrix} \vec{I} \\ \vec{J} \\ \vec{K} \end{Bmatrix} \tag{5.1}$$

The difference between two position vectors is given by

$$\vec{R}_{nm} = \vec{R}_m - \vec{R}_n = \begin{Bmatrix} X_m - X_n \\ Y_m - Y_n \\ Z_m - Z_n \end{Bmatrix}^T \begin{Bmatrix} \vec{I} \\ \vec{J} \\ \vec{K} \end{Bmatrix} \tag{5.2}$$

In other words $\vec{R}_{nm}$ is the position of the origin of B-F frame m relative to the origin of B-F frame n.

The components of $\vec{R}_{nm}$ can be found in any of the B-F frames. For example, in B-F frame n,

$$\vec{R}_{nm} = \begin{Bmatrix} X_m - X_n \\ Y_m - Y_n \\ Z_m - Z_n \end{Bmatrix}^T [C_n]^T \begin{Bmatrix} \vec{i}_n \\ \vec{j}_n \\ \vec{k}_n \end{Bmatrix} \tag{5.3}$$

where the transformation matrix has precisely the form given by Equation (2.2). The Euler angles are those of B-F frame n.

In Figure 5.1, the B-F coordinate systems and one G-F system are shown. In addition, the position vectors of the origins, $\vec{R}_1$ and $\vec{R}_2$, and the relative position vector $\vec{R}_{12}$ are shown. Point P denotes any point in space; its position is given by $\vec{R}$ in the G-F system, by $\vec{r}_1$ and $\vec{r}_2$ in the B-F systems. In the implementation of the general unsteady vortex lattice method, one must be able to obtain $\vec{r}_1$ when $\vec{r}_2$ is given. A slight complication arises because $\vec{r}_2$ is given in terms of B-F frame 2, $\vec{R}_1$ and $\vec{R}_2$ are given in terms of the G-F frame, and $\vec{r}_1$ is desired in terms of B-F frame 1. The procedure is described in general next.

One can write

$$\vec{r}_m = \begin{Bmatrix} x_m \\ y_m \\ z_m \end{Bmatrix}^T \begin{Bmatrix} \vec{i}_m \\ \vec{j}_m \\ \vec{k}_m \end{Bmatrix} \quad \text{and} \quad \vec{r}_n = \begin{Bmatrix} x_n \\ y_n \\ z_n \end{Bmatrix}^T \begin{Bmatrix} \vec{i}_n \\ \vec{j}_n \\ \vec{k}_n \end{Bmatrix} \tag{5.4}$$

It follows from the discussion in Chapter II that for B-F frame m

$$\begin{Bmatrix} \vec{i}_m \\ \vec{j}_m \\ \vec{k}_m \end{Bmatrix} = [C_m] \begin{Bmatrix} \vec{I} \\ \vec{J} \\ \vec{K} \end{Bmatrix} \tag{5.5}$$

which can be written in B-F frame n

$$\begin{Bmatrix} \vec{i}_m \\ \vec{j}_m \\ \vec{k}_m \end{Bmatrix} = [C_m][C_n]^T \begin{Bmatrix} \vec{i}_n \\ \vec{j}_n \\ \vec{k}_n \end{Bmatrix} \tag{5.6}$$

From Equations (5.4) and (4.6), one can write $\vec{r}_m$ as seen in B-F frame n

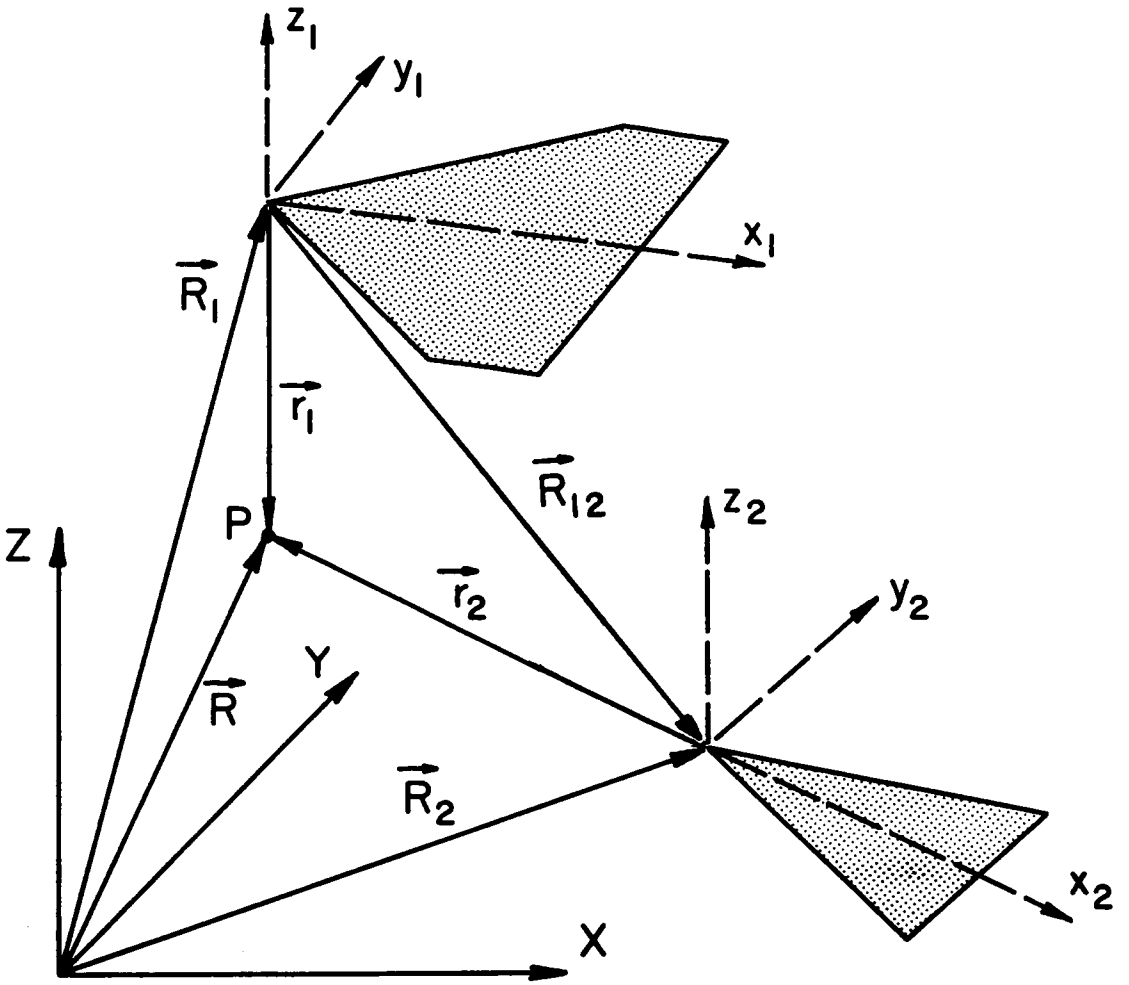

Figure 5.1. Ground-fixed and body-fixed coordinate systems used to describe multi-lifting-surface configurations.

$$\vec{r}_m = \begin{Bmatrix} x_m \\ y_m \\ z_m \end{Bmatrix}^T [C_m][C_n]^T \begin{Bmatrix} \vec{i}_n \\ \vec{j}_n \\ \vec{k}_n \end{Bmatrix} \tag{5.7}$$

Using Figure 5.1 as a reference, one can easily arrive at the following:

$$\vec{r}_n = \vec{R}_{nm} + \vec{r}_m \tag{5.8}$$

which, from Equations (5.3) and (5.7), can be written as

$$\begin{Bmatrix} x_n \\ y_n \\ z_n \end{Bmatrix}^T \begin{Bmatrix} \vec{i}_n \\ \vec{j}_n \\ \vec{k}_n \end{Bmatrix} = \begin{Bmatrix} X_m - X_n \\ Y_m - Y_n \\ Z_m - Z_n \end{Bmatrix}^T [C_n]^T \begin{Bmatrix} \vec{i}_n \\ \vec{j}_n \\ \vec{k}_n \end{Bmatrix}$$

$$+ \begin{Bmatrix} x_m \\ y_m \\ z_m \end{Bmatrix}^T [C_m][C_n]^T \begin{Bmatrix} \vec{i}_n \\ \vec{j}_n \\ \vec{k}_n \end{Bmatrix} \tag{5.9}$$

or

$$\begin{Bmatrix} x_n \\ y_n \\ z_n \end{Bmatrix} = [C_n] \left[\begin{Bmatrix} X_m - X_n \\ Y_m - Y_n \\ Z_m - Z_n \end{Bmatrix} + [C_m]^T \begin{Bmatrix} x_m \\ y_m \\ z_m \end{Bmatrix} \right] \tag{5.10}$$

Using Equation (5.10) one can specify the coordinates of a point relative to B-F frame m and then determine its coordinates in B-F n. This is the procedure used when the velocity induced by lifting surface m and its wake is desired at a given point in B-F frame n.

In addition to the need for specifiying position vectors in different reference frames, there is the need to specify the velocity vector in the various frames. The useful transformations are described

next. The velocity of the origin of each frame is specified in terms of the G-F frame:

$$\vec{V}_n^G = V_{nx}^G \vec{I} + V_{ny}^G \vec{J} + V_{nz}^G \vec{K} = \begin{Bmatrix} V_{nx}^G \\ V_{ny}^G \\ V_{nz}^G \end{Bmatrix}^T \begin{Bmatrix} \vec{I} \\ \vec{J} \\ \vec{K} \end{Bmatrix} \tag{5.11}$$

which can be written in B-F frame n

$$\vec{V}_n = \begin{Bmatrix} V_{nx}^G \\ V_{ny}^G \\ V_{nz}^G \end{Bmatrix}^T [C_n]^T \begin{Bmatrix} \vec{i}_n \\ \vec{j}_n \\ \vec{k}_n \end{Bmatrix} \tag{5.12}$$

or

$$\begin{Bmatrix} V_{nx} \\ V_{ny} \\ V_{nz} \end{Bmatrix} = [C_n] \begin{Bmatrix} V_{nx}^G \\ V_{ny}^G \\ V_{nz}^G \end{Bmatrix} \tag{5.13}$$

Note that superscript G is not used on lift-hand side of equation (5.13) to indicate that the velocity is in the local B-F frame n.

Once the communication scheme is completed and ready to be used, then the procedure of applying the unsteady vortex-lattice method to multi-lifting surface configurations is very much the same as the one used for the single lifting surface (see Chapter II). There is, however; two miner but important differences. First, when satisfying the no-penetration condition, Equation (2.14) takes the form

$$\sum_{j=1}^{M} A_{ij} G_j = [(\vec{V}_{LS} - \vec{V}_F) \cdot \vec{n}]_i \tag{5.14}$$

for i = 1, 2, ..., M; where M is the sum over all the elements in all the components of the complete configuration; $\vec{V}_F$ is the velocity induced by all the wakes of all components at the control point i, $\vec{V}_{LS}$ is the velocity of the lifting surface which contains point i, and the rest of the terms in Equation (5.14) have the same meaning as before. Second, when convecting the nodes of the lattice in the wake, Equation (2.16) would still have the same form, i.e.,

$$\vec{r}(t + \Delta t) = \vec{r}(t) + [\vec{V}(t) - \vec{V}_{LS}]\Delta t \qquad (5.15)$$

however, $\vec{V}(t)$ here is the velocity induced, at the node being convected, by the combined bound vortex systems and the wakes of all the components of the complete configuration. Furthermore, $\vec{V}_{LS}$ is the velocity of the lifting surface whose wake contains the node being convected.

5.3 Numerical Examples

Examples of steady and unsteady flows are considered. Here we consider a planform that resembles the X-29 which consists of two flat canards and slightly cambered main wing. Figure 5.2 shows the planform and the mesh used to make all the calculations discussed in this section.

The steady-flow results were obtained from the general unsteady program. The configuration was given an impulsive start and then moved at constant velocity until a steady state developed.

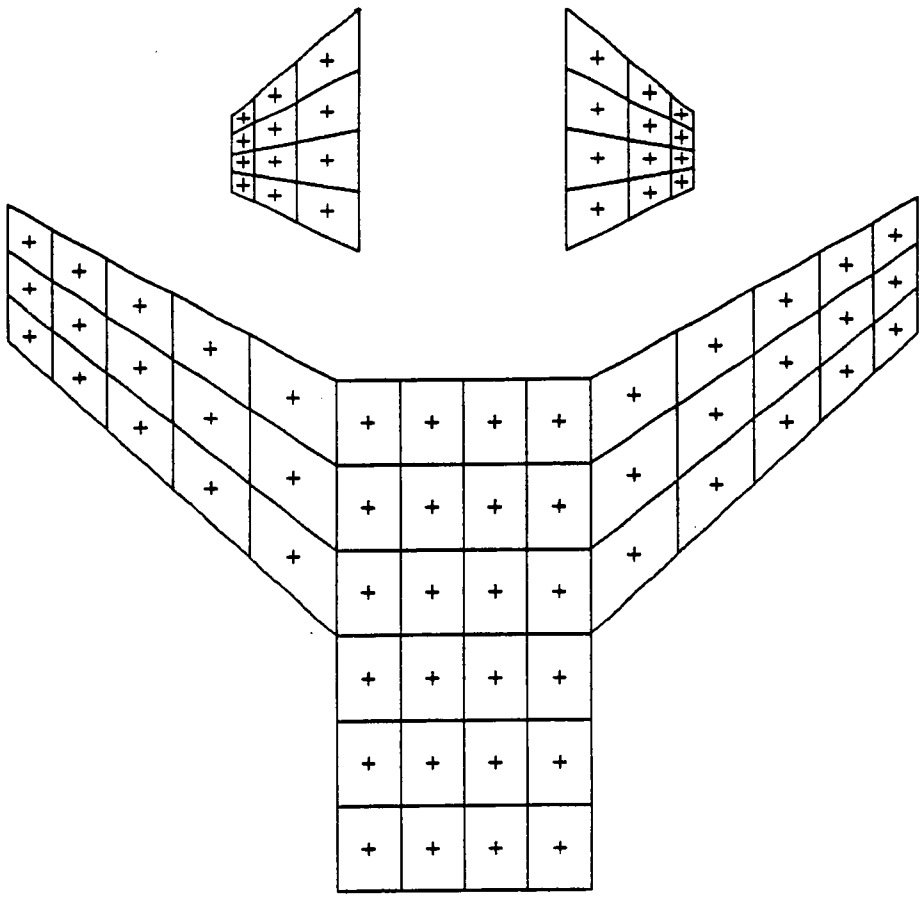

Figure 5.2. Planform and mesh for a configuration resembling the X-29.

5.3.1 Steady Flow

A top view of the computed wakes for the configuration shown in Figure 5.2 are shown in Figure 5.3. In part a, only the wake adjoining the main wing is shown, while in part b only the wakes adjoining the canards are shown. Part c shows the complete flowfield. In Figure 5.4 the top, side, and front views of the complete flowfield are shown in parts (a), (b), and (c), respectively. The view in part a is a repeat of part c in Figure 5.3. The angle of attack of both canards is 15 degrees and that of the main wing is 9 degrees.

The loads on the various components are given in Table 5.1. The lift on the wing is descreased by the presence of the canards. For a given angle of attack of the main wing, the lift on the main wing decreases as the angle of attack of the canards increases. Of course, the lift on the canards increases with angle of attack. Moreover, the lift on the canards is increased by the presence of the main wing. This leads to the result that the lift on the ensemble remains virtually constant; however, the pitch moment changes markedly.

The reason for the loss of lift on the main wing can be found in Figure 5.5, where the difference in pressure across the main lifting surface is plotted as a function of position of the control point. In part a the results are for the main wing alone and in part b the results for the main wing in the presence of the canards. The drop in pressure on the main wing occurs directly under the wakes of the canards and is responsible for the loss in lift. For these results, the angle of attack of the canards is 15 degrees. The results for angles of attack

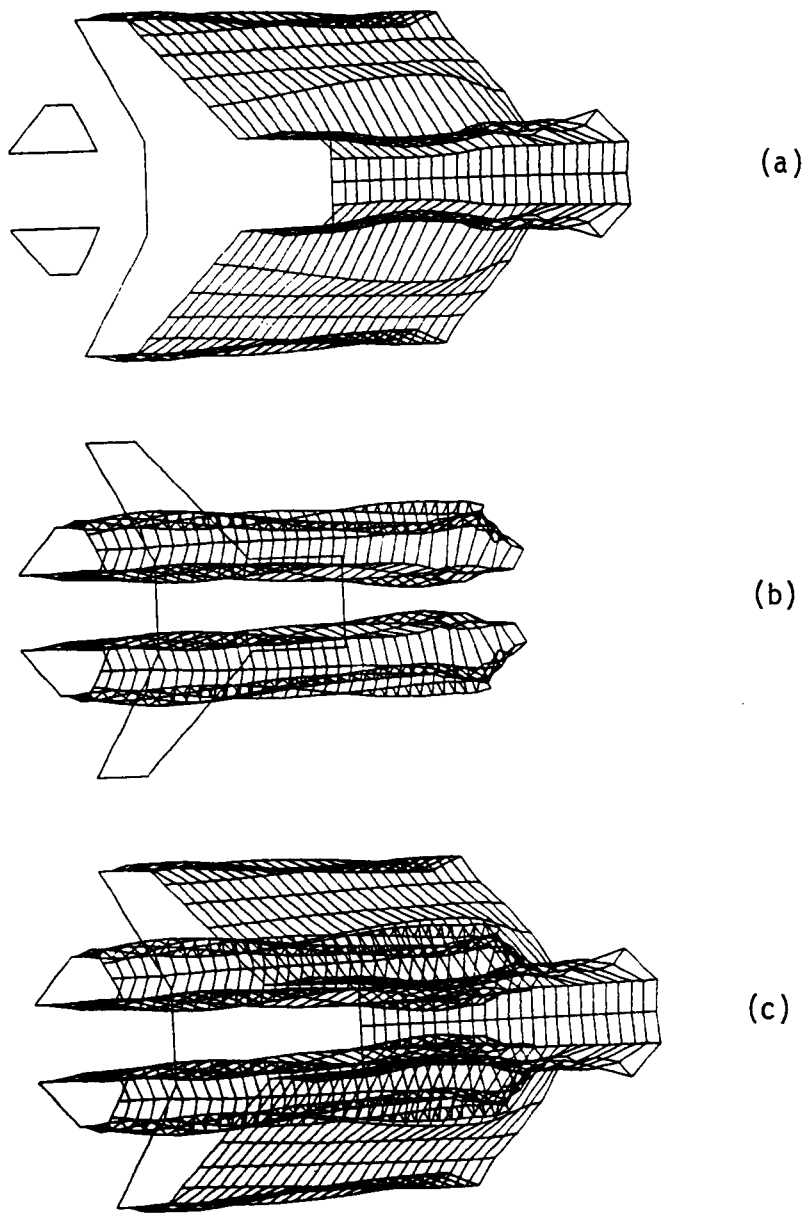

Figure 5.3. Top views of the computed wakes for steady flow past the configuration shown in Figure 5.2, $\alpha_{canards} = 15°$, $\alpha_{wing} = 9°$. (a) Wake of the main wing alone. (b) Wakes of the canards alone. (c) Combined wakes of canards and main wing.

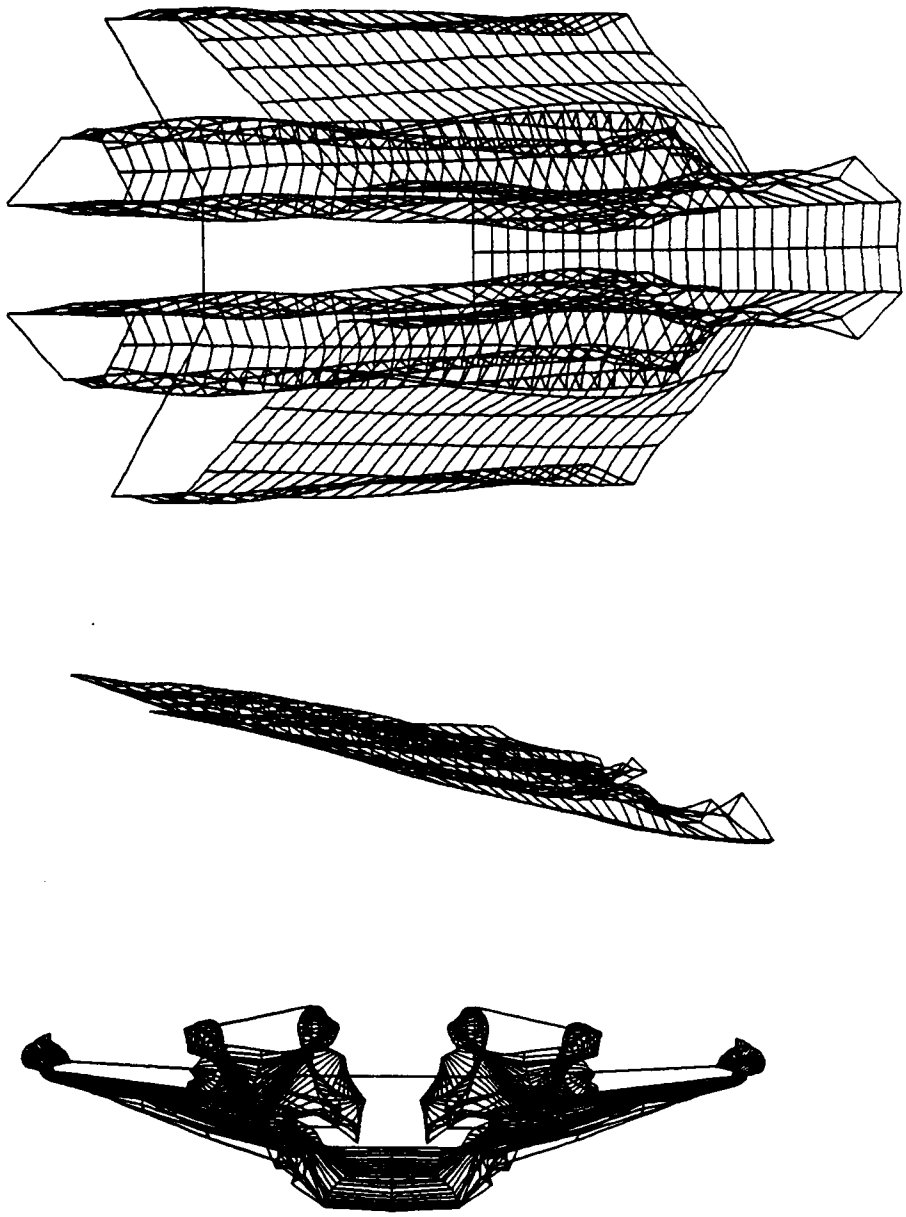

Figure 5.4. Computed wakes for steady flow past the configuration shown in Figure 5.2. (a) Top view, which is the same as Figure 5.3 part c. (b) Side view. (c) End view.

Table 5.1. Steady loads on canards and main wing.

Canard alone	Wing alone
(α=15°)	(α=9°)
CL = 0.570	CL = 0.451
CD = 0.153	CD = 0.061

α canard	Canard		Wing		Ensemble		
	CL	CD	CL	CD	CL	CD	CMP
10	0.422	0.074	0.405	0.064	0.407	0.056	0.009
15	0.665	0.178	0.379	0.060	0.419	0.076	0.019
20	0.930	0.339	0.341	0.054	0.422	0.085	0.033

α_{wing} = 9 degrees

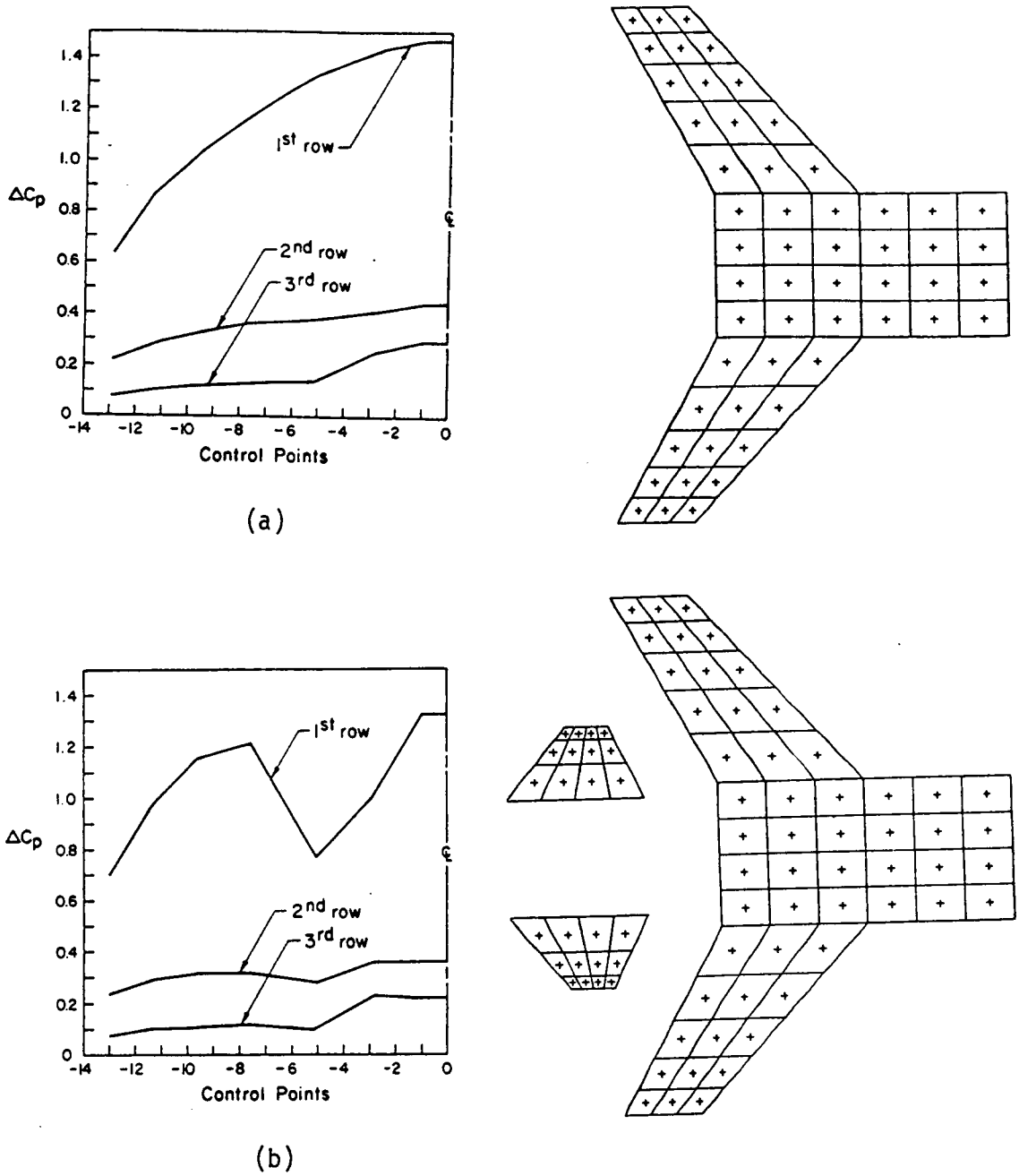

Figure 5.5. Calculated pressure distributions. (a) Main wing alone ($\alpha_{wing} = 9°$). (b) Canards and main wing ($\alpha_{canards} = 15°$).

of 10 and 20 degrees are shown in Figure 5.6. There is a larger loss in lift at larger angles of attack.

It should be mentioned that here the force and moment coefficients have the same definitions as in Section 2.7 except; however, for the ensemble the definitions are based on the sum of the areas and the sum of the chords of all components. These sums are called the effective area and the effective chord, respectively.

Using a finer mesh and changing the size of the time step (see Section 2.6.5.) created more uniformity between the elements in the wakes. Part a of Figure 5.7 shows the new mesh. Parts b, c, and d show rotational views of the flowfield of the main wing, the main canards, and the combination, respectively. This steady-state solution was obtained for $\alpha_{canard} = \alpha_{wing} = 8$ degrees. Comparing Figure 5.7 with Figure 5.3, one can see that the elements in the wakes in Figure 5.7 are uniform whereas those in Figure 5.3 are not. Morever, just as in Figure 5.5 where the interactions between the wakes of the canards and the main wing is clear, Figure 5.7, particularly part (c), shows how this interaction forces the wakes of the canards to move towards the main wing.

Using the new mesh, a static comparison with wind-tunnel data (Mason, 1986) was made. The steady state solutions are obtained where both of the canards and the main wing at equal angles of attack. In Figure 5.8 the load coefficients of the complete configuration are plotted as functions of the angle of attack of the main wing. Total lift coefficient (CLT), total drag coefficient (CDT), and total pitch-

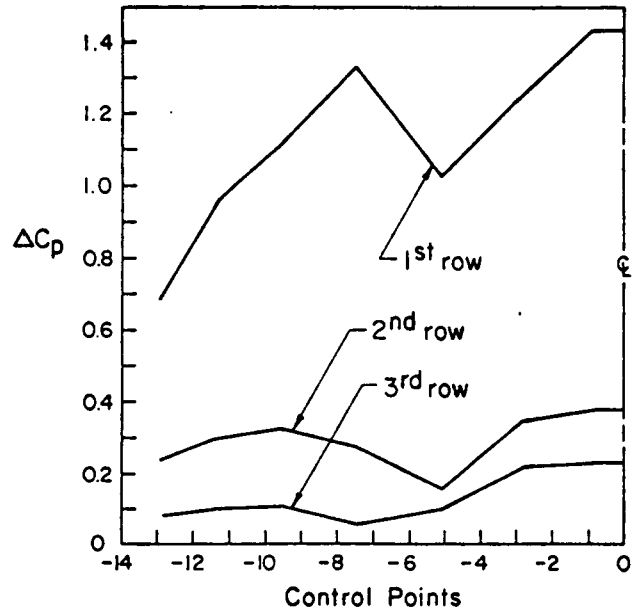

α = 10^0

(a)

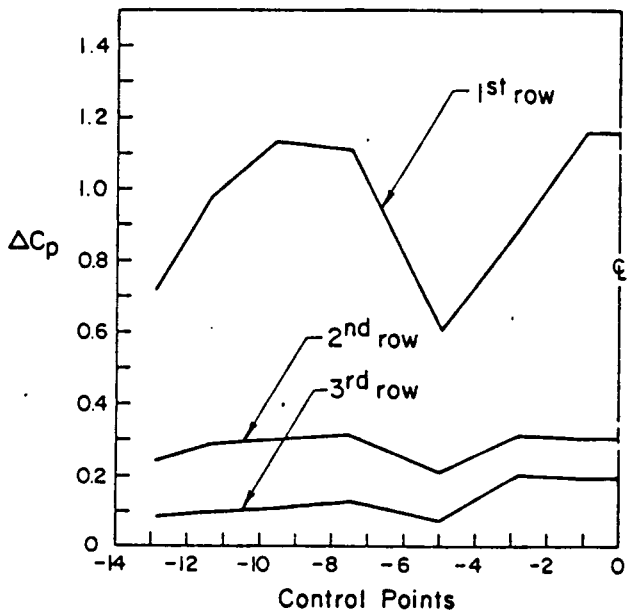

α = 20^0

(b)

Figure 5.6. Pressure distributions on the main wing for different angles of attack of the canards.

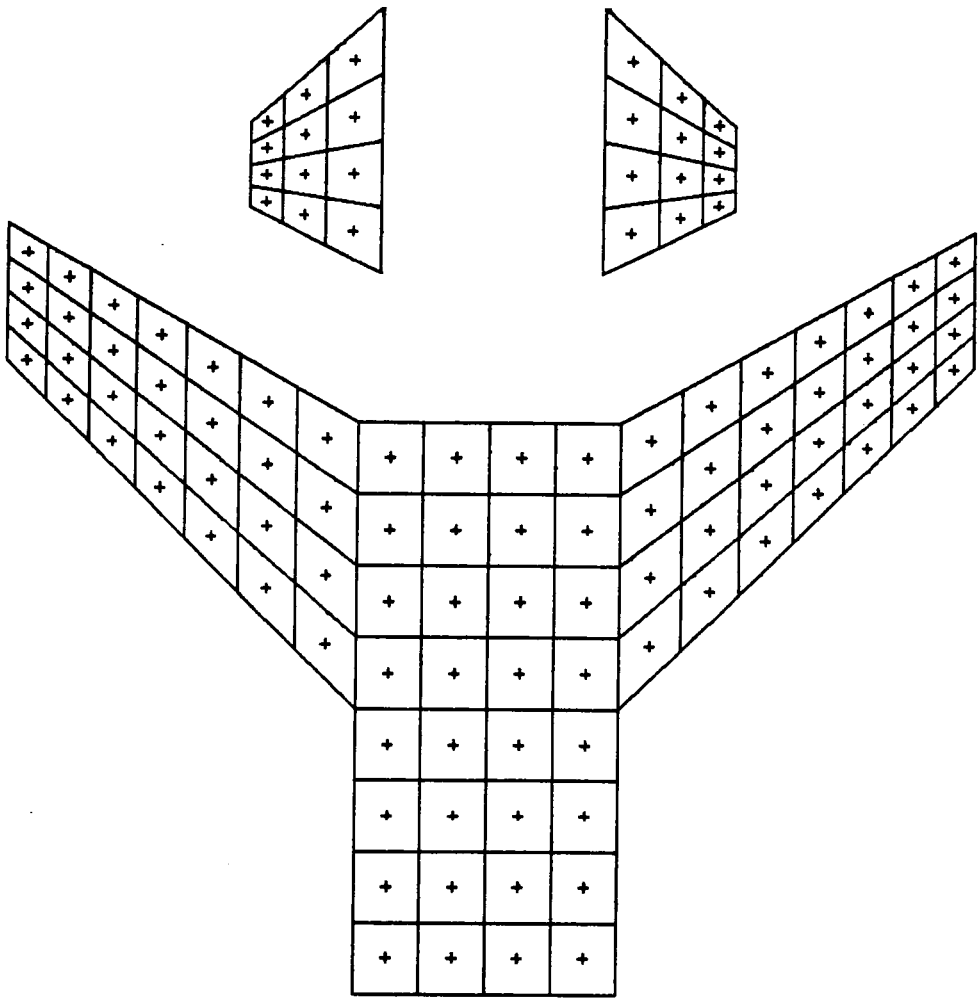

Figure 5.7. Rotational view of the computed wakes for steady flow past the planform shown in Figure 5.2 but with a different mesh. $\alpha_{canards} = \alpha_{wing} = 8°$. (a) The new mesh. (b) Wakes of the main wing alone. (c) Wakes of the canards alone. (d) Combined wakes of canards and main wing.

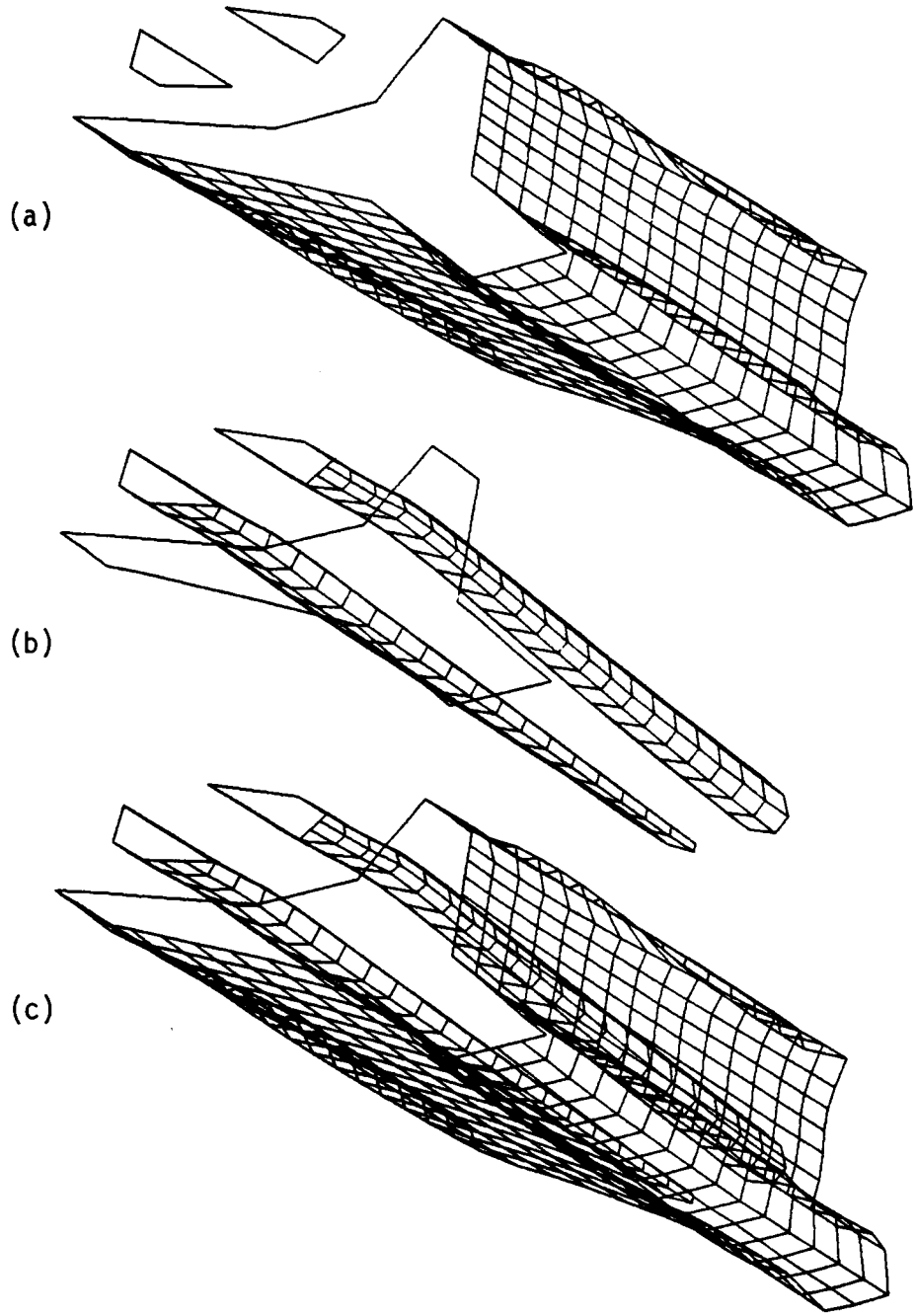

Figure 5.7. (continued).

moment coefficient are given in part a, b, and c, respectively. Each part includes two different sets of experimental data and two different curves that represent the computations. One of the computed curve is based on a correction factor of the value 1.4966 which was provided with the wind-tunnel data. This correction factor is based on the relation between the area of the model and the area of the actual configuration. The other computed curve is with no correction. It is based on the effective area (the sum of the areas of all components) for the drag and the lift and on both the effective area and the effective chord (the sum of the chords of all components) for the moment coefficient. Considering the fact that, in the computations, part of the fuselage is not considered and viscous effects are not accounted for, one can see a quantitative and qualitative agreement with the experiments for the drag and the lift coefficients (Figures 5.8a and 5.8b). However, for the pitch-moment coefficient (Figure 5.8c) we see only a qualitative agreement with the experiment. The reason is being that the location of the axis, around which the computed moments were taken, is different from that of the experiment.

5.3.2 Unsteady Flow

Three examples of different nature are considered.

First example, using the same configuration shown in Figure 5.3, the angle of attack of the port canard undergoes a ramp increase from 15° to 18° while the angle of attack of the starboard canard undergoes a ramp decrease from 15° to 12°. The angles of attack of the port and

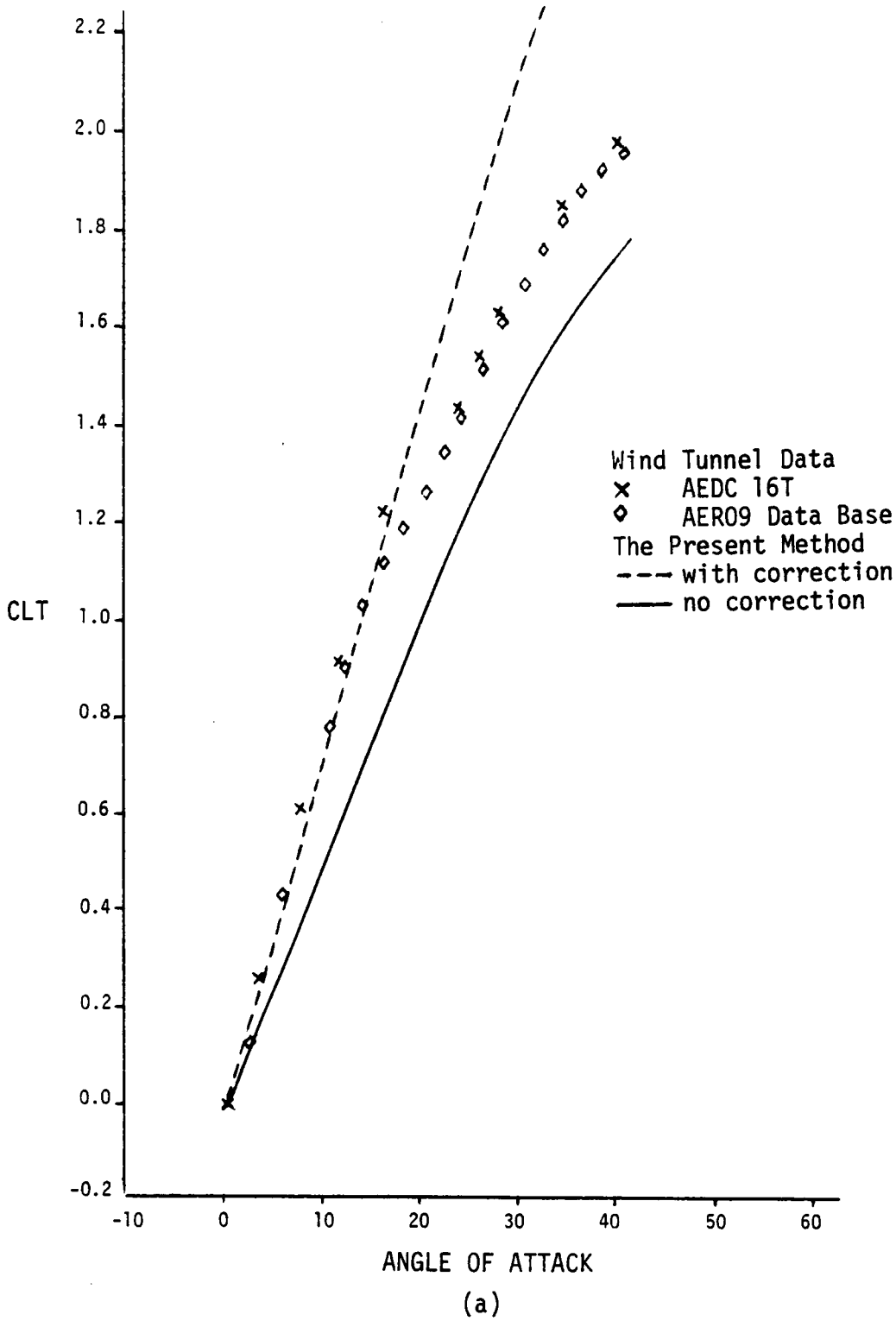

(a)

Figure 5.8. Total load coefficients as functions of angle of attack of the main wing:
(a) Total lift coefficient.

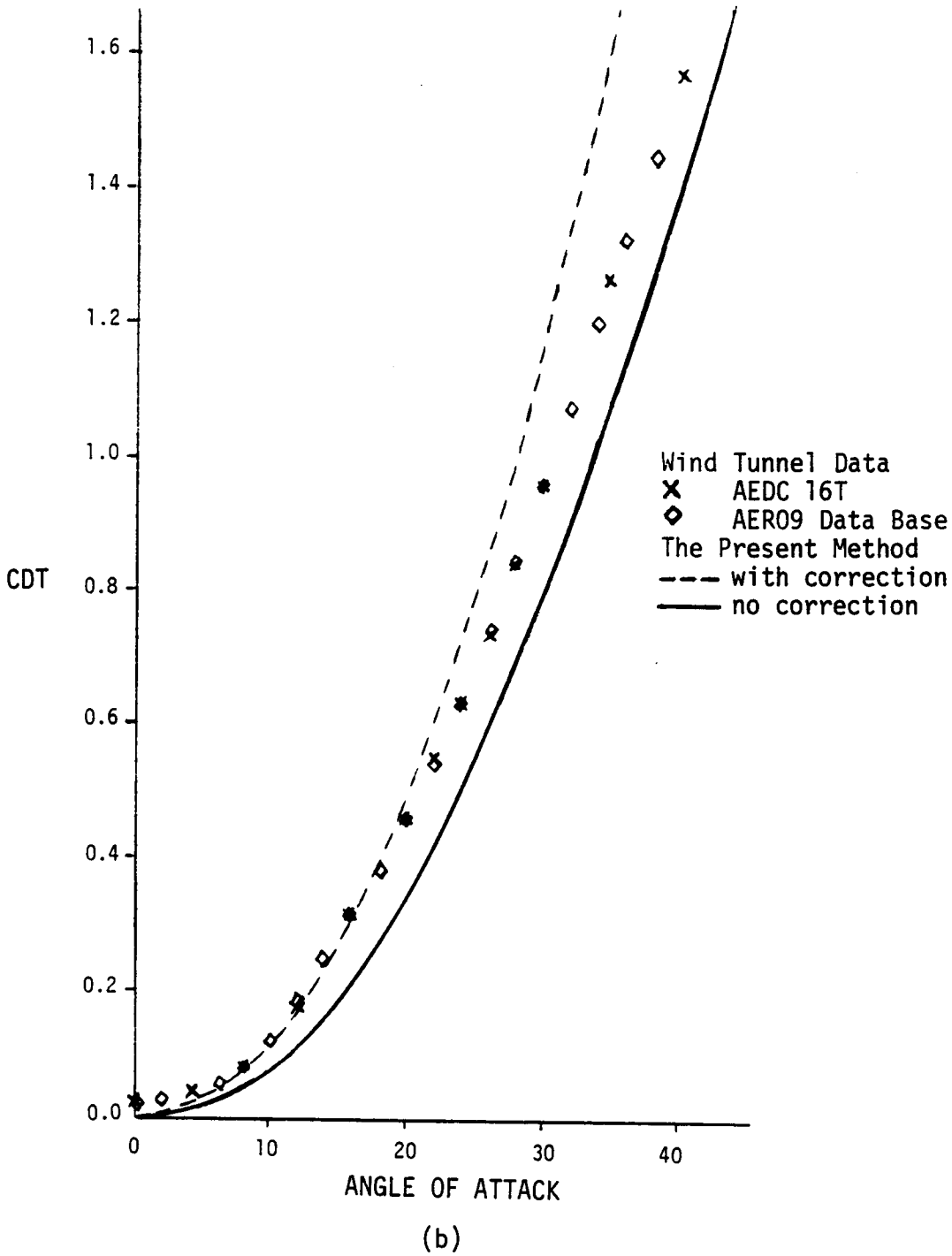

Figure 5.8. (b) Total drag coefficient.

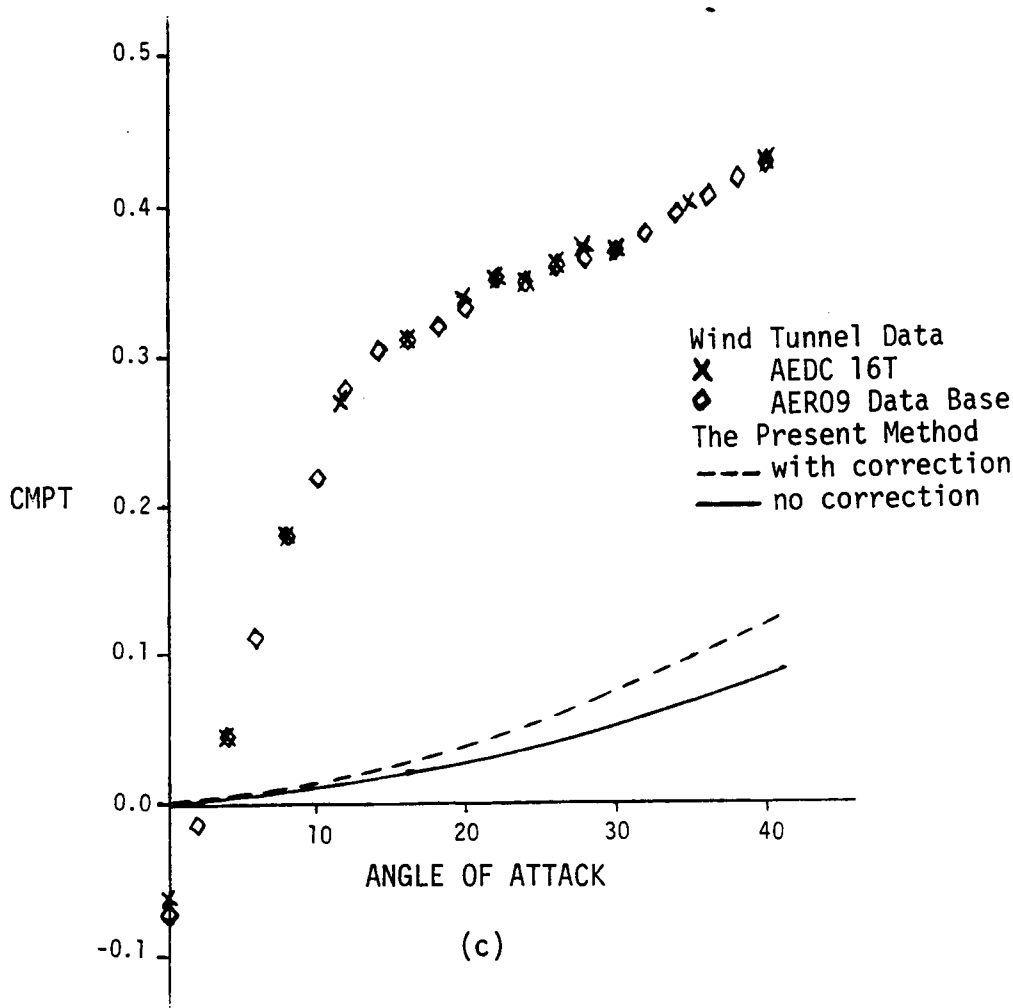

Figure 5.8. (c) Total pitch-moment coefficient.

starboard canards remain at 18 and 12 degrees, respectively. This period lasts as long as the period when the ramping motion occurred. Finally, the angles of attack return to 15° with ramp changes at the same rate as the original deflection. The main wing remains at 9 degrees during the whole ramping motion. The results are shown in Figure 5.9. In part a the angles of attack are plotted as functions of time. The normal-force coefficients on the individual components are shown in part b, and the force coefficients on the ensemble are shown in part c (CLT,CDT). As in the steady case lift remains virtually constant. The roll-moment coefficient (CMRT) is given in part d. During the ramping motion, the roll moment is not zero. But when the canards are stationary, the roll rapidly becomes very small. Apparently the increase in lift on one side and the accompanying decrease in lift on the corresponding side of the main wing also result in virtually no change in the roll moment. Roll must be accomplished with ailerons.

Second example, using the new mesh shown in Figure 5.7a, the steady-state solution, which was obtained for $\alpha_{canard} = \alpha'_{wing} = 10°$, was used as an initial condition for the following sinusoidal motion:

$$\theta(t) = 10 + 2.5 \sin(ft) \tag{5.16}$$

and

$$\dot{\theta}(t) = 2.5\, f \cos(ft) \tag{5.17}$$

with frequency $f = 0.10048$; where $\theta(t)$ is in degrees and t is the nondimensional time.

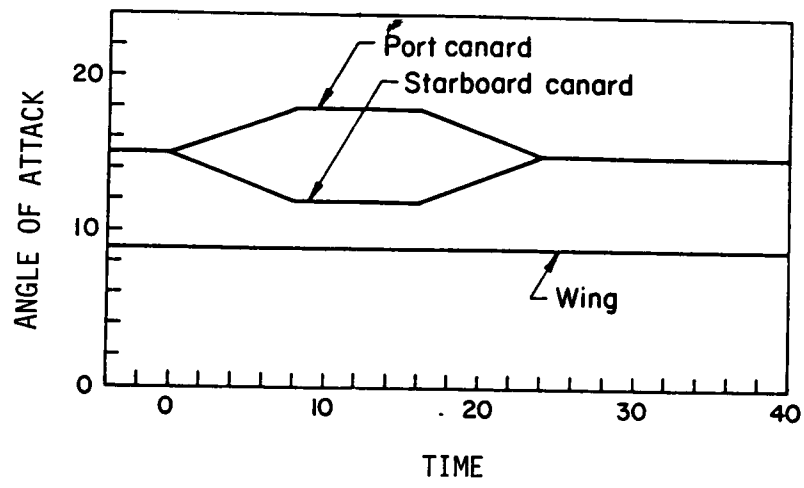

(a)

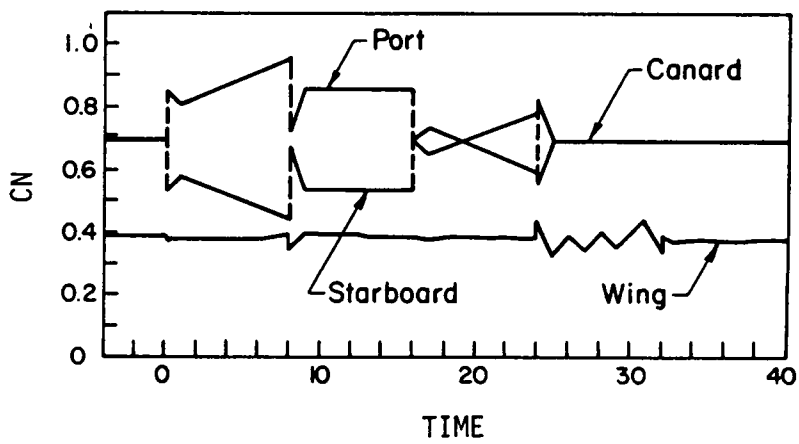

(b)

Figure 5.9. Ramping Motion:
(a) Angles of attack of the canards and the main wing as functions of time.
(b) Normal-force coefficients as functions of time.

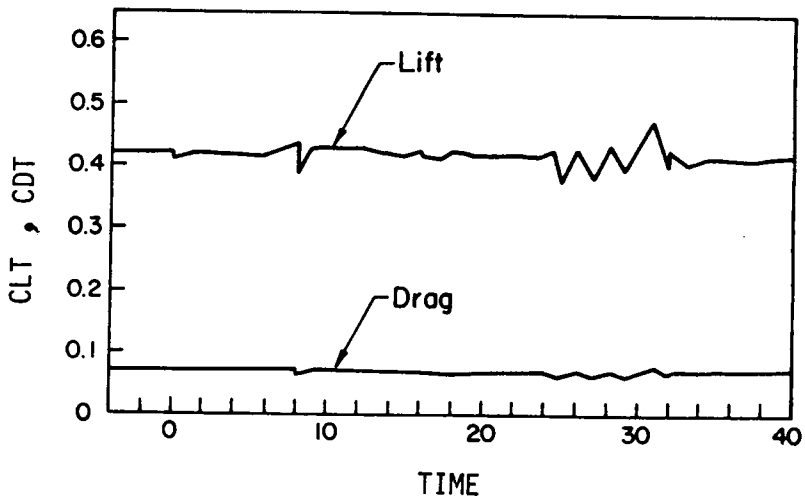

(c)

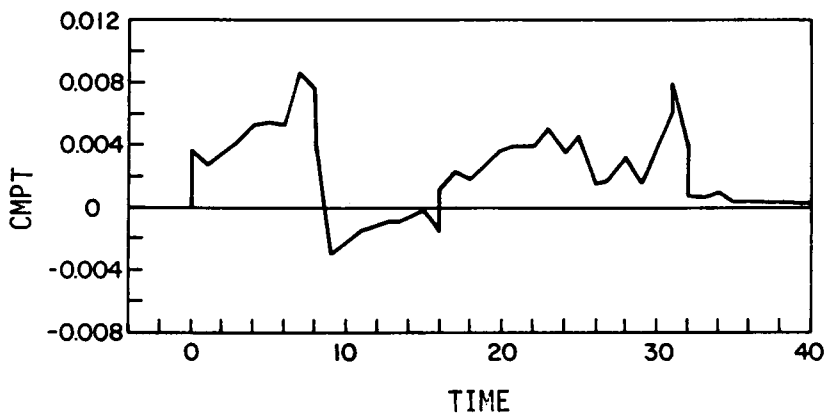

(d)

Figure 5.9. (c) Lift and drag coefficients on the complete configuration as functions of time.
(d) Roll-moment coefficient of the complete configuration as a function of time.

The results are shown in Figure 5.10. In part a the angles of attack are plotted as functions of time for two complete cycles. The normal force coefficients are shown in part b, where CN1 and CN2 represent the normal force coefficients of the canards and CN3 represent that of the main wing. In addition to the lift coefficients for the canards (CL1, CL2) and the wing (CL3), the lift coefficient for the ensemble (CLT) is shown in part c. Similarly, part d shows the drag coefficients for the canards (CD1, CD2), for the main wing (CD3), and for the complete configuration (CDT). Finally, the pitch moment coefficients of the canards (CMP1, CMP2), of the main wing (CMP3), and of the ensemble (CMPT) are shown in part e. The normal-force coefficient of the main wing reaches a minimum just after that of the canards becomes a maximum. Similar observation can be noticed for the lift and the drag coefficient. However the pitch-moment coefficient of the main wing becomes a minimum before that of the canards reaches a maximum. A good reason for such observations is the time traveled by the vortices in the wakes of the canards before interacting with vortices of the main wing. This time interval often called lag time.

Third example, again here we used the mesh shown in Figure 5.7a, the steady-state solution obtained for $\alpha_{canard} = \alpha_{wing} = 4^{0}$ was used as an initial condition for the following sinuoidal motion:

$$\theta(t) = 4\cos(ft) \tag{5.18}$$

and

$$\dot{\theta}(t) = -4 f \sin(ft) \tag{5.19}$$

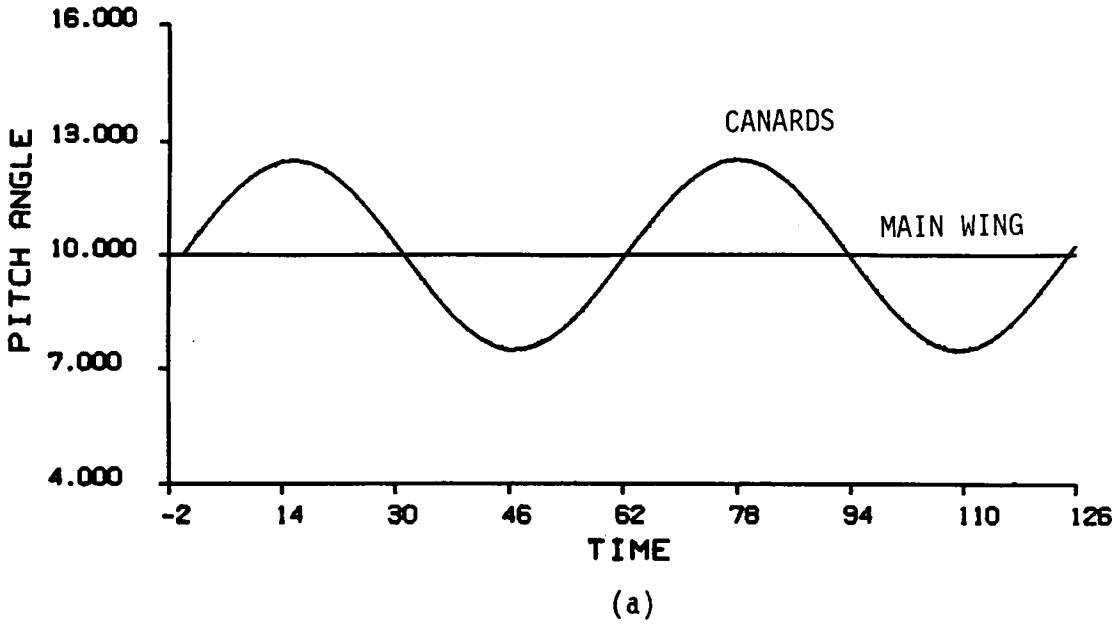

(a)

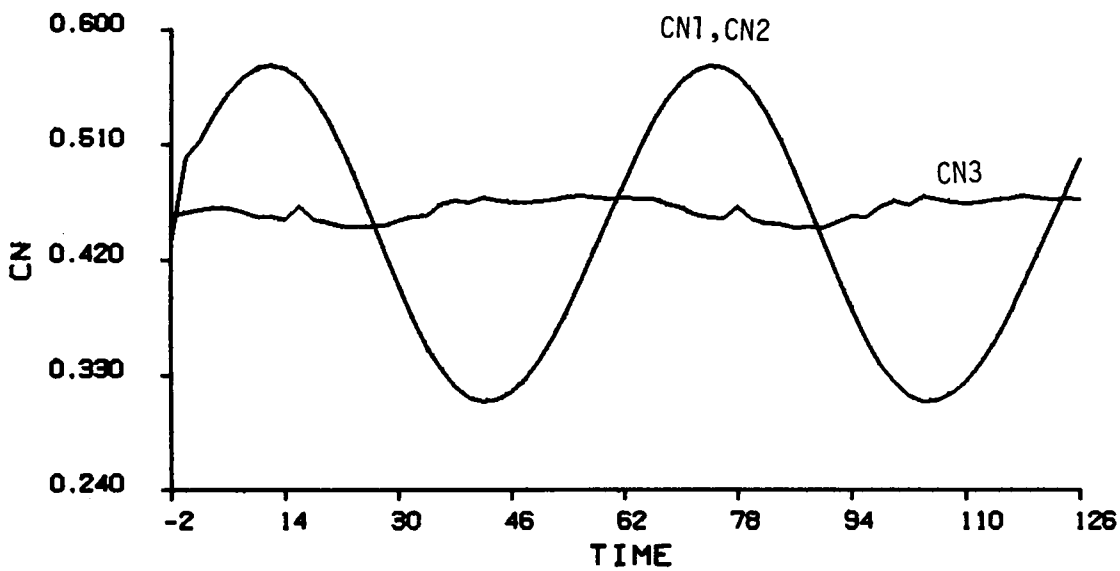

(b)

Figure 5.10. Sinusoidal motion (Equation 5.16):
(a) Angles of attack of the canards and the main wing as functions of time.
(b) Normal-force coefficients as functions of time.

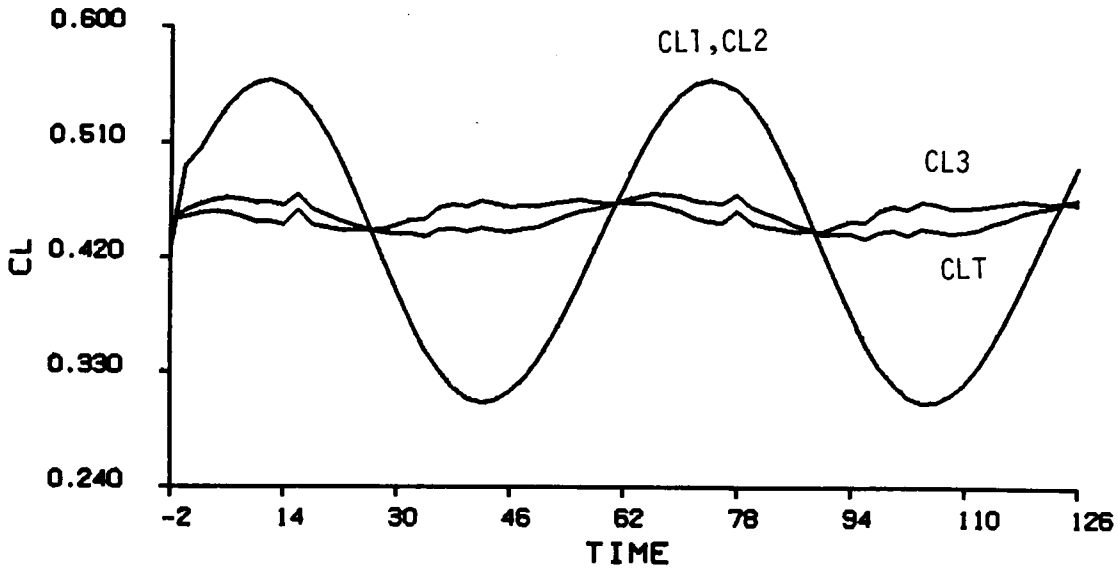

(c)

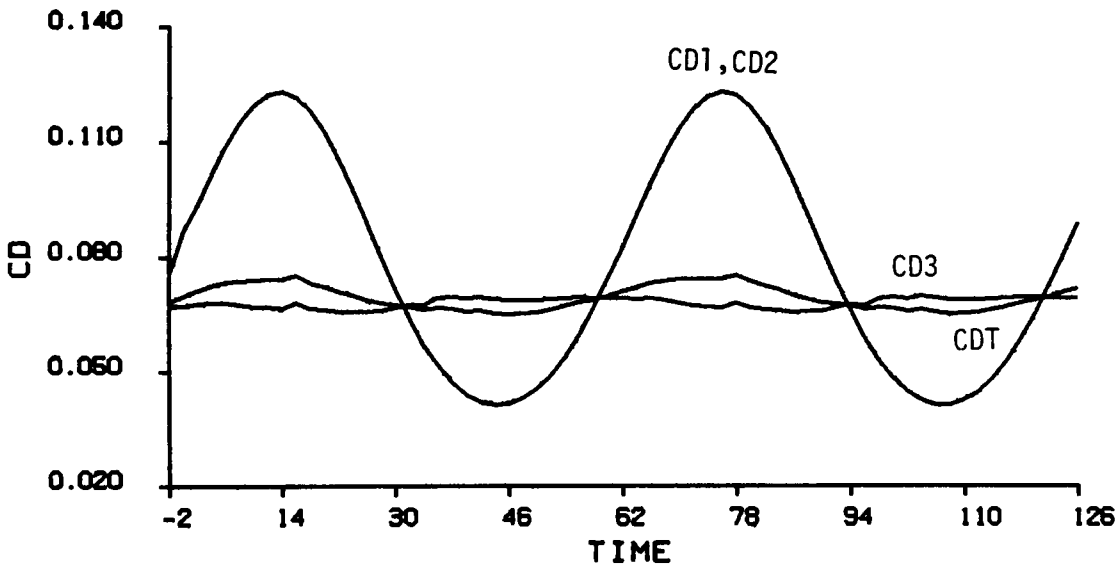

(d)

Figure 5.10. (c) Lift coefficients as functions of time.
(d) Drag coefficients as functions of time.

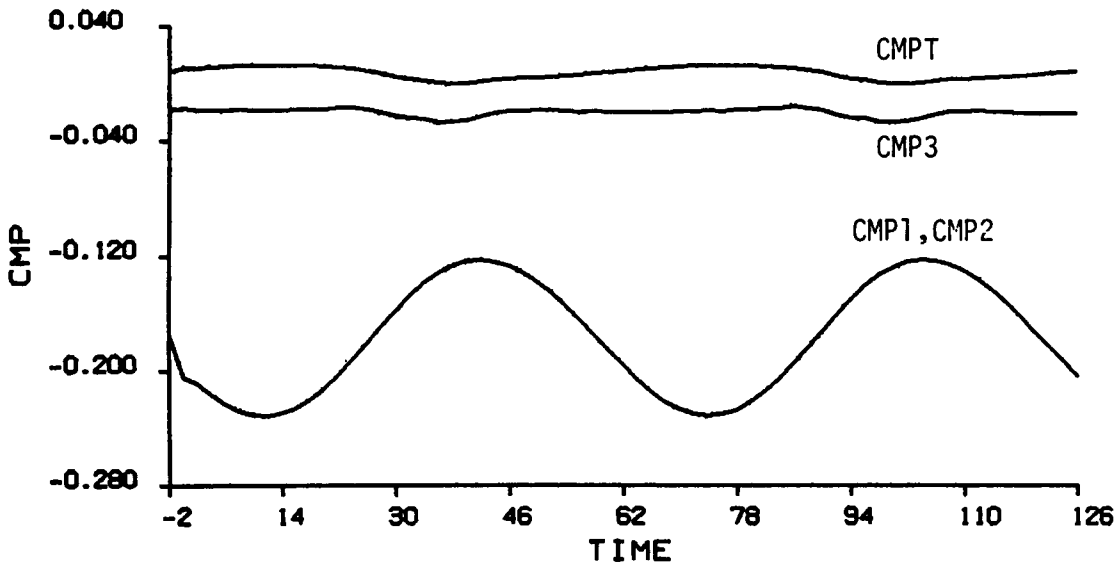

(e)

Figure 5.10. (e) Pitch-moment coefficients as function of time.

where f = 0.06830 (30 Hz) which is based on wind-tunnel informations given by Buchanan and Cayse (1986). Again here $\theta(t)$ is in degrees and t is the nondimensional time. The results for this case are shown in Figure 5.11. Same observations noticed in part b, c, d, and e of Figure 5.10 can be noticed in the corresponding parts of Figure 5.11. However, sharp spikes in the later are clearly showing. These spike did not show pronouncely in Figure 5.10 because of the difference in the nature of the motion. In Figure 5.11 the amplitude to angle of attack ratio is one, whereas in Figure 5.10 the same ratio is 0.25. In other words, the motion of the canards is felt by the main wing very readily when the angle of attack of the main wing is in the order of the amplitude of the motion or vise versa. We are not sure whether these spikes are caused by an error in the code or are they characteristics of the real flow? In Figure 5.10, force coefficients of the canards seem to have the same period and in phase except the pitch-moment curve it is out of phase by $\pi/2$. Moreover, all curves are out of phase with the motion curve. On the other hand, Figure 5.11d shows that the drag coefficient developed a harmonic motion with a period equals to one half of that of the normal-force coefficient and the lift-coefficient curves. The reason can be seen from Equation (5.18), i.e., oscillating the canards about zero. Again here the normal-force coefficient curve and the lift coefficent curve are in phase where the pitch-moment coefficient is out of phase by $\pi/2$, and all curves are not in phase with the curve of motion.

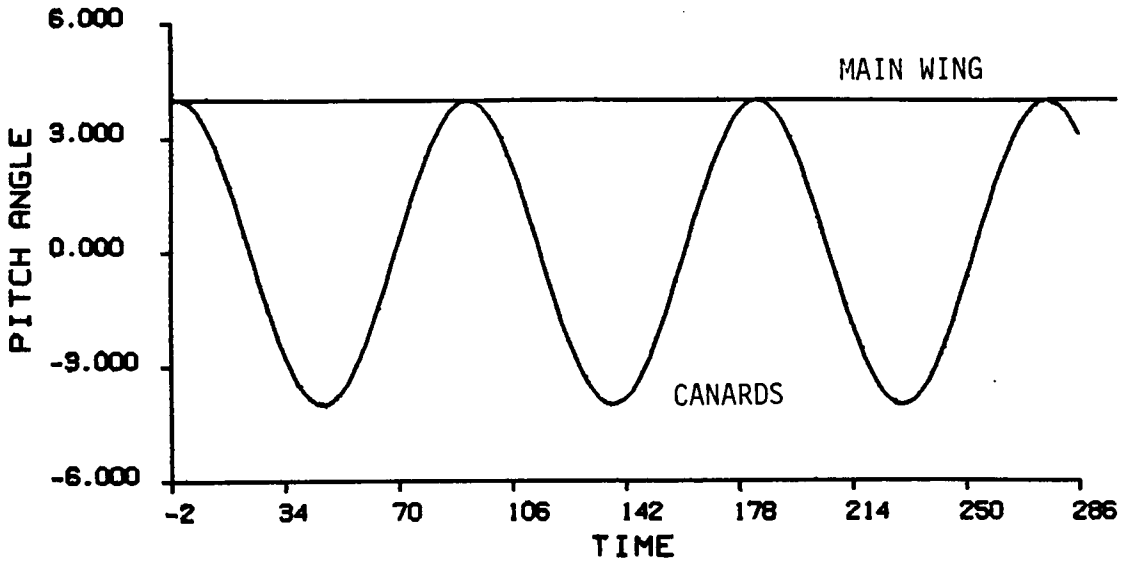

(a)

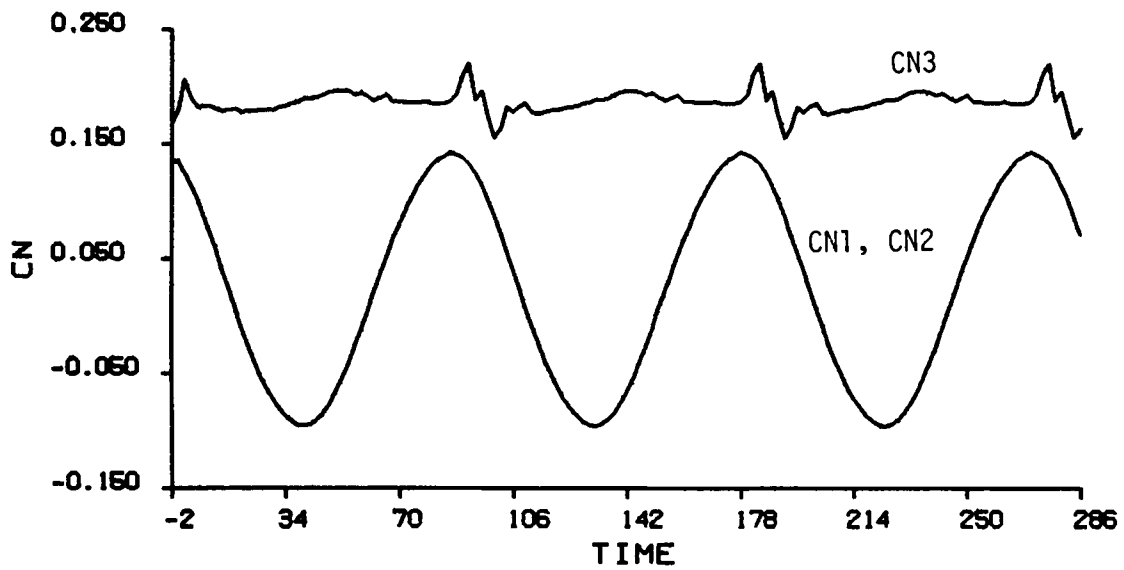

(b)

Figure 5.11. Sinusoidal motion (Equation 5.18):
(a) Angles of attack of the canards and the main wing as functions of time.
(b) Normal-force coefficients as functions of time.

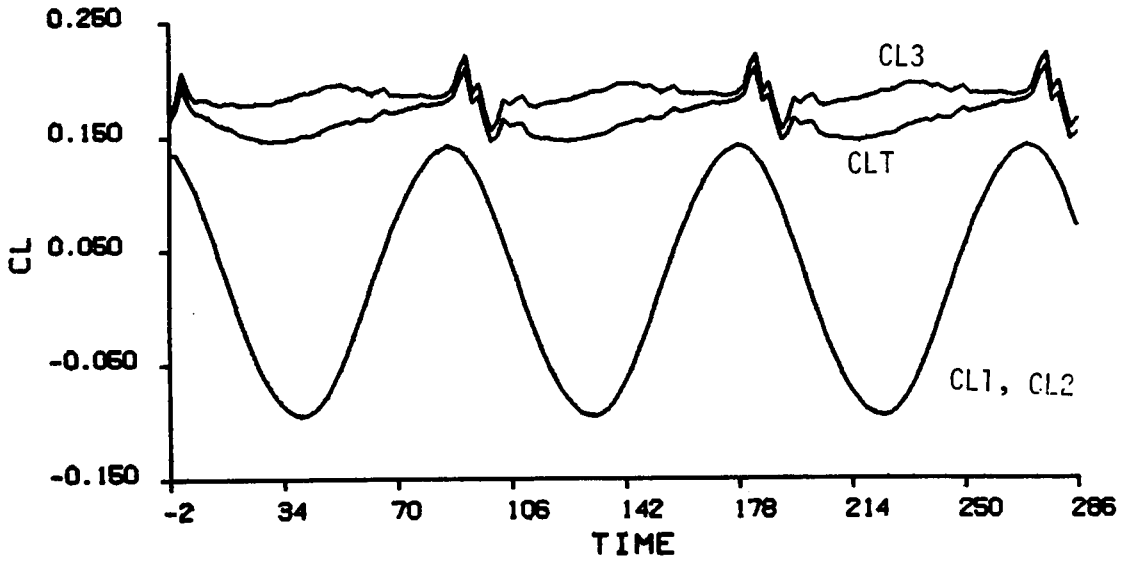

(c)

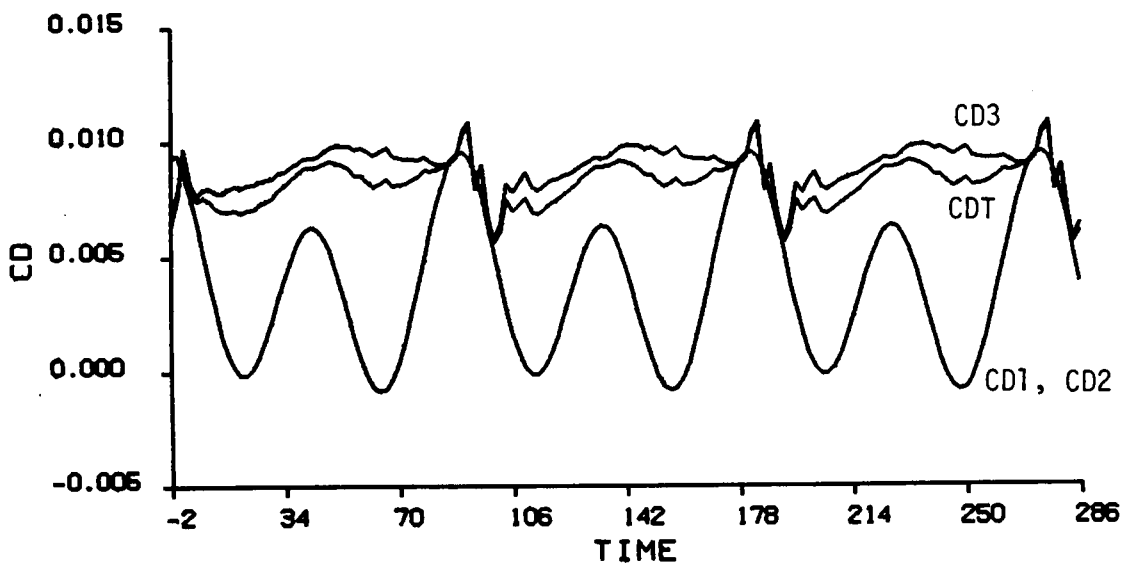

(d)

Figure 5.11. (c) Lift coefficients as functions of time.
(d) Drag coefficients as functions of time.

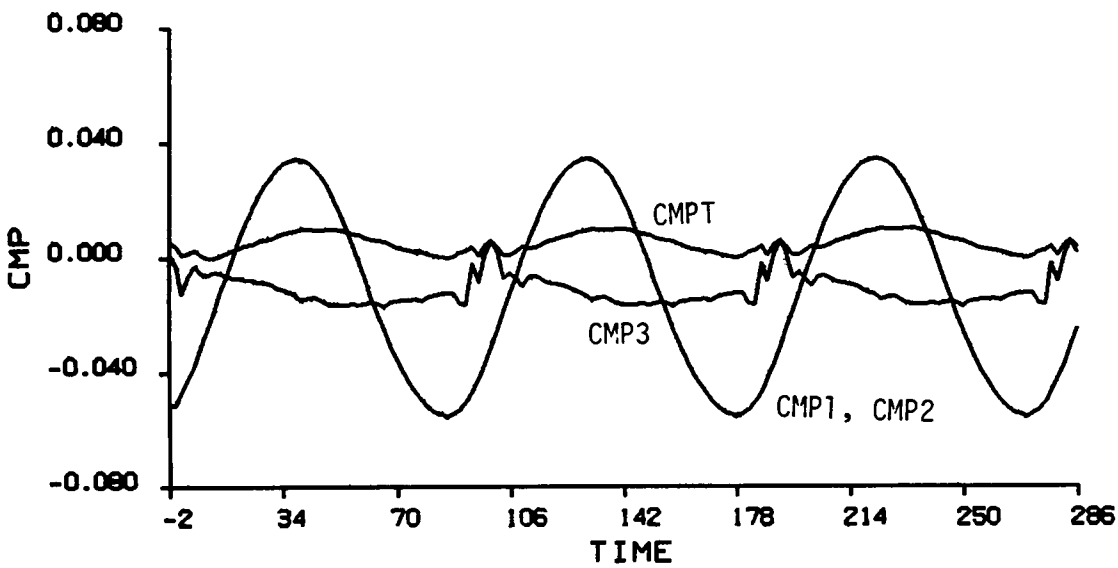

(e)

Figure 5.11. (e) Pitch-moment coefficients as function of time.

Finally, for the case in Figure 5.11, we note that the lift coefficient of the main wing (CL3) reaches a maximum value just after the maximum value of the canards (CL1, CL2) by a period of time of 0.0203 seconds. The same observation can be made for the pitch-moment coefficients; the time involved here is 0.1758 seconds. The experimental results of Buchanan and Cayse (1986) indicate a time lag value of 0.0028 seconds for the case shown in Figure 5.11. Their report did not indicate on what kind of measurements this time lag was based. Our lift-coefficient curve indicates a time lag of 0.0025 seconds.

5.4. Conclusions

The general unsteady vortex-lattice method is extended to treat multiple lifting surfaces. The choice of the present communication scheme eased the complications involved. Such a scheme played an effective role in the bookkeeping process.

The present method predicts the aerodynamic loads and fully describes the flowfield. In the numerical examples considered, the method shows good agreements with available wind-tunnel data for steady flows. For the unsteady flows, the technique shows good comparison with existing experimental data. Finally, the method emphasizes the strong vorticity interaction between the wakes and the lifting surfaces. Even though the numerical code of the present method uses so much computer time, a finer mesh is suggsted. The results are very promising.

REFERENCES

1. Agnew, J. W., and J. R. Hess, Jr. (1979). Benefits of aerodynamic interaction to three surface configuration. AIAA Paper 79-1830.

2. Atta, E. H. (1976). Unsteady flow over arbitrary wing-planforms including tip separation. M. S. Thesis, Dept. of Engineering Science and Mechanics, Virginia Polytechnic Institute and State University, Blacksburg, Virginia.

3. Atta, E. H., O. A. Kandil, D. T. Mook, and A. H. Nayfeh (1976). Unsteady flow past wings having sharp-edge separation. NASA SP-405, 407-418.

4. Atta, E. H., O. A. Kandil, D. T. Mook, and A. H. Nayfeh (1977). Unsteady aerodynamic loads on arbitrary wings including wing-tip and leading-edge separation. AIAA Paper No. 77-156.

5. Atta, E. H. (1978). Nonlinear aerodynamics of wings and wing-body combinations. Ph.D. Dissertation, Department of Engineering Science and Mechanics, Virginia Polytechnic Institute and State University, Blacksburg, Virginia.

6. Atta, E. H., and A. H. Nayfeh (1978). Nonlinear aerodynamics of wing-body combinations. AIAA Paper 78-1206.

7. Belotserkovskii, S. M. (1966). Calculating the effects of gusts on an arbitrary thin wing. Fluid Dynamics, 1.

8. Belotserkovskii, S. M. (1969). Calculation of the flow around wings of arbitrary planform in a wide range of angles of attack. NASA TT F-12, 291.

9. Belotserkovskii, S. M., and M. I. Nisht (1974). Nonstatinary nonlinear theory of a thin wing of arbitrary planform. Fluid Dynamics, 9.

10. Beyers, M. E. (1983). Subsonic roll oscillation experiments on the standard dynamics model. AIAA Paper 83-2134.

11. Brandon, J. M., and L. T. Nguyen (1986). Experimental study of effects of forebody geometry on high angle of attack static and dynamic stability. AIAA Paper 86-0331.

12. Buchanan, T., and R. Cayse (1986). Aerodynamic lag investigation on the X029A at Mach 0.3 to 1.6. AEDC-TSR-86-V3.

13. Calarese, W. (1984). Close-coupled canard-wing vortex interaction. Journal of Aircraft, 21, 99-100.

14. Croom, M. A., S. B. Grafton, and L. T. Nguyen (1982). High angle-of-attack characteristics of three-surface fighter aircraft. AIAA Paper 82-0245.

15. Elzebda, J. M., D. T. Mook, and A. H. Nayfeh (1985). Unsteady aerodynamic interference for lifting surfaces. AIAA Paper 85-1801.

16. Er-El, J., and A. Seginer (1985). Vortex trajectories and breakdown on wing-canard configurations. Journal of Aircraft, 22, 641-648.

17. Ericsson, L. E. (1984). Flow phenomena causing wing and body rock. AIAA Paper 84-2177.

18. Ericsson, L. E. (1983). The fluid mechanics of slender wing rock. AIAA Paper 83-1810.

19. Ericksson, L. E., and A. Rizzi (1984). Computation of vortex flow around a canard/delta combination. Journal of Aircraft, 21, 858-865.

20. Frei, D., and M. Moore (1985). The X-29 - A unique and innovative aerodynamic concept. SAE Paper 851771.

21. Garnahan, B., H. A. Luther, and J. O. Wilkes (1969). Applied numerical methods. John Wiley & Sons, Inc., New York, New York.

22. Giesing, J. P., T. P. Kalman, and W. P. Rodden (1972). Subsonic steady and oscillatory aerodynamics for multiple interfering wings and bodies. Journal of Aircraft, 9, 693-702.

23. Grafton, S. B., W. P. Gilbert, M. A. Croom, and D. G. Murri (1982). High-angle-of-attack characteristics of a forward-swept wing fighter configuration. AIAA Paper 82-1322.

24. Griffin, K. E., and F. M. Jones (1983). Wake characteristics and interactions of the canard/wing lifting surface configuration of the X-29 forward-swept wing flight demonstrator. AIAA Paper 83-1835.

25. Hsu, C., and C. E. Lau (1985). Theory of wing rock. AIAA Paper 85-0199.

26. Hsu, C., and C. E. Lan (1985). Theory of wing rock. Journal of Aircraft, 22, 920-924.

27. Hummel, O. (1979). On vortex formulation over a slender wing at large angles of incidence. AGARD CP-247.

28. Hwang, C., and W. S. Pi (1978). Some observations on the mechanism of aircraft wing rock. AIAA Paper 78-1456.

29. Kandil, O. A. (1974). Prediction of the steady aerodynamic loads on lifting surfaces having sharp-edge separation. Ph.D. Dissertation, Department of Engineering Science and Mechanics, Virginia Polytechnic Institute and State University, Blacksburg, Virginia.

30. Kandil, O. A., D. T. Mook, and A. H. Nayfeh (1974). Nonlinear prediction of the aerodynamic loads on lifting surfaces. AIAA Paper 74-503.

31. Kandil, O. A., D. T. Mook, and A. H. Nayfeh (1977). A numerical technique for computing subsonic flow past three dimensional canard-wing configurations with edge separation. AIAA Paper 77-1.

32. Kandil, O. A., E. H. Atta, and A. H. Nayfeh (1977). Three dimensional steady and unsteady asymetric flow past wings of aribtrary planforms. AGARD Paper No. 2.

33. Karamcheti, K. (1966). Principles of ideal fluid aerodynamics. John Wiley and Sons, Inc., New York, New York.

34. Katz, J., and D. Levin (1985). Measurements of canard-induced roll oscillations. AIAA Paper 1830-CP.

35. Keith, M. W., and B. P. Selberg (1985). Aerodynamic canard/wing parametric analysis for general-aviation applications. Journal of Aircraft, 22, 401-408.

36. Kelly, S. G. (1977). A systematic investigation of the parameters affecting the accuracy of the vortex-lattice method. M. S. Thesis, Department of Engineering Science and Mechanics, Virginia Polytechnic Institute and State University, Blacksburg, Virginia.

37. Kim, M. J., and D. T. Mook (1986). Application of continuous vorticity panels to general unsteady incompressible two-dimensional lifting flows. Journal of Aircraft, 23, 464-471.

38. Konstadinopoulos, P. (1981). A vortex-lattice method for general unsteady subsonic aerodynamics. M.S. Thesis, Department of Engineering Science and Mechanics, Virginia Polytechnic Institute and State University, Blacksburg, Virginia.

39. Konstadinopoulos, P., D. T. Mook, and A. H. Nayfeh (1981). A numerical method for general unsteady aerodynamics. AIAA Paper 81-1877.

40. Konstadinopoulos, P., D. T. Mook, and A. H. Nayfeh (1983). Numerical simulation of the subsonic wing-rock phenomenon. AIAA Paper 83-2115.

41. Konstadinopoulos, P. A. (1984). Numerical simulation of the subsonic wing-rock phenomenon. Ph.D. Thesis, Department of Engineering Science and Mechanics, Virginia Polytechnic Institute and State University, Blacksburg, Virginia.

42. Konstadinopoulos, P., D. F. Thrasher, D. T. Mook, A. H. Nayfeh, and L. Watson (1985). A vortex-lattice method for general, unsteady aerodynamics. Journal of Aircraft, 22, 43-49.

43. Konstadinopoulos, P., D. T. Mook, and A. H. Nayfeh (1985). Subsonic wing rock of slender delta wings. Journal of Aircraft, 22, 223-228.

44. Landahl, M. (1968). Pressure loading functions for oscillating wings with control surfaces. AIAA Journal, 6, 345-349.

45. Levin, D., and J. Katz (1981). Vortex-lattice method for the calculation of the nonsteady separated flows over delta wings. Journal of Aircraft, 18, 1032-1037.

46. Levin, D., and J. Katz (1982). Dynamic load measurements with delta wings undergoing self-induced roll-oscillations. AIAA Paper 82-1320.

47. Maddox, S. A. (1973). An extension of a vortex-lattice method to include the effects of leading-edge separation. M.S. Thesis, Department of Engineering Science and Mechanics, Virginia Polytechnic Institute and State University, Blacksburg, Virginia.

48. Maneuver Limitation of Combact Aircraft. AGARD-AR-155A. France, August 1979.

49. Mason, W. H. (1986). Wind-tunnel data provided by Dr. W. H. Mason at the Grumman Aerospace Corp., Huntington, NY.

50. Miller, B. D., and S. K. Hadley (1963). Application of forward sweep wings to air combat fighter. AIAA Paper 83-1833.

51. Mook, D. T., and S. A. Maddox (1974). An extension of a vortex-lattice method to include the effects of leading-edge separation. Journal of Aircraft, 11, 127-128.

52. Mook, D. T., and A. H. Nayfeh (1985). Application of the vortex-lattice method to high-angle-of-attack subsonic aerodynamics. SAE TP 851817.

53. Moore, M., and D. Frei (1983). X-29 Forward swept wing aerodynamic overview. AIAA Paper 83-1834.

54. Murri, D. G., M. A. Croom, and L. T. Nguyen (1983). High angle-of-attack flight dynamics of a forward-swept wing fighter configuration. AIAA Paper 83-1837.

55. Nayfeh, A. H., D. T. Mook, and A. Yen (1979). The aerodynamics of small harmonic oscillations around large angles of attack. AIAA Paper 79-1520.

56. Nguyen, L. T., W. P. Gilbert, J. Gera, K. W. Iliff, and E. K. Eneroldson (1980). Application of high-α control system concepts to a variable sweep fighter airplane. AIAA Paper 80-1582.

57. Nguyen, L. T., L. Yip, and J. R. Champers (1981). Self-induced wing rock of slender delta wing. AIAA Paper 81-1883.

58. Nikolitsch, D. (1978). Normal force and pitching moment coefficients of bodies and wing-body combination at very high angle of attack. AIAA Paper 78-63.

59. Prandtl, L., and O. G. Tietjens (1934). Fundamentals of Hydro- and Aerodynamics. Dover Publications, Inc., New York, New York.

60. Ross, A. J. (1972). Investigation of nonlinear motion experienced on a slender-wing research aircraft. Journal of Aircraft, 9, 625-631.

61. Ross, A. J. (1979). Lateral stability at high angles of attack, particularly wing rock. AGARD CP-260, Paper 10.

62. Rowe, W. S., B. A. Winther, and M. C. Redman (1974). Unsteady subsonic aerodynamic loadings caused by control surface motions. Journal of Aircraft, 11, 45-54.

63. Schmidt, L. V. (1979). Wing rock due to aerodynamic hysteresis. Journal of Aircraft, 16, 129-133.

64. Spacht, G. (1980). The forward swept wing: a unique design challenge. AIAA Paper 80-1885.

65. Thrasher, D. F., D. T. Mook, O. Kandil, and A. H. Nayfeh (1977). Application of the vortex-lattice concept to general, unsteady lifting-surface problems. AIAA Paper 77-1157.

66. Thrasher, D. F. (1979). Nonlinear unsteady aerodynammics with application to dynamic-aerodynamic interaction. M. S. Thesis, Department of Engineering Science and Mechanics, Virginia Polytechnic Institute and State University, Blacksburg, Virginia.

67. Thrasher, D. F., D. T. Mook, and A. H. Nayfeh (1979). A computer based method for analyzing the flow over sails. The Fourth Chesapeake Sailing Yacht Symposium, Chesapeake, Maryland.

68. Uchiyama, N., R. P. Mikkilineni, and J. M. Wu (1978). The analysis of wing-body combinations at moderate angles of attack. AIAA Paper 78-62.

The vita has been removed from the scanned document

TWO-DEGREE-OF-FREEDOM SUBSONIC WING ROCK AND NONLINEAR AERODYNAMIC INTERFERENCE

by

Jamal M. Elzebda

ABSTRACT

In many situations the motion of the fluid and the motion of the body must be determined simultaneously and interactively. One example is the phenomenon of subsonic wing rock. A method has been developed that accurately simulates the pitching and rolling motions and accompanying unsteady flowfield for a slender delta wing. The method uses a predictor-corrector technique in conjunction with the general unsteady vortex-lattice method to compute simultaneously the motion of the wing and the flowfield, fully accounting for the dynamic/aerodynamic interaction. For a single degree of freedom in roll, the method predicts the angle of attack at which the symmetric configuration of the leading-edge vortex system becomes unstable, the amplitude, and the period of the resulting self-sustained limit cycle, in close agreement with two wind-tunnel experiments.

With the development of modern aerodynamic configurations employing close-coupled canards, such as the X-29, comes the need to simulate unsteady aerodynamic interference. A versatile method based on the general unsteady vortex-lattice technique has been developed. The method yields the time histories of the pressure distribution on the

lifting surfaces, the distribution of vorticity in the wakes, and the position of the wakes simultaneously. As an illustration of the method, the unsteady flowfield for a configuration closely resembling the X-29 is presented. The results show the strong influence of the canards on the main wing, including the time lag between the motions of the canards and the subsequent changes in the vorticity and hence the pressure distributions and loads on the main wing.